Quantum Transport Simulations of Nanoscale Materials

Dissertation by

Obodo Tobechukwu Joshua
Ph.D., Materials Science and Engineering

Submitted in Partial Fulfillment of the Requirements

For the Degree of

Doctor of Philosophy

King Abdullah University of Science and Technology, Thuwal,

Kingdom of Saudi Arabia

(January, 2016)

The dissertation of Obodo Tobechukwu Joshua is approved by the examination committee

Committee Chairperson: Prof. Udo Schwingenschlögl

Committee Member: Prof. Aurelien Manchon

Committee Member: Prof. Jörg Eppinger

Committee Member: Prof. Stefano Sanvito

King Abdullah University of Science and Technology

2016

ABSTRACT

Quantum Transport Simulations of Nanoscale Materials

Obodo Tobechukwu Joshua

Nanoscale materials have many potential advantages because of their quantum confinement, cost and producibility by low-temperature chemical methods. Advancement of theoretical methods as well as the availability of modern high-performance supercomputers allow us to control and exploit their microscopic properties at the atomic scale, hence making it possible to design novel nanoscale molecular devices with interesting features (e.g switches, rectifiers, negative differential conductance, and high magnetoresistance). In this thesis, state-of-the-art theoretical calculations have been performed for the quantum transport properties of nano-structured materials within the framework of Density Functional Theory (DFT) and the Non-equilibrium Green's Function (NEGF) formalism. The switching behavior of a dithiolated phenylene-vinylene oligomer sandwiched between Au(111) electrodes is investigated. The molecule presents a configurational bistability, which can be exploited in constructing molecular memories, switches, and sensors. We find that protonation of the terminating thiol groups is at the origin of the change in conductance. H bonding at the thiol group weakens the S-Au bond, and thus lowers the conductance. Our results allow us to re-interpret the experimental data originally attributing the conductance reduction to H dissociation. Also examined is current-induced migration of atoms in nanoscale devices that plays an important role for device operation and

breakdown. We studied the migration of adatoms and defects in graphene and carbon nanotubes under finite bias. We demonstrate that current-induced forces within DFT are non-conservative, which so far has only been shown for model systems, and can lower migration barrier heights.

Further, we investigated the quantum transport behavior of an experimentally observed diblock molecule by varying the amounts of phenyl (donor) and pyrimidinyl (acceptor) rings under finite bias. We show that a tandem configuration of two dipyrimidinyl-diphenyl molecules improves the rectification ratio, and tuning the asymmetry of the tandem set-up by rearranging the molecular blocks greatly enhances it. It has been recently demonstrated that the large band gap of boronitrene can be significantly reduced by carbon functionalization. We show that specific defect configurations can result in metallicity, raising interest in the material for electronic applications. In particular, we demonstrate negative differential conductance with high peak-to-valley ratios, depending on the details of the material, and identify the finite bias effects that are responsible for this behavior. Also, we studied the spin polarized transport through Mn-decorated topological line defects in graphene. Strong preferential bonding is found, which overcomes the high mobility of transition metal atoms on graphene and results in stable structures. Despite a large distance between the magnetic centers, we find a high magnetoresistance and attribute this unexpected property to very strong induced π magnetism. Finally, the results obtained herein advance the field of quantum electronic transport and provide significant insight on switches, rectification, negative differential conductance, magnetoresistance, and current-induced forces of novel nanoscale materials.

ACKNOWLEDGEMENTS

Reaching this milestone is a convolution of support and generosity of professors, colleagues, friends, and family. Their genuine words of wisdom and encouragement contributed towards making this thesis a success.

Firstly, I would like to express my sincere gratitude to my advisor Prof. Udo Schwingenschlögl for his his patience, motivation, and immense support during my doctorate study. I would like to thank the rest of my thesis committee: Prof. S. Sanvito, Prof. A. Manchon, and Prof. J. Eppinger for their insightful comments and encouragement. Special thanks to KAUST for funding and the computing team for the computational resources and support.

Also, special thanks to Dr. I. Rungger, Dr. K. Gkionis, Dr. K. O. Obodo, and Dr. A. Murat, Dr. S. Kumar, and Dr. M. U-Kahaly, whose invaluable contributions is indelible. Thanks to members of the Computational Physics and Materials Science group at KAUST for useful discussions, especially doctoral candidates: E. Munoz Montez, S. Grytsyuk, O. Salawu, C. Akosa, I. Ajia, P. Diaye, S. Ghosh whose fruitful discussions impacted my learning curve. To my friends: Dr. C. O. Abah, A. O. Ogbuu, Dr. K. Thaneshwor, Dr. J. Chibueze, A. Omoniyi, C. O. Irerua, A. Alfazazi, B. Arekame, S. Nebo, J. Pagels, and V. Ude and my colleagues in University of Nigeria, Nsukka especially: Prof. C. M. I. Okoye, Prof. E. Chukwude, and Prof. R. U. Osuji, I am grateful for your support.

Last but not the least, I would like to thank my family; my parents: Chief and Lolo C. N. Obodo, my brothers: Ebuka, Kingsley, Nnamdi, Chidi, and Sopulu, my lovely sisters: Nnenna and Chinyere and to my special gift: M. P. Madu for their unwavering support and prayers. Above all, I give God all the glory.

TABLE OF CONTENTS

LIST OF ABBREVIATIONS

$T(E)$	Transmission Coefficient
ASIC	Atomic-Self Interaction Correction
DFT	Density Functional Theory
EA	Electron Affinity
GGA	Generalized Gradient Approximation
HK	Hohenberg and Kohn
HOMO	Highest Occupied Molecular Orbital
I-V	Current Voltage characteristics
IP	Ionization Potential
LCAO	Linear Combination of Atomic Orbitals
LDA	Local Density Approximation
LUMO	Lowest Occupied Molecular Orbital
MEP	Minimum Energy Paths
NDC	Negative Differential Conductance
NEB	Nudged Elastic Band Method
NEGF	Non-equilibrium Green's Function
SIC	Atomic-Self Interaction Correction
SW	Stone-Wales

LIST OF FIGURES

LIST OF TABLES

Chapter 1

General Introduction

With the progressing reduction in size of electronic devices, the importance of molecular electronics continues to grow. A comprehensive review of the development of this research area has been given in 2013 in Ref. [1]. There is a zoo of possibilities for technological applications due to the diversity of the electronic functionalities provided by different, often specifically designed and synthesized, molecules [2]. Important examples include diodes [3, 4], switches [5**?**], memories [6], and transistors [7, 8]. On the other hand, the exploration of the charge transport through single molecules and molecular monolayers has led to key insight into various fundamental effects, facilitated by developments in measuring techniques [9, 10].

Since the characteristic length scale of molecular devices is nanometer, they are strongly influenced by quantum phenomena [11]. The quantum nature is frequently exploited for improving the device performance [12–15]. For instance, band structure engineering has led to a new generation of magnetic tunnel junctions, which now operates in commercial hard disks [16]. Proposals for powerless logic elements based on quantum mechanical interference are in search of an experimental realization [17]. On the other hand, atomic motion induced by an electric current is associated with a number of problems towards device miniaturization, in particular degradation, which

can be resolved only, if a detailed understanding of current-induced forces is achieved [18, 19].

Attaching electrodes to single molecules is one major challenge in single molecule electronics, mostly due to issues of reliability and reproducible. Several approached have been developed to overcome this imitation, including mechanical break junctions [20], electromigration break junctions [21], electrochemical deposition [22], scanning probe techniques [23], and lithography [24–26]. While the mechanical break junction technique is well established are therefore most widely used, the electromigration break junction technique is advantageous to fabricate a three electrode molecular device. The third gate either is already present before electrobreaking or a conducting oxidized silicon substrate is used [27, 28]. A drawback of the technique, as compared to mechanical break junctions, lies in the difficulty of obtaining a large number of junctions for studying the statistical behaviour [27, 29].

A theoretical assessment of molecular devices is possible by means of the non-equilibrium Green's function (NEGF) approach. In the Landauer-Büttiker formalism the current is given by

$$I = \frac{2e}{h} \int_{-\infty}^{+\infty} T(E)[f(E + E_F) - f(E - E_F)]dE, \tag{1.1}$$

where f is the Fermi-Dirac distribution function and $T(E)$ is the transmission coefficient. The electronic states of a molecule connected to electrodes are subject to modifications due to the metal-molecule bonding, which shift the energy levels as compared to the isolated molecule. In addition, orbital hybridization broadens the energy levels and results in finite lifetimes.

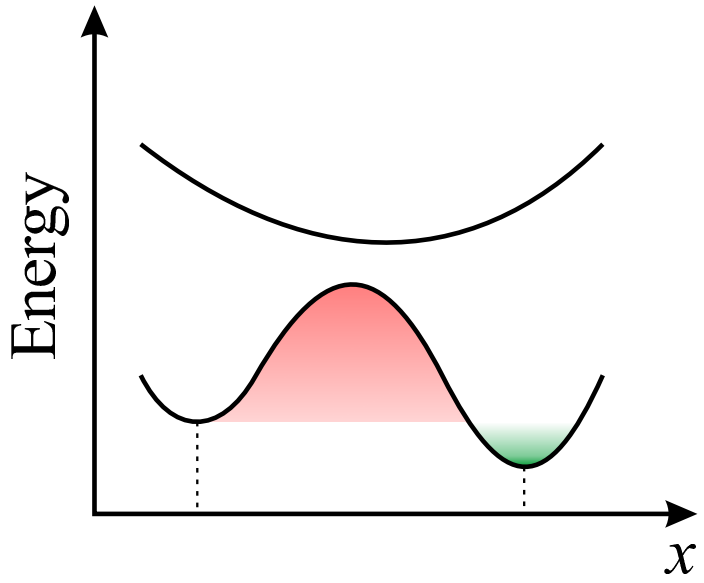

Figure 1.1: Schematic of a system with two locally stable states.

1.1 Switches

A molecular switch changes its physical or chemical properties, typically the conductance, between two or more stable states under external stimuli, such as a bias voltage or light [30], see the schematic representation given in Fig. 1.1. For a molecule to be a useful in a switch it must satisfy three basic requirements: (i) It must have states with distinctly different properties, (ii) the states must be sufficiently stable during operation, and (iii) the barrier between the states must clearly exceed the thermal energy at operating temperature. Molecular switches can be divided into conformational and redox switches. The former are based on a change in the structure, while in the latter the molecule gains or loses charge, which in turn also can induce (typically small) conformational changes.

For example, Sendler and coworkers have reported a reversible switching of diarylethene under light irradiation, between an open ring off state and a closed ring on state [31]. Nakamura and coworkers have addressed both experimentally and theoretically the length dependence of the properties of a covered quaterthiophene-based

molecular wire when the anchoring points (thus the length of the π-conjugated backbone) are varied. For increasing length the conductance decays exponentially. It also has been demonstrated both experimentally and theoretically that the electrodes used for contacting a molecule can enable or inhibit a switching behavior, demonstrating that the contact physics in molecular devices cannot be ignored [32]. For instance, perylene-3,4,9,10-tetracarboxylic dianhydride (PTCDA) switches when contacted by Au electrodes but not when contacted by semiconducting graphene electrodes.

Concerning redox switches, the oxidized state generally has lower conductance than the reduced state of a conjugated molecule [33]. Based on experimental results it has been claimed that oligophenylenevinylene switches between low and high conductance state when H bonds with the thiol end group that binds the molecule to Au electrodes [34]. However, theoretical results indicate that the H bonds reduce the conductance (the transmission coefficient at the Fermi level is lowered by about one order of magnitude), because the S-Au bond is weakened [35].

Bulovic and coworkers [36] have demonstrated an abrupt switching behavior with non-zero leakage current for a nano-electromechanical molecular switch, where the on state is achieved by compression of a molecular thin film. This solved the important problem of irreversible contact adhesion [37]. Figure 1.2(a) shows the two conformations of the system (top: off state, bottom: on state). According to Fig. 1.2(b) there is good agreement between the experimental and theoretical I-V curves during the switching cycles. The increasing surface adhesion forces then the thin film is compressed are balanced by elastic forces due to the deformation of the molecules, which promotes zero net stiction and recoverable switching. Numerical analysis indicates the potential of optimizing the on-off ratio, which would open a broad range of low power electronic applications.

In general, current-induced forces can affect the mechanical stability of nanojunc-

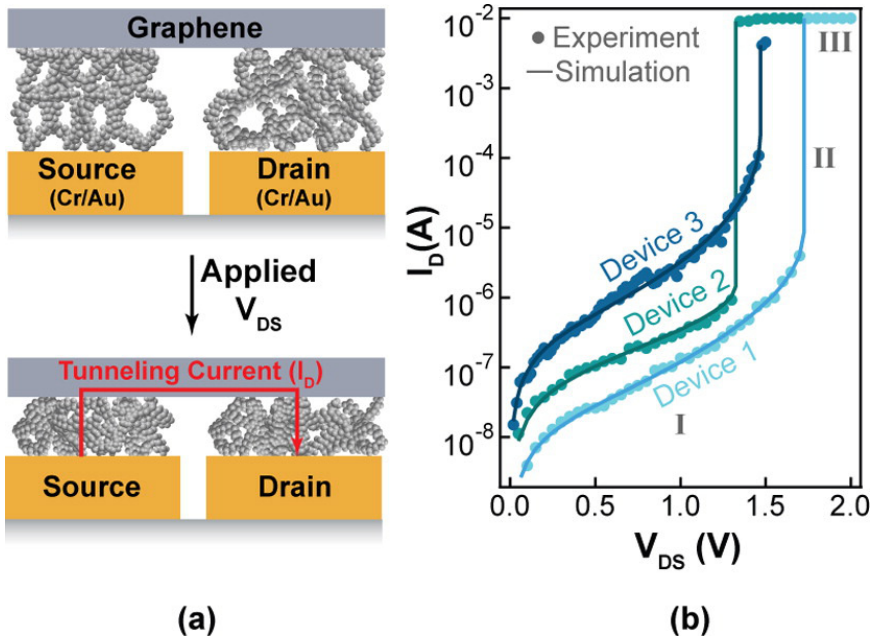

Figure 1.2: (a) Two terminal squitch architecture with Cr/Au bottom electrodes, self-assembled poly(ethylene glycol) dithiol molecular thin films, and graphene top electrode. (b) I-V curves for three example squitches and corresponding simulation results [36].

tions [38]. They are generally non-conservative [39, 40], which has been demonstrated in Ref. [41] by investigating the torque exerted by current-induced forces in a highly asymmetric molecular junction with a benzene molecule coupled to Pt electrodes. Transition states are key for characterizing molecular switches. Among the existing methods to determine transition states [42], the nudged elastic band method is a standard tool for describing the energetics. In particular, the energy difference between the molecular states must exceed the thermal energy.

1.2 Rectifiers

The rectification ratio

$$\mathcal{R} = \frac{I(V)}{I(-V)} \tag{1.2}$$

of a material is given by the currents $I(\pm V)$ under forward and reverse bias. The asymmetry requried of a molecular rectifier in the transport direction can be realized by different means [43, 44]: (1) donor-σ-acceptor molecules, (2) donor-π-acceptor molecules, and (3) asymmetric electrodes [3]. Since the discovery of the first molecular rectifier [45], various organic molecules are being put forward as possible candidates. Liu and coworkers [46] have studied the rectification behavior of a molecule composed of σ-nitrotoluene and o-aminotoluene connected via a σ-bridge. They have also addressed a tandem arrangement (serial connection), for which they found a strongly enhanced rectification ratio (about 20 times) as compared to the single molecule, and the effect of the length of the wire connecting the two molecular rectifiers. Venkataraman and coworkers [3] have demonstrated for a symmetric single-molecule junction a rectification ratio in excess of 200 at voltages as low as 370 meV, using a polar medium to modified the electrostatic environment of the junction in an asymmetric fashion when changing the bias polarity.

Dyck and Ratner [44] have presented a new design based on asymmetric anchoring: (1) Asymmetric chemically bonding of the molecule to the electrodes using one acceptor anchoring group (giving rise to the lowest unoccupied molecular orbital, LUMO) and one donator anchoring group (giving rise to the highest occupied molecular orbital, HOMO). (2) Use anchoring groups with frontier orbitals in the vicinity of the electrode Fermi level to promote Fermi level pinning. (3) Use a molecule consisting of two conjugated fragments that are not π-coupled. These building principles modify the HOMO-LUMO gap, which enhances the rectification ratio for the system studied in Ref. [44] by about two orders of magnitude. Fig. 1.3 shows the transmission coefficient under positive and negative bias. Positive bias results in a separation of the HOMO and LUMO peaks, which stay out of the transmission window, while for negative bias they come closer to each other and finally merge within the transmission

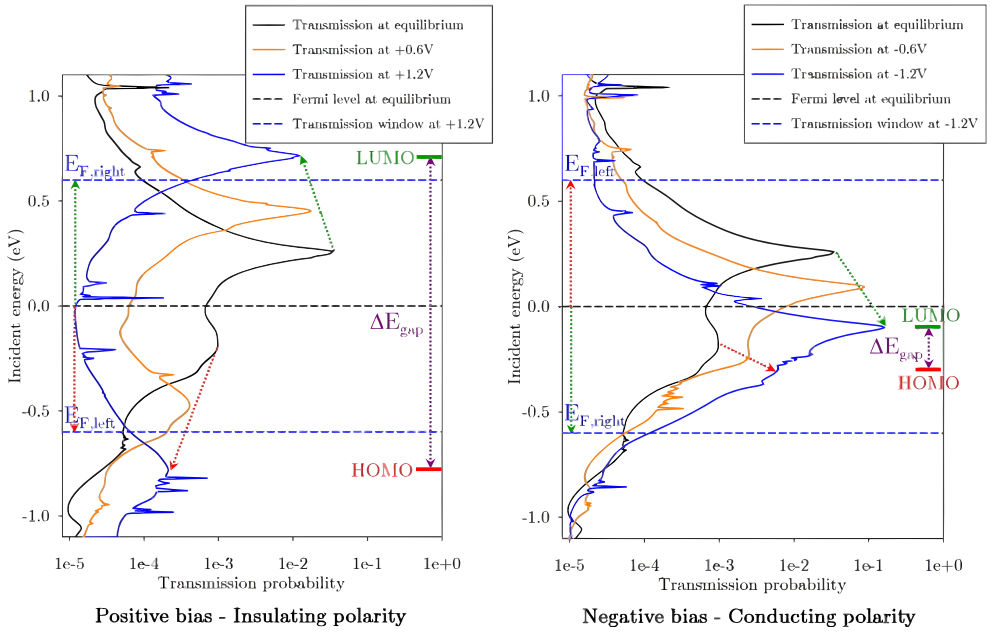

Figure 1.3: Left: Transmission spectra under positive bias. Red/green arrows indicate the evolution of the HOMO/LUMO transmission peaks, reflecting an increased HOMO-LUMO gap. The peaks stay out of the transmission window, as indicated by the dashed blue lines, and thus do not contribute to the current. Right: Transmission spectra under negative bias. The HOMO-LUMO gap decreases and the HOMO/LUMO transmission peaks enter the transmission window, which promotes conductance [44].

window.

Most studies on molecular rectifiers have used metallic substrates and electrodes, whereas graphite can have advantages, particularly with respect to its mechanical strength [47]. Many junctions can be measured without changes in the surface properties. Using the scanning tunneling microscope break junction technique, the authors of Ref. [47] have investigated a symmetric oligophenylamine molecule and observed a rectification behavior. Using the NEGF approach, they found that the energy dependence of the graphite density of states yields variations in the transmission coefficient that explain the experimental observations.

A major challenge in molecular electronics is to control the strength of the coupling between molecule and electrode to optimize the device performance. Non-covalent

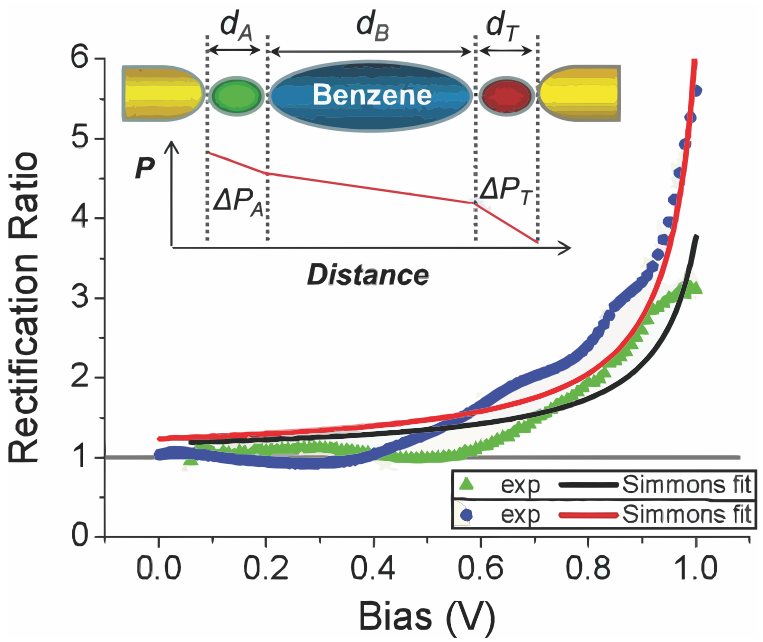

Figure 1.4: Rectification ratio for Au-NH_2-benzene-SH-Au (green and black) and Au-SH-benzene-NH_2-Au (blue and red) junctions. The inset shows a schematic of the potential drop across the junction (ΔP_A: amine group. ΔP_T: thiol group) [51].

bonding gives rise to minimal broadening of the molecular energy levels, as required to maximize the rectification ratio. In contrast, chemisorption results in prominent broadening, leakage currents and poor device performance. In this context, it has been demonstrates in Ref. [48] that tuning of the coupling between a ferrocenyl molecule and the electrodes enables rational design of the transport across organic-inorganic interfaces. From a materials point of view, the synthesis of the B-fullerene B_{40} is interesting, as the molecule is asymmetric and therefore gives rise to a distinct rectification behavior [49]. By varying the end groups of 1,2-bis(4-(phenylethynyl)phenyl)ethane the authors of Ref. [50] have designed a single-molecule diode based on orbital resonances involving the HOMO and HOMO-1. Variation of the anchoring groups thus can be used to enhance the rectification ratio.

Wang and coworkers have demonstrated experimentally a high rectification ratio for a benzene molecule terminated with different thiol and amine groups [51]. They

were able to show, see Fig. 1.4, that the energy gap obtained from Landauer fitting matches closely with results from transition voltage spectroscopy. Moreover, application of the Simmons model implies that the asymmetry of the potential drop across the asymmetric anchoring groups is the origin of the observed rectification.

1.3 Negative differential conductance

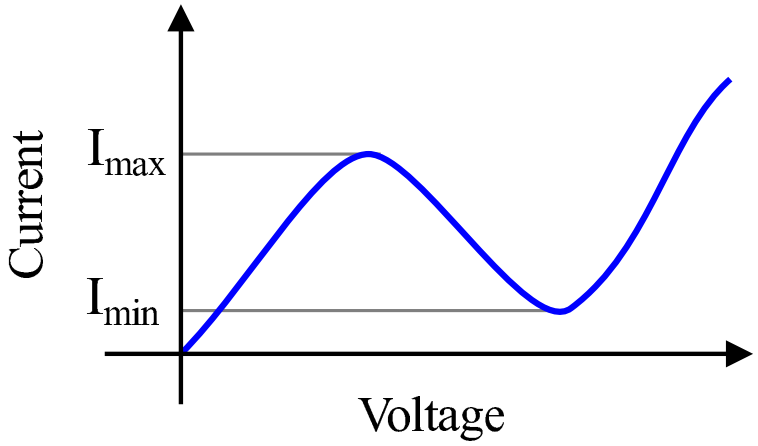

Figure 1.5: Schematic I-V curve in the NDC case.

Negative differential conductance (NDC) devices promise multifunctional (non-linear) operations due to the non-linear I-V characteristics shown in Fig. 1.5. A low NDC voltage (peak voltage) is favorable in order to minimize the device power consumption and a high peak-to-valley ratio (ratio between the peak and valley currents) is favorable for switching and amplification.

Zhu and coworkers have observed NDC in a benzene molecular junction, as a result of charge redistribution and Coulomb blockade at the contact to the electrode [52]. This gives rise to potential applications in nanoscale current modulators. The NDC region can be shifted to lower bias by application of a gate voltage, which also strongly enhances the peak-to-valley ratio [53]. In this study a C_{60} dimer was sandwiched between Au(111) electrodes in a field effect transistor arrangement. The

frontier molecular orbitals turn out to be shifted towards the Fermi level, while the transmission peak is reduced in intensity. Using the scanning tunneling microscope break junction technique, Zhou and coworkers [54] probed molecular junctions composed of thiol-terminated Ru(II) bis-terpyridine between Au electrodes, varying the anchoring group. They found NDC (at a low bias of ~ 0.6 V) only for one of three tested anchoring groups and explained their observations by bias induced changes in the coupling between molecule and electrodes.

1.4 Magnetoresistance

Spin-polarized transport is gaining increasing interest because it paves the way to downsizing of electronic components and lowering the power consumption. The field of spintronics (spin electronics) largely started with the discovery that the resistance of ferromagnetic layers separated by a thin non-magnetic spacer can be controlled by an external magnetic field or a current [55]. In the case of a metallic spacer the effect is known as giant magnetoresistance and for ultra thin insulating layers spacers as tunneling magnetoresistance. A large anistropic magnetoresistance recently was found at room temperature for terephthalic acid interfaces with Fe [56]. First-principles quantum simulations show that the effect originates from dependence of the coupling at the contacts to the electrodes on the orientation of the Fe magnetization with respect to the direction of the current.

Wiel and coworkers have studied molecular wires formed by sublimating organic dye molecules into the channels of zeolite crystals in the presence of K counterions [57]. An ultra high magnetoresistance observed at room temperature appears to be connected to the one-dimensional character of the system. High magnetoresistance can be achieved in topological line defects in graphene by Mn decoration due to strong

induced π magnetism [13]. The dependence of the magnetoresistance of manganese phthalocyanine contacted by a Co tip in a scanning tunneling microscope on the separation between the tip and the molecule has been investigated in Ref. [58].

Chapter 2

Theoretical Methodology

2.1 Density Functional Theory

Density functional theory (DFT) is a theory of correlated many-body systems [59]. The fundamental tenet of density functional theory is that any property of an atomistic system of many interacting particles can be viewed as a functional of its ground state density $n_0(r)$, which in principle determines all the information in the many-body wave functions for the ground state.

2.1.1 The Hamiltonian

The electronic structure of molecules and solids is described in terms of the ions and valence electrons. The ions are composed of the nuclei and tightly bound core electrons. The charge on each nuclei is $Z \cdot e$, where Z denotes the atomic number of the particular chemical element and e is the electronic charge. Assuming that the core electrons do not contribute to the transport properties of the material, then, only the valence electrons are responsible for conductivity and other electronic properties. Also, the separation to ions and valence electrons is an idealization, this allows for the description of the interacting ions and electrons. In order to describe the electronic

properties of the system, the hamiltonian of the system can be defined as

$$H = H_{ion} + H_{el} + H_{ion-el} \tag{2.1}$$

where H_{ion} defines the ionic sub-system, H_{el} the electronic sub-system, and H_{ion-el} the coupled ionic-electronic system. The ionic sub-system is composed of the kinetic energy H^k_{ion} of the ions and the potential energy $H_{ion-ion}$ due to ion-ion Coulomb interaction.

$$H_{ion} = H^k_{ion} + H_{ion-ion} = \frac{1}{2}\sum_{\mu}\left(-\frac{\hbar^2}{M_\mu}\nabla^2_\mu + \frac{e^2}{4\pi\epsilon_0}\sum_{\mu\neq v}\frac{Z_{val,\mu}\ Z_{val,v}}{|R_\mu - R_v|}\right) \tag{2.2}$$

Similarly, the Hamiltonian of the electronic sub-system is written as

$$H_{ion} = H^k_{el} + H_{el-el} = \frac{1}{2}\sum_{i}\left(-\frac{\hbar^2}{m}\nabla^2_i + \frac{e^2}{4\pi\epsilon_0}\sum_{i\neq j}\frac{1}{|r_i - r_j|}\right) \tag{2.3}$$

Also, the coupled ionic-electronic system is given by the energy due to Coulomb interaction between the ion and electron

$$H_{ion-el} = -\frac{e^2}{4\pi\epsilon_0}\sum_{\mu}\sum_{i}\frac{Z_{val,\mu}}{|R_\mu - r_i|} \tag{2.4}$$

The masses and positions of the ions and electrons are represented by (M_μ, R_μ) and (m, r_i) respectively.

The solution to the problem $|\Psi(r, R)\rangle$ is given by solving the eigenvalue problem poised by the Schrödinger equation

$$H\,|\Psi(r, R)\rangle = \mathcal{E}\,|\Psi(r, R)\rangle \tag{2.5}$$

The wavefunction of the many particle system is given by

$$\Psi_\gamma(r_i, R_\mu) = \sum_\alpha \phi_{\gamma\alpha}(\{R_\mu\})\psi_\alpha(r_i, R_\mu) \tag{2.6}$$

The complete degree of freedom of the ionic and electronic coordinates is embedded in the full hamiltonian Eqn. (2.1). In order to solve this many body problem whose exact solution is difficult, the Born-Oppenheimer approximation [60] is used to effectively decouple the ionic component of the hamiltonian from the electronic part. This approximation is based on the fact that the ions are much heavier than the electrons. Hence, the electrons move much faster compared to the ions, during this motion, the electrons tend to adjust their relative position with respect to the ions. Considering the ionic motion with respect to the electrons, it is imperative to say that the ions do not move. To this effect, we decouple the electronic and ionic degree of freedom. Considering the ions fixed at position $\{R_\mu\}$, the Schrödinger equation for the electronic problem is given by

$$\left(H_{el}^k + H_{ion-el}\right)\psi_\alpha(r_i, R_\mu) = E_\alpha(\{R_\mu\})\psi_\alpha(r_i, R_\mu) \tag{2.7}$$

and the ionic degree gives

$$\left(H_{ion}^k + E_\alpha(\{R_\mu\})\right)\phi_{\gamma\alpha}(R_\mu) = \mathcal{E}_\gamma\ \phi_{\gamma\alpha}(R_\mu) \tag{2.8}$$

The different time scales of the ionic and electronic degree of freedom can be seen from the fact that Eqn. (2.7) does not contain the dynamics of the ionic degree and the fact that the ionic equation, Eqn. (2.8), have the total energy of the electronic sub-system and not the individual energies.

By the re-writing of the Born-Oppenheimer approximation, we are able to con-

centrate on the electronic problem. This is because the ion-ion interaction gives rise to a constant additive contribution of energy to the electronic energies. Hence we can re-write Eqn. (2.1)

$$H = H_0 + H_{ext} \tag{2.9}$$

where

$$H_0 = H_{el-el} + H_{el}(\{r_i\}) + H_{ion-el}(\{r_i\})$$

and

$$H_{ext} = H_{ion-ion} + H_{ion-el}.$$

The many-body interacting system is reduced to finding the solution of an electronic Schrödinger equation within the DFT. The electron density n is the central variable in the DFT. The electron density operator is defined in terms of field operators. We denote spin index by σ as

$$\hat{n}(r) = \sum_{\sigma} \hat{n}(r) = \sum_{\sigma} \hat{\psi}^{\dagger}_{\sigma}(r)\hat{\psi}_{\sigma}(r). \tag{2.10}$$

The Hamiltonian thus can be re-written in terms of the field operators and electron density operator $\hat{n}$

$$H^k_{el} = \sum_{\sigma} \int d^3r \hat{\psi}^{\dagger}_{\sigma} \left(-\frac{\hbar^2}{2m}\nabla^2 \right) \hat{\psi}_{\sigma}(r) \tag{2.11}$$

$$H_{el-el} = \frac{1}{2}\frac{e^2}{4\pi\epsilon_0} \sum_{\sigma\sigma'} \int d^3r \int d^3r' \hat{\psi}^{\dagger}_{\sigma}(r)\hat{\psi}^{\dagger}_{\sigma'}(r')\frac{1}{|r-r'|}\hat{\psi}_{\sigma'}(r')\hat{\psi}_{\sigma}(r) \tag{2.12}$$

$$H_{ext} = \int d^3r \left(\frac{1}{2N}\frac{e^2}{4\pi\epsilon_0} \sum_{\mu\neq\upsilon} \frac{Z_{val,\mu}Z_{val,\upsilon}}{|R_\mu - R_\upsilon|} - \frac{e^2}{4\pi\epsilon_0}\sum_{\mu}\frac{Z_{val,\mu}}{|R_\mu - r|} \right) \hat{n}(r) \tag{2.13}$$

$$= \int d^3r \; V_{ext} \; \hat{n}(r). \tag{2.14}$$

2.1.2 The Hohenberg-Kohn Theorems

The problem of solving the many body interacting system is reduced to a single particle problem within the framework of DFT, where finding accurate approximations to the energy functional is important. The DFT is based on two theorems first proved by Hohenberg and Kohn [61].

Theorem 2.1.1. *For any system of interacting particles in an external potential $V_{ext}(r)$, the potential $V_{ext}(r)$ is determined uniquely, except for a constant, by the ground state particle density $n_0(r)$.*

Corollary 2.1.2. *Since the hamiltonian is thus fully determined, except for a constant shift of the energy, it follows that the many-body wave functions for all states (ground and excited) are determined.* Therefore all properties of the system are completely determined given only the ground stated density $n_0(r)$.

Theorem 2.1.3. *The total energy functional $E[n(r)]$ has a minimum at the correct ground state electron density $n_0(r)$.*

$$E[n_0(r)] < E[n(r)]. \tag{2.15}$$

Corollary 2.1.4. *The energy functional $E[n(r)]$ is enough to determine the exact ground state energy and density.*

From theorem 2.1.1, Hohenberg and Kohn (HK) showed that the external potential is a function of the electronic ground state (GS) density given by $n(r) = \langle\psi|\hat{n}(r)|\psi\rangle$, for which ψ is the ground state wave function and $\hat{n}(r)$ is the density operator. Mathematically, the energy of the system can be expressed as a functional of density [61]

$$E[n] = F_{HK}[n] + \int V_{ext}(n)\hat{n}(r)d^3r \tag{2.16}$$

where $F_{HK}[n]$ is a universal functional because it does not depend on the external potential, but it is a function of the sum of the kinetic T and potential V energy operators of the electron-electron interaction.

$$F_{HK}[n] = \langle \psi[n] | T + V | \phi[n] \rangle \tag{2.17}$$

HK showed in theorem 2.1.3 that the GS density of the system is the one which minimizes the $E[n]$, and also the minimum $E[n]$ is the GS energy E_0. The exact form of the functional is unknown, but it is known to be a function of the density and this simplifies it. One year after HK paper, Kohn and Sham (KS) [61] were able to show a practical means to solve the problem, for which they earned the Nobel Prize. The idea is to consider an auxiliary non-interacting system whose density is the same as the one of the real system. The wave form of the non-interacting system is known as the Kohn Sham Orbital $\phi_i(r)$ and they obey the orthogonality condition.

$$\int \phi_i^*(r)\phi_j(r)dr = \delta_{ij}$$

The electron density is defined as

$$n(r) = \sum_i |\phi_i(r)|^2$$

Considering the energy functional for which $T_0[n]$ is the GS kinetic energy of the auxiliary non-interacting system, $E_H[n]$ is the repulsive electrostatic energy of the classical charge distribution $n(r)$ and $E_{XC}[n]$ is the exchange-correlation (XC) energy. Applying the variational principle to minimize the energy functional and using the orthogonality condition as a constraint, one finds a set of one-particle Schrödinger

equations;

$$\left[\frac{1}{2}\nabla^2 + V_{KS}\right]\phi_i(r) = \varepsilon_i\phi_i(r) \tag{2.18}$$

where the Kohn-Sham (KS) potential is given by

$$V_{KS} = V_{ext}(r) + \int \frac{n(r')}{|r-r'|}dr' + V_{XC}(r); \tag{2.19}$$

$$V_{XC} = \frac{\delta E_{XC}[n]}{\delta n(r)} \tag{2.20}$$

and

$$n(r) = \sum_{i=1}^{\infty} f(\epsilon_i - \epsilon_F)|\phi_i(r)|^2 \tag{2.21}$$

These equations are the famous KS equations, which must be solved self-consistently. V_{KS} is a functional of the electron density and $f(\alpha)$ is the Fermi-Dirac distribution for $\alpha = \epsilon_i - \epsilon_F$ where the Fermi energy is ϵ_F. Upon the achievement of convergence, the electronic energy of the system is given by

$$E = \sum_{i=1}^{N} f(\epsilon_i - \epsilon_F)\epsilon_i - \frac{1}{2}\int \frac{n(r)n(r')}{|r-r'|}dr + E_{XC}[n] - \int V_{xc}n(r)dr + E_{ion} \tag{2.22}$$

where E_{ion} is the ionic electrostatic repulsion energy. This would be the exact electronic ground state energy of the system if the exact $E_{XC}[n]$ is known [62].

2.1.3 Exchange-Correlation Functionals

The Kohn-Sham formalism is exact based on the assumption that the exchange-correlation potential $V_{XC}[n](r)$ can be determined exactly, which in principle is not the case. To this effect, different approximations have been developed for exchange functional that work well for some systems. Considering the fact that the $V_{XC}[n](r)$ functional of the density $n(r)$ at a point r is dependent on the position r' of density

$n(r')$ the need for an approximation becomes relevant.

Local Density Approximation

The LDA is a useful approximation to the exchange-correlation functional, where the homogeneous interacting electron gas is used to model the unknown energy contributions. The exchange-correlation functional as used in this approximation depends on the position of the particle and the exchange-correlation energy per particle (ϵ_{XC}) integrated over the whole space.

$$E_{XC}^{LDA}[n(r)] = \int d^3r \; n(r) \; \epsilon_{XC} \; n(r) \tag{2.23}$$

Since the local electron density is evaluated from the homogeneous interacting electron gas, the inhomogeneous interacting electron gas is divided into small regions located at positions r, each containing a homogeneous interacting electron gas with some average density $n(r)$. This approximation is exact within the limit of constant charge density. Experience has shown that metals are much more accounted for within this approximation due to a high mobility of charge carriers as compared to its agreement with semiconductors and insulators [63].

Generalized Gradient Approximation

The local density approximation fails in situations where the density undergoes rapid changes because it approximates the energy of the true density by the energy of a local constant density. In order to correct this situation, the Generalized Gradient Approximation (GGA) have been introduced, which takes into account the density

and gradient of the density.

$$E_{XC}^{GGA} = E_{XC}^{GGA}[n(r), \nabla n(r)] \tag{2.24}$$

Moreover, it is an established fact that the GGA offers significant improvement in the treatment of molecules in terms of the atomization energies, energy barriers and total energy differences [64]. The GGA does have some drawbacks, such as overcorrecting the LDA predictions.

There exist different variants of the GGA functional of which various forms have been developed to deal with different kinds of systems (surfaces, defects, molecules etc), but the most readily available include Beck (B88) [65], Perdew and Wang (PW91) [66] and Perdew, Burke, and Enzerhof (PBE) [67].

2.1.4 Self Interaction Correction

One basic problem of the LDA and GGA is "self interaction" [59, 68] which arises from the fact that in the Hartree potential the integral is performed over the total density $n(r)$, which includes the spurious electrostatic interaction of each particle with itself. Therefore, in LDA and GGA the particle feels its own potential. Unlike the Hartree-Fock approach where the self interaction in the Hartree potential is exactly cancelled by the exchange term, exchange potential in LDA and GGA is approximated and therefore this cancellation is not complete, part of the unphysical self-interaction remains in the case of the LDA and GGA. This problem can be overcome by using exact functional for the exchange part of potential, so that by construction the self-interaction cancels out [59]. This approach is difficult to achieve as it might introduce spurious self-interaction. The many-body interacting system is reduced to the finding the solution of an electronic Schrodinger equation within the DFT. Above all, this

approach is computationally expensive.

In this work, we have applied the Atomic-Self Interaction Correction (ASIC) approximation [69–71]. This approach has been shown to give good results for a variety of systems and is computationally inexpensive. Importantly, the ASIC is shown to improve the ionization potential for molecules [72] compared to the LDA results. In the ASIC , an occupation dependent correction is added to the LDA exchange-correlation potential. This causes the occupied states to be shifted down to lower energies but does not affect unoccupied levels. This effectively corrects for the self-interaction error of the LDA exchange-correlation energy, which is overestimated for occupied states.

2.1.5 RKKY Exchange Interaction

Ruderman-Kittel-Kasuya-Yosida (RKKY) interaction is an indirect exchange interaction between two magnetic impurities in a nonmagnetic host. The RKKY energy can be obtained by second order perturbation theory, where the interaction Hamiltonian written for the interaction between the itinerant electrons and the localized spin is the perturbation term. Studies suggest that this type of interaction should oscillate and decay as impurity separation is increased and the oscillation rate is determined by the Fermi wavevector [73] of the host, while the decay depends on the dimensionality of the host and the magnetic impurity [73]. Assuming that the exchange interaction between the conduction electron of spin $\mathbf{s}$ at position $\mathbf{x_{el}}$ and a localized spin $\mathbf{S_i}$ at position $\mathbf{r_i}$ has a simple form

$$H_{int} = J\mathbf{s} \cdot \mathbf{S_i}\delta^{\mathbf{3}}(\mathbf{x_{el}} - \mathbf{r_i}) \tag{2.25}$$

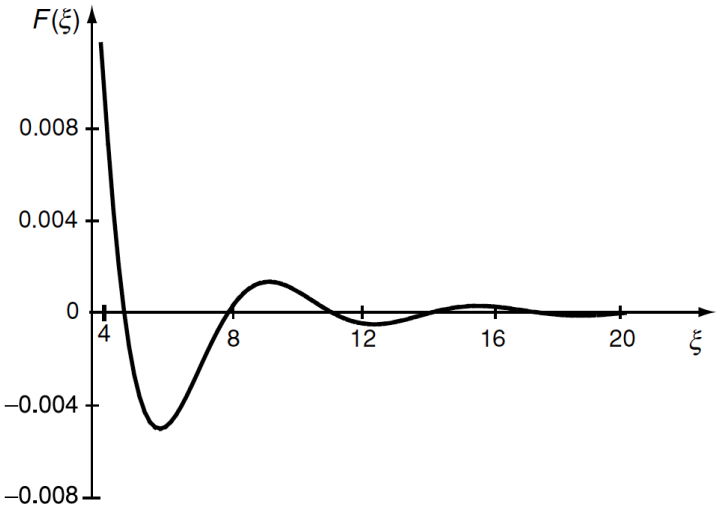

Figure 2.1: Schematic of the RKKY interaction as a function of distance between magnetic impurities.

Then, the effective interaction (H_{int}^{eff}) between two localized spins i and j separated by distance $\mathbf{R}$ is given by

$$H_{int}^{eff} = J^2 \mathbf{S}_i \cdot \mathbf{S}_j F(\xi), \tag{2.26}$$

where the *range function* $F(\xi)$ of the distance between the localized spins is

$$F(\xi) = \frac{\mathbf{m}^* \boldsymbol{\mu}_\mathbf{B}^\mathbf{2}}{\mathbf{h}^\mathbf{3}} \frac{(\mathbf{2k_F})^\mathbf{4}}{\boldsymbol{\xi}^\mathbf{4}} [\sin(\xi) - \xi \cos(\xi)] \tag{2.27}$$

and $\xi = 2k_F \mathbf{R}$.

RKKY interaction has been demonstrated in graphene decorated with impurity atoms. In undoped graphene a decay rate which is proportional to $\mathbf{R^{-3}}$ is seen for top and bridged adsorbed impurities, while a much faster decay rate proportional to $\mathbf{R^{-7}}$ is observed for center-adsorbed impurities [74, 75]. This decay rate is much faster than the $\mathbf{R^{-2}}$ expected for two dimensional materials because of the vanishing density of states at the Fermi energy of graphene.

2.2 SMEAGOL: *Ab initio* Quantum Transport Code

SMEAGOL is a linear scaling ab-initio quantum electronic transport code which combines both the DFT and non-equilibrium Green's function (NEGF) method. SMEAGOL uses SIESTA as interface for its DFT electronic structure platform [76, 77]. The NEGF scheme on which the SMEGOL is based can be interfaced with any DFT code that generates a Hamiltonian in tight-binding-like form. One of the advantages of using the SIESTA for its DFT part is that it constructs the Hamiltonian very efficiently, even for large systems. In fact, in the SIESTA this operation scales linearly with system size. Also, the SIESTA Hamiltonian and overlap matrices are constructed in the required tight-binding-like form.

The algorithm implemented in SMEAGOL is constructed taking into cognizance that the specific form of the Hamiltonian is irrelevant, once it is written as Linear Combination of Atomic Orbitals (LCAO) basis set which is a functional of the charge density. In SMEAGOL code, the combination of DFT and NEGF is a multistage transport process, which can be outlined as:

i. Infinite bulk contacts calculations of the Hamiltonain H^{ks}

ii. Obtaining the corresponding tight-binding representation of the converged H^{ks}

iii. Self-energies $\Sigma_{n,m}(\epsilon)$ calculations for the semi-infinite bulk leads

iv. Alignment of the chemical potential of the leads and the extended molecule region

v. Transport across the complete system.

Figure 2.2 shows a typical transport setup. The schematic shows a two-terminal device with two leads kept at different chemical potentials, which is able to exchange electrons with the central region (the extended molecule).

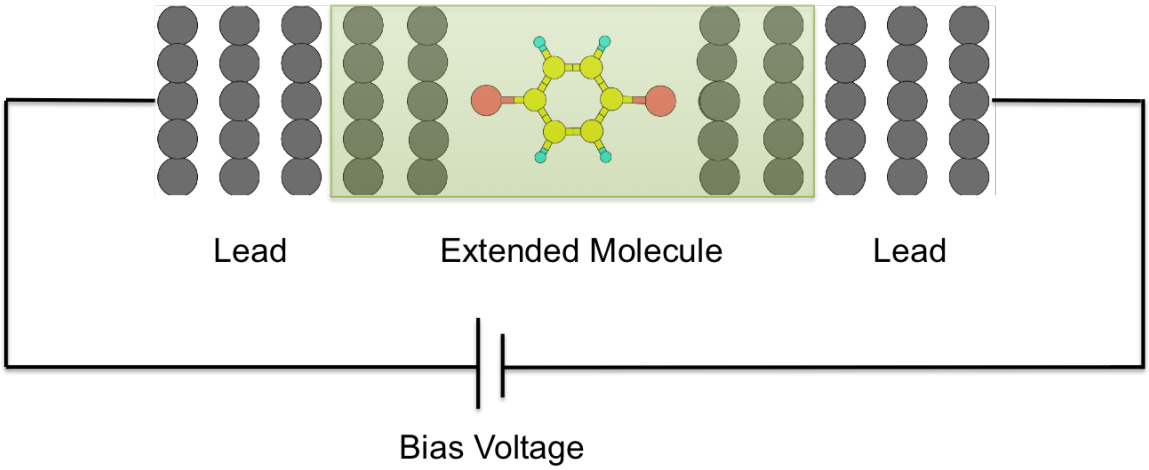

Figure 2.2: (Color online) Schematic representation of the transport setup. The greenish region represents the extended scattering region.

Figure 2.3 shows a general flowchart [78] of SMEAGOL and how it interfaces with the SIESTA code. The SIESTA code provides the KS Hamiltonian and SMEAGOL introduces the self-energies turning the system from periodic to a central scattering region attached to semi-infinite electrodes. SMEAGOL calculates the non-equilibrium charge density of an open system via Green's function approach. This non-equilibrium charge density is used to calculate the transport properties, for example, transmission coefficients and the current-voltage characteristics.

The section below briefly explains the underlying theory within the SMEAGOL code such as: Landauer formalism, non-equilibrium Green's function formalism (Green's function for the transport problem and the non-equilibrium properties), nudged elastic band method, and current induced forces. Also, we have calculated the current using the Landauer formalism presented in the section 2.2.1

2.2.1 Landauer Formalism

The Landauer approach is a scattering process where the device acts as a quantum mechanical scatterer for incoming electrons from the lead. Furthermore, the elec-

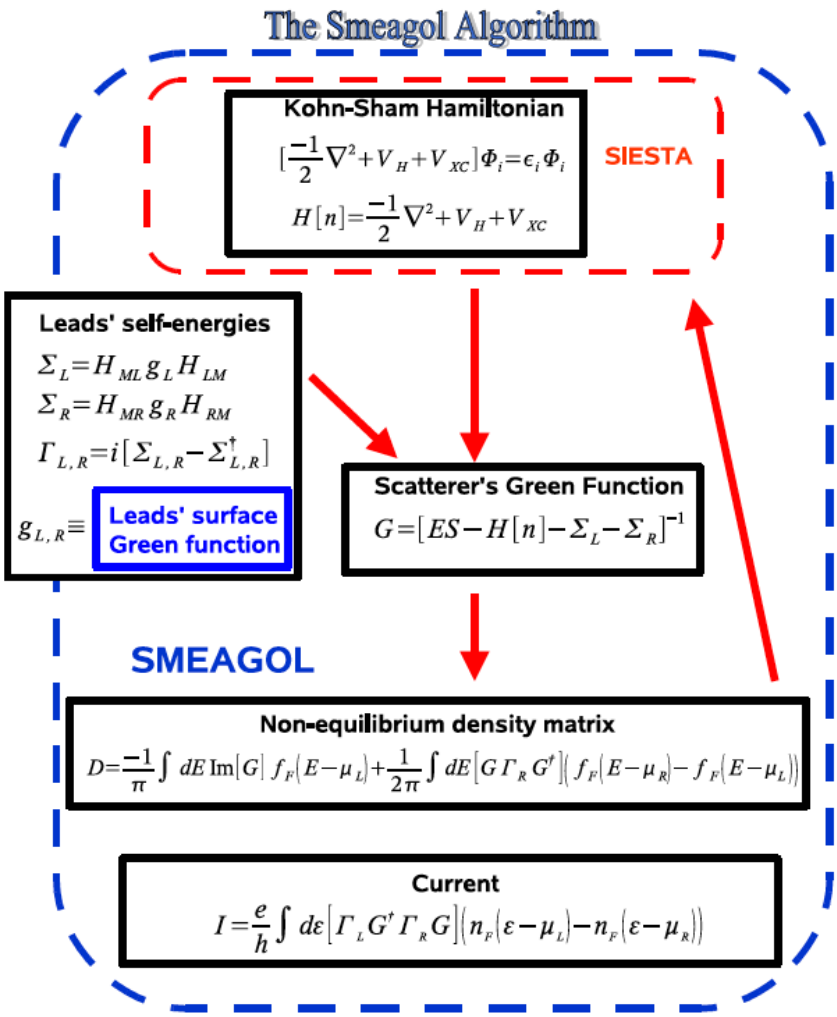

Figure 2.3: Flow chat of the SMEAGOL programme [78].

trons scatter elastically on the device (sample). The electrons through the device is described by the non-interacting quasi particles model. Three basic assumptions are considered in the derivation of the Landauer formalism:

i. The leads are semi-infinte.

ii. The reservoirs are reflectionless; that is, there is no interaction between the two leads a consequence of the fact that incoming electrons cannot be reflected back to the electrode.

iii. $\mu_L = eV + \mu_R$; consequently, μ_L is higher in energy to allow current flow.

Even though the leads are semi-infinite, they have finite width. Due to this finite width, the motion of the electrons perpendicular to the direction of the leads is quantized giving rise to a finite number of propagation modes or bands $\{\psi_{n,k}\}$ for a given energy.

The derivation of this approach applies to a system of electrons in which no inelastic scattering mechanisms are present. The transport is therefore assumed to be coherent. We will now present a derivation of the Landauer formula that is by no means rigorous, but nonetheless it shows what are the major assumptions in this approach.

In the reciprocal space, consider a single transverse mode, moving from the left to right electrode. The moving electron scatters in the scattering region. For simplicity, we assume a uniform electron gas with charged density n per unit length. The right moving current can be written as

$$I_L^{L\to R} = \frac{e}{L}\sum \nu f_L(E) = \frac{e}{L}\sum \frac{1}{\hbar}\frac{\partial E}{\partial k} f_L(E), \tag{2.28}$$

where ν is the velocity of the electron with energy E and the $f_L(E) = f(E-\mu_L)$ defines the Fermi-Dirac distribution function for the left electrode. Mathematically transforming the sum to integral

$$\sum_k \to \sigma \times \frac{L}{2\pi}\int dk, \tag{2.29}$$

where σ (spin) = 2, Eqn. (2.28) becomes

$$I_L^{L\to R} = \frac{2e}{h}\int f_L(E)dE. \tag{2.30}$$

The transmission probability through the scattering region is denoted by T, and then, the reflection probability is defined as $1-T$. From Eqn. 2.30, the left-moving current can be written as:

$$I_L^{R\to L} = \frac{2e}{h}\int \left[f_L(E)(1-T) + f_R(E)T\right] dE, \tag{2.31}$$

Eqn. 2.31 consist of two parts, the states back-scattered and the transmitted states from the right lead. Finally, the total current is given by

$$I_L^{total} = I_L^{L\to R} + I_L^{R\to L} = \frac{2e}{h}\int \left[f_L(E) - f_R(E)\right] T dE, \tag{2.32}$$

Within the linear response regime, the $f(E-\mu_{L/R}) \approx \mu_{L/R}$. This implies that the total current for an electron to move from the left electrode can be rewritten as

$$I_L^{total} = \frac{2e}{h} T\left[\mu_L - \mu_R\right] dE. \tag{2.33}$$

Since current flows as a result in difference in chemical potential $\mu_L - \mu_R = eV$, the conductance of the system is given as $G = \dfrac{2e^2}{h}T$. Hence, this result can be generalized for a multichannel system to be

$$G = \frac{2e^2}{h}\sum_i T_i \tag{2.34}$$

where i is the number of channel. This relation that relates the current to the transmission probability for electrons to transverse elastically through the conductor is the Landauer formalism [79], and that which incorporates inelastic scattering is the Generalized Landauer theory [77, 79]. The bias dependent current is generally written as

Eqn. (2.35):

$$I(E;V) = \frac{2e}{h} \int [f_L(E) - f_R(E)]\, T(E;V) dE. \tag{2.35}$$

In quantum transport theory, the central problem is to calculate $T(E;V)$ for a given device Hamiltonian. An extra degree of complexity is added when bias is included.

2.2.2 Non-equilibrium Green's Function Formalism

Interestingly, the non-equilibrium Green's function (NEGF) approach within the density functional theory (DFT) is based on equilibrium DFT to describe the electronic structure. The advantage is its simplicity and computational ease [79–82]. Compared to the equilibrium approach (linear regime), the effect of external bias on the electronic structure and consequently on the electronic transport properties is addressed below.

$$\left[\epsilon^{\dagger} S - H\right] G^R(E) = I, \tag{2.36}$$

where all matrices have infinite dimension (i.e I, H, S, G) and $\epsilon^{\dagger} = \lim_{\delta \to 0^{\dagger}} E + i\delta$ given that E is the energy.

First, we demonstrate the basic properties of Green's function. Assume that the system can be describe by a single particle Hamiltonian:

$$H\psi_i = E_i S \psi_i \tag{2.37}$$

where ψ_i is the state vectors whose dimension is $\mathcal{N}$, the eigenvalue E_i, and S is the overlap matrix. Both H and S are Hermitian, a consequence of the fact that E_i is real. The eigenvectors are normalized in such a way that $\psi_i^{\dagger} S \psi_j = \delta_{ij}$, which implies that the corresponding completeness relation is given by $\sum_i \psi_i^{\dagger} \psi_i S = \mathbb{1}_{\mathcal{N}}$, where $\mathbb{1}_{\mathcal{N}}$

is an $\mathcal{N} \times \mathcal{N}$ identity matrix. Thus, the retarded Green's function [83, 84] is given by:

$$G^R(E) = \frac{1}{(E + i\delta)S - H} \ , \tag{2.38}$$

where $\delta \to 0^+$ is for the retarded Green's function (G^R), and the $\delta \to 0^-$ is for the advanced Green's function (G^A). This implies that for real values of the eigenvalues; E, $G^A = G^\dagger$. For simplicity, we drop the "R" indicating the retarded Green's function. Rewriting the Hamiltonian in the spectral form we have

$$H = \sum_i^{\mathcal{N}} E_i S \psi_i \psi_i^\dagger S, \tag{2.39}$$

and the corresponding Greens function is given by

$$G(E) = \sum_i^{\mathcal{N}} \frac{1}{(E + i\delta) - E_i} \psi_i \psi_i^\dagger. \tag{2.40}$$

The spectral function, which is generalized density of states [83, 84] is defined as:

$$A(E) = i \left[G(E) - G^\dagger(E) \right]. \tag{2.41}$$

Eqn. 2.41 can be re-written using the spectral representation of the Green's function as defined in Eqn. 2.40. Doing this, we have,

$$A(E) = \sum_i^{\mathcal{N}} \left[\frac{1}{(E + i\delta) - E_i} \psi_i \psi_i^\dagger - \frac{1}{(E - i\delta) - E_i} \psi_i \psi_i^\dagger \right] = 2 \sum_i^{\mathcal{N}} \frac{\delta}{(E - E_i)^2 + \delta^2} \psi_i \psi_i^\dagger \tag{2.42}$$

The above Lorentzian becomes $A(E) = 2\pi \sum_i^{\mathcal{N}} \delta(E - E_i) \psi_i \psi_i^\dagger$ in the limit of $\delta \to 0^+$.

Green's Function for the Transport Problem

The device whose Green's function is determined is split into three parts; the left/right leads and the scattering region (also extended molecule). The extended molecule is the central device, which interacts with the leads. For simplicity, the leads are thermal bath in local thermal equilibrium with chemical potential $\mu_{L/R}$.

The Hamiltonian for the two terminal device is written in its matrix form:

$$H = \begin{pmatrix} H_L & H_{Ld} & H_{LR} \\ H_{dL} & H_d & H_{dR} \\ H_{RL} & H_{Rd} & H_R \end{pmatrix} \tag{2.43}$$

where H_{RL} and H_{LR} are equivalently zero matrices because this two blocks do not interact. $H_{L/R}$ represent the Hamiltonian of the isolated leads (left and right respectively), and H_d has the information of the device Hamiltonian. Since, the Hamiltonian is Hermitian, $H_{RL} = H_{LR}^{\dagger}$ and vice versa. And, the overlap matrix (S), have similar structure as the H matrix;

$$S = \begin{pmatrix} S_L & S_{Ld} & S_{LR} \\ S_{dL} & S_d & S_{dR} \\ S_{RL} & S_{Rd} & S_R \end{pmatrix} \tag{2.44}$$

In order to simplify the problem of Eqn. 2.36, we introduce the concept of the self-energies, and redefine the Green's function of the device in terms of the self-energies, giving rise to Eqn. 2.45

$$G_d = [E - H - \Sigma_L - \Sigma_R]^{-1} \ , \tag{2.45}$$

where the Σ_κ is the self-energy of the leads (κ = left/right leads) defined as $\Sigma_\kappa =$

$\Gamma_\kappa^\dagger g_\kappa \Gamma_\kappa$ (See Refs. [77, 84, 85] for derivation). These self-energies are a measure of the impact of the contacts on the device [86]. Ground states properties like the density can be obtained easily by using this approach. In order to evaluate this property, we need to evaluate the spectral function earlier defined in Eqn. 2.41

$$A_d = i\left[G_d - G_d^\dagger\right], \tag{2.46}$$

The spectral function of the device Eqn. 2.46 can be rewritten in terms of its self-energies, and the result is given below;

$$A_d = iG_d\left[G_d^{\dagger -1} - G_d^{-1}\right]G_d^\dagger = iG_d\left[\Sigma - \Sigma^\dagger\right]G_d^\dagger. \tag{2.47}$$

The in/out flow of current through the contacts is described by the coupling strength ($\Gamma_{L/R}$) [84], which is obtained from plugging Eqn. 2.45 into the spectral function of the device Eqn. 2.47

$$\Gamma_{L/R} = i\left(\Sigma_{L/R} - \Sigma_{L/R}^\dagger\right) \tag{2.48}$$

Note that the device may be in a non-equilibrium state, electrons are injected from the equilibrium reservoirs (the leads); the Fermi level is uniquely fixed for all carriers based on the applied voltage.

The Non-Equilibrium Properties

As mentioned in the previous section the transport calculation can be split into three regions, which are the leads (left and right) and the extended molecule. Though, this independent piece can be consider independently as equilibrium problem and when brought together the problem of the the contact introduces the out of equilibrium nature. However, as electrons continue to flow through the contact to equilibrate the

occupation, current flows. Practically, the equilibration of the electron requires an infinite time, a consequence of the infinite leads. But, a non-equilibrium steady state is achieved when the in/out flow of electron in the contact becomes same.

The basic idea is that the states in the leads are occupied up to a local Fermi level, and the occupation of the states in the extended molecule is then obtained by the difference between the inflowing and the outflowing electrons. Thus, the occupation of the states is determined by the chemical potential of the lead they originate from. The spectral function is rewritten in a form that maps each of the states of the system as originating form one particular leads. And, the Green's function allows the calculation of the density matrix of the device [78].

$$\rho_d = \frac{-i}{2\pi} \int dE G_d^<(E), \tag{2.49}$$

where the lesser Green function ($G_d^<$) [77, 83, 84, 87]of the device (extended molecule) is define as

$$G_d^<(E) = iG_d \left(\sum_i^{\mathcal{L}} \Gamma_i f_i(E) \right) G_d^\dagger \tag{2.50}$$

and $\mathcal{L}$ is the number of the leads, which is two for a two probe system. The current I across the device is defined [88]as

$$I = \frac{e}{h} \int dE \ \mathrm{Tr} \left[\Gamma_L G_d^\dagger \Gamma_L G_d \right] \left(f(x^+) - f(x^-) \right), \tag{2.51}$$

where $x^\pm = E \pm \mu_{L/R}$ and $\mathrm{Tr} \left[\Gamma_L G_d^\dagger \Gamma_L G_d \right]$ is analogous to the conductance for linear regime,

$$T(E;V) = \mathrm{Tr} \left[\Gamma_L G_d^\dagger \Gamma_L G_d \right]. \tag{2.52}$$

Hence, Eqn. 2.52 is the transmission coefficient, which is energy and bias dependent

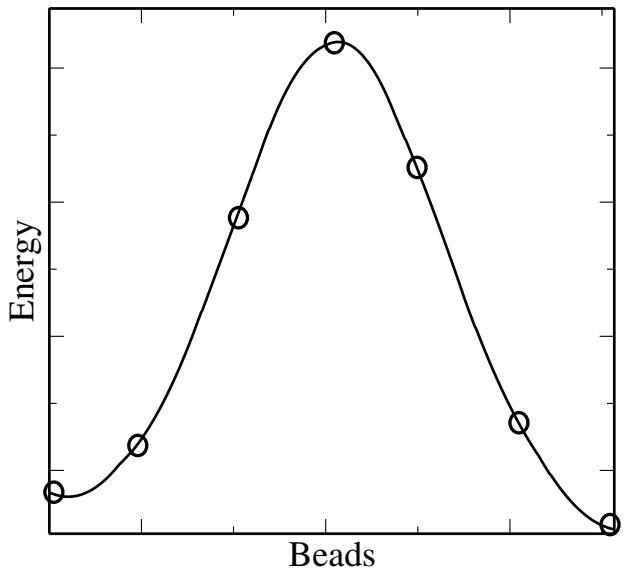

Figure 2.4: Schematic representation of the nudged elastic band (NEB) where empty cycles represent the point of the beads.

in more general non-equilibrium state.

2.2.3 Nudged Elastic Band Method

The NEB is a method for finding saddle points and Minimum Energy Paths (MEP) between two known metastable states (e.g, reactants and products as in chemical reactions) [89]. This approach of finding path between two states is done by optimizing a number of intermediate images along the path. Each image finds the lowest energy possible while maintaining quasi equal spacing to neighboring images (or beads) [90]. This constrained optimization is achieved by adding spring forces along the band between images and by projecting out the component of the force due to the potential perpendicular to the band.

Moreover, the NEB method stands out of other elastic band methods of finding the minimum energy path because it uses the force projection method, which ensures that the spring forces do not interfere with the convergence of the elastic bands to the MEP. This also makes sure that the true forces do not affect the distribution of

the images along the MEP. During minimization, the tangent to the path for each image of the true and spring forces is decomposed to its parallel and perpendicular component.

The NEB is a chain-of-states method. In this method, a string of geometric images of a system describes a reaction pathway. These geometric images are connected by spring forces, which ensures equal spacing. Once, the NEB is converged to the MEP, the reaction mechanism is described by the images up to the resolution of the images (see Fig. 2.4). The initial and final states are known at the start of the NEB calculation. First, a linear pathway connecting the end states is typically used, but in some cases other choices might be preferred. For instance, a geometric repulsive force is used to push atoms apart should they get too close to each other, this could result to a band with lower initial forces. A more suitable initial pathway is possible from an interpolation of internal coordinates, for instance, if the reaction involves rotational motion. This is also possible if the reaction goes through an intermediate state.

Fig. 2.4 shows the two metastable states as the end points of the curve and the cycles represent the different beads which define the path between the two metastable states.

2.2.4 Current-Induced Forces

Current-induced forces is the phenomenon associated with the interaction between electrons and ions in the presence of current. In other words, the current-induced forces are due to the momentum that the electrons transfer to ions during current flow. From a static point of view, the steady-state electron density in a current-carrying conductor is microscopically different from that in the absence of current. Current flow alters the forces. In microelectronics, this phenomenon is called electro-

migration and is a major device failure mechanism in interconnects [91]. Moreover, electromigration may become of significant concern since nanoscale conductors may carry current densities much larger than their macroscopic equivalents. This may occur due to two processes: (i) as a result of electrons transferring only momentum to the ions without energy (elastic process) and (ii) as a result of electrons transferring both momentum and energy to the ions (inelastic process).

The motion of atoms due to current flow has been extensively studied in the past both for its fundamental point of view and its importance in microelectronics [92–95]. Due to current induced breakdown in micro-electronics, a result of electromigration and other effects, the study of forces induced by current becomes of great importance. In order to investigate this phenomenon, the Kohn-Sham Hamiltonian $\hat{H}$ and its associated density matrix $\hat{\rho}_d$ (see Eqn. 2.50) are determined by the non-equilibrium Green's function formalism coupled with the density functional theory technique as implemented in SMEAGOL, the force acting on the n-th atom F_n is obtained by the Hellmann-Feynman theorem[96].

$$F_n = Tr[\hat{F}_n \hat{\rho}_d] - \frac{\delta \hat{H}_{nn}}{\delta \mathbf{R_n}} \quad with \quad \hat{F}_n = -\frac{\delta \hat{H}}{\delta \mathbf{R_n}}, \tag{2.53}$$

where $\hat{F}_n$ is the force operator with respect to the nth atom, $\mathbf{R_n}$ is the position of the n-th atom, and H_{nn} is the interaction between atoms. From Eqn. (2.53), the first term is the usual Hellmann-Feymann contribution to the force due to localized electronic states, while the second term is the contribution to the force due to the continuum states [96, 97]. The continuum integration covers the part of the spectrum occupied by the electrons at a given bias [96].

The origin of this force is linked to the bond charge or overlap population in the system, and the redistribution of the electronic charge due to the voltage, which

results in an asymmetric voltage drop, leading to current induced forces [98]. It is worth mentioning that the current-induced forces have been understood by separating it into direct and wind forces, however this separation is arbitrary and in this thesis we have not separated the forces in this fashion. The direct force is usually attributed to the electrostatic force due to the electrostatic field that drives the electron current on the bare positive charge of the ion. Also, the wind force is a result of the net momentum transfer from the electron current due to the scattering electrons on the ions.

The question of why bother about the conservativeness of current-induced forces may arise. If current-induced forces are not conservative, the conventional notion of phonons will be lost under current [99]. This is because the cross products of the ionic potential with ionic positions are not necessarily equal (see Eqn. 2.54), hence the dynamical response matrix for a current-carrying wire structure is not necessarily symmetric.

$$\frac{\partial^2 V_{ion}(R_i - R_j)}{\partial R_{i\mu} \partial R_{j\nu}} \neq \frac{\partial^2 V_{ion}(R_i - R_j)}{\partial R_{j\mu} \partial R_{i\nu}} \tag{2.54}$$

This leads us to the question: Are current-induced forces conservative [100]? First, by conservativeness of force we mean that the work done across a close path is zero (i.e., $\nabla \times \mathbf{F} = 0$). In other words, the force can be written as a simple gradient of a potential ($\mathbf{F} = -\nabla V$). In the past, current induced forces have been strongly argued to be conservative [96, 101]. They proposed that the force can be written as derivatives of appropriate energy functionals by either mapping the force problem as a variational one [96] or maximizing an appropriate entropy functions [101].However, current-induced forces have been shown to be generally non-conservative [100]. For instance, Dundas et. al [18] showed that the current-induced forces are non-conservative and can be used to drive an atomic scale waterwheel. In their work, they showed that

the curl of the force vanishes at equilibrium but it is nonzero in the present of current. They also demonstrated that the force is not the gradient of a potential. As a result of the non-conservativeness of the current-induced forces, also shown is the fact that the circular motion of an atom, or a group of atoms, can transfer energy from the electronic sub-system to the atoms; increasing the energy of the atomic system after each revolution. Hsu and co workers [41] recently showed that the current-induced forces can be used to do useful work. They were able to cause an asymmetrically coupled benzene-Pt to rotate as a stream of water rotates a waterwheel in the presence of current. The force exerted is a result of large current density because of reduced distance between Pt (from electrodes) and C atoms of benzene in the lower part of the ring.

2.2.5 Mechanism for Negative Differential Conductance

Negative differential conductance, which results from the corresponding decrease in current with increasing voltage have been explained using different models. Rakshit et al. [102] considered a molecule bounded between a p-type semiconductor with well-defined resonance positioned (E_m) below the Fermi energy (E_F) that is located at the valence band of Si (see Fig. 2.5(a)). Initially, this molecular level is not in the bias window. A positive current causes the molecular level to move upward towards E_F and eventually aligning with it, hence a large current (Fig. 2.5(b)). With further increase in bias, the molecular level lifts into the band gap, prohibiting carrier flow through the level, resulting in a drop in current and NDC, Fig. 2.5(c).

Perrin et al. [104] in a letter published in the Nature Nanotechnology, gave insight into their observed NDC using a two site model. They first isolated two very close molecular orbitals (HOMO and HOMO-1) by taking a simple addition and subtraction

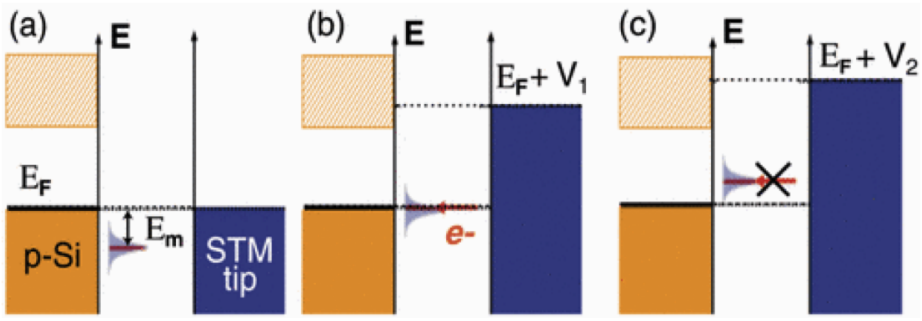

Figure 2.5: Schematic depiction of resonant tunneling mechanism for NDC. (a) zero bias, (b) moleuclar level at resonance with E_F ($V \uparrow$, $I \uparrow$), and (c) molecular level driven into the band gap ($V \uparrow$, $I \downarrow$) [102, 103]. The arrows indicate direction.

of the molecular level to create two localized molecular orbitals (LMO) sitting in two ends of the molecule. The LMOs are located on each side of the molecule, implying that the junction can be modelled by a two site model weakly coupled by τ (see Fig. 2.6). The two sites are coupled to the leads on each side by Γ. At zero bias, the conductance is high because of the symmetry of the molecule, which makes the energies ϵ_L and ϵ_R to be in resonance. However, upon application of bias the sites are separated by αeV (where α is a fractional voltage drop inside the molecule). This offset resonance condition induced by bias voltage leads to a reduction of elastic transport through the molecule, lowering the conductance. The transmission coefficient as calculated by the two site model is given by:

$$T(E) = \frac{(2\tau)^2}{(\Gamma/2)^2} \frac{(\Gamma/2)^2}{(\epsilon - \epsilon_L)^2 + (\Gamma/2)^2} \frac{(\Gamma/2)^2}{(\epsilon - \epsilon_R)^2 + (\Gamma/2)^2} \tag{2.55}$$

Chen et al. [105] exploited a two-step reduction process that modifies charge transport through a molecule as a candidate mechanism for NDC. In their work, the molecule initially undergoes a one-electron reduction, thereby supplying a charge carrier for electron flow through the system during finite bias. Further increasing the bias causes additional reduction with subsequent blocking of the current. The molecule considered constitute a nitro moiety, which is the most electron-withdrawing

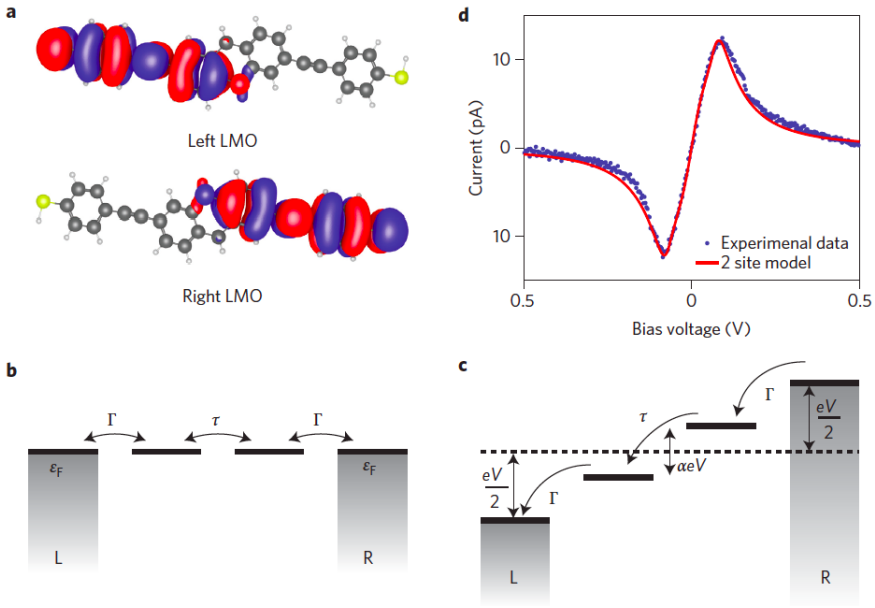

Figure 2.6: (a) Shows the left and right LMO obtained by addition and subtraction of HOMO and HOMO-1 orbitals, (b) shows the LMO's represented by the two site model, whose energies are weakly coupled by τ and each coupled to the electrodes by Γ, (c) depicts the offset resonance on application of bias voltage, and (d) shows the close matching nature of I-V characteristics of the molecule of the model and experiment [104]

group in the molecule. In other words, this is due to Coulomb blockade. Consider a two level model with highest occupied molecular orbital (HOMO) and the lowest unoccupied molecular orbital (LUMO). We consider the LUMO is weakly coupled to the right electrode ($\gamma_{2,R}$). Once the applied voltage reaches the LUMO level, it begins to fill. However, because it is now harder for electrons to leave the LUMO due to the weak coupling to the right electrode and considering the fact that double-occupation is forbidden because of Coulomb repulsion, the HOMO level begins to empty its electrons at a much faster rate than the LUMO level, resulting in depletion of the former. In this scenario, the resulting current from the LUMO is not enough to compensate for the reduction in current due to HOMO level depletion, and therefore, the overall current decreases with increasing voltage leading to NDC behavior.

Under low bias, bands within the vicinity of the Fermi energy are responsible for

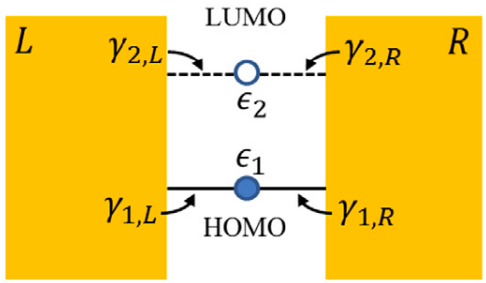

Figure 2.7: Effective two-level model, where the coupling between the LUMO and the electrode is weak [106].

the transport properties. Xiao-Fei et al. [107] demonstrated that half filled energy bands can lead to NDC under low bias. Fig. 2.8 shows the overlap degree of the half filled energy bands in the left and right electrode. And, the same Fermi energy guarantees that the overlap degree is maximum at zero bias resulting in the widest transmission flat. Applying bias voltage shifts the electrochemical potential of the leads by $(V/2)$. Therefore, causing a reduction in the degree of overlap, until eventually it becomes zero and then the transport channel supported by the half filled energy band is totally suppressed, hence the current reaches its deep. This mechanism applies to the observed NDC discussed in Chapter 6.

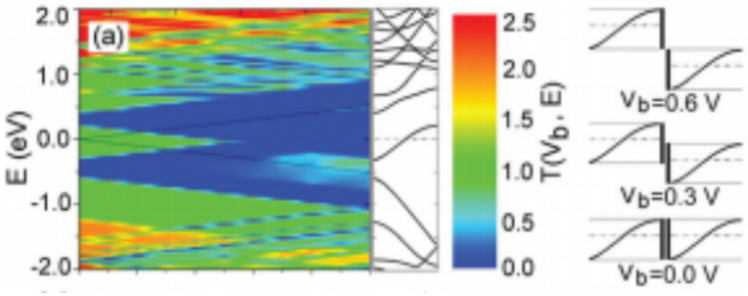

Figure 2.8: Left panel shows the bias dependent transmission coefficient and the right panel shows the overlap degree between the half filled energy bands of left and right electrodes under the bias of 0.0, 0.3, and 0.6 V [107].

Chapter 3

Hydrogen Bonding as the Origin of the Switching Behavior in Dithiolated Phenylene-vinylene Oligomers

Molecular electronics has gained significant interest over the last decade, and it is now considered as one of the potential strategies to integrate and/or replace conventional metal-oxide-semiconductor based electronics [108, 109]. Potentially organic molecules have many advantages over inorganic semiconductors. For instance they are cheap and can be processed in large quantities with low-temperature chemical methods instead of the expensive high-temperature techniques used in the conventional semiconductor industry. Molecules are available in an extremely wide range of chemical compositions and geometrical configurations and their properties can be changed dramatically by minor chemical substitutions. As such organic compounds form a versatile toolbox where the desired electronic properties can be engineered. Furthermore the ability of molecules to self-assemble makes them good candidates for applications where large

interconnectivity is needed [110]. Finally, the electronic properties of molecules can be manipulated by acting on multiple degrees of freedom such as the geometry [30], the spin [111], and the charging state [112]. It is then not surprising that a multitude of conventional electronic devices already has been demonstrated at the molecular level. This includes molecular switches, rectifiers and transistors [113–115].

A crucial issue with molecular electronics is that, despite the fact that molecules can be produced identical with extremely high yield, molecular devices are characterized by a much lower reproducibility. This is often so extreme that breaking junctions, where large statistics are collated, appear as the only way to extract general properties from a transport experiment [116]. The low reproducibility is associated with the difficulties of forming electrical contact between the molecules and the electrodes [117]. The relatively weak bonds and the fact that often there is a multitude of absorption sites and geometries with rather close binding energies [118] makes it difficult to form many identical junctions, even if the growing conditions are very stable. Although progresses have been made in the optimization of the molecule to electrodes bond [119], it is extremely unlikely that molecular junctions will ever reach the fidelity needed for ultra-dense mainstream logic. However, such high fidelity is not needed for bio-inspired computational protocols based on connectivity and junction bi-stability [120]. Furthermore, when such bi-stability is produced by some type of chemical reaction, molecular junctions become an interesting technological platform for chemical sensing [121].

There are therefore many different reasons to study molecular junctions that can be switched on and off by either the interaction with other molecules or with an electric current [30, 105, 122, 123]. In general there are two possible ways of generating a switchable device. One can start from a molecule presenting intrinsic bi-stability, where the two configurations are accessible by an external stimulus (for instance light),

sandwiched between two electrodes. If the bi-stability is preserved and the molecule can be switched in the junction, usually the two configurations can be associated to two different I-V characteristics [124, 125]. A second option is to start from a stable molecule, which develops bi-stability when incorporated in the junction [9]. Such acquired bi-stability can be related to geometry changes internal to the molecule [126, 127] or to the molecule-electrode bond [34]. Often these two possibilities are difficult to distinguish from each other, since the only evidence at hand is a change in conductance, and one has to rely on theoretical modeling.

In this work we explore one such switchable molecule, namely a dithiolated phenylenevinylene oligomere (opv3) sandwiched between gold electrodes. It has been demonstrated experimentally by Danilov *et al.* that opv3 can switch between a high (on) and a low (off) conductive state [34]. The mechanism for the switch was attributed to the protonation/de-protonation of the thiol groups linking the molecule to the electrodes. In particular the low conductance state was attributed to the protonated species (thiolate) and the high conductance state to the de-protonated species (thiol). However, theoretical calculations for the simpler benzene molecule attached to Au electrodes through either thiol or thiolate show a more complex situation, where the actual zero-bias conductance depends on the specific absorption site [128]. For this reason we have reviewed the mechanism proposed by Danilov *et al.* and found that the situation is actually reversed, i.e., the off state must be attributed to the thiol and the on state to the thiolate.

3.1 Computational Details

Two terminal devices with opv3 are constructed using a supercell geometry where oligophenyleneviylene derivates are embedded in the gap between two Au(111) sur-

faces, each consisting of five atomic layers. In the plane orthogonal to the transport the Au(111) surface is constructed with a 3×3 cell resulting in nine gold atoms per atomic layer, and supercells containing in total 130, 131, and 132 atoms for opv3, opv3H, and opv32H, respectively. As periodic boundary conditions are applied in the plane, the structure corresponds to 1/9 opv3 monolayer coverage, a molecular density, which guarantees that molecules residing in neighboring periodic cells do not interact with each other. In order to establish the relaxed geometries we use a two step process. In the first step we attach the molecule to two layers of Au on each side, include enough vacuum along the transport axis so that the thin Au slabs can move independently, and allow all atoms to relax. Afterwards a third Au layer is added on each side and the atoms (besides those in the third layers) are relaxed again. The geometries of all the oligophenyleneviylene derivatives on gold are optimized by using the density functional theory (DFT) conjugate gradient method as implemented in the SIESTA package [129]. The Brillouin zone is sampled with a 3×3 Monkhorst-Pack k-mesh in the plane of the surface, while the conjugate gradient procedure is considered converged when the forces are smaller than 0.02 eV/Å. The distance between the electrodes is optimised by relaxing the cells containing the different molecules as a function of the electrode separation. Thus we obtain equilibrium distances of 23 Å, 23.6 Å, and 23.6 Å, respectively, for opv3 attached to the electrodes by two thiol groups, by one thiol and one thioloate group, and by two thiolate groups.

The density matrix and all the operators are expanded over a numerical atomic orbitals basis set as defined in the SIESTA DFT code [130]. Here S, C, and H are described by a double-zeta polarized basis set. For Au the same basis is used for the geometrical relaxation, while a single-zeta polarized basis is employed for the transport calculations. The cutoff radii of the basis are assigned by imposing a global energy shift of 30 meV [129]. The core electrons of all the atoms involved are de-

scribed by norm conserving pseudopotentials generated with the Troullier and Martin scheme[131] including scalar relativistic corrections and written in a fully separable form.[132] The real-space grid cutoff has a corresponding cutoff energy of 600 Ry. The local density approximation (LDA) as parameterized by Ceperley and Alder [133] is employed for the exchange-correlation energy. However, in order to better reproduce the molecule gap between the HOMO and the LUMO, we have also performed calculations where SIC are included. In particular we use the atomic approximation with screening parameter $\alpha = 1$ [134]. The SIC corrects only occupied states, whereas its effect on empty states is not well defined. For the HOMO eigenvalues the removal of the self-interaction error results in a lowering of the energy. Such corrections improve also the level alignment of the junction and have been proved multi times to provide a better agreement between transport experiments and theory [14, 128, 135].

Electron transport calculations are performed at the optimized geometries using the non-equilibrium Green's function approach as implemented in the SMEAGOL package [76]. Since SMEAGOL interfaces directly with SIESTA, which provides the DFT platform for the method, the same convergence criteria used for the electronic structure calculations (basis set, grid cutoff, etc.) are also employed for the transport. The non-linear current through the junction is calculated using the Landauer formula in Eqn. 2.35. In Eqn. 2.35, V is the bias potential, which is applied symmetrically to the electrodes, i.e., $\mu_{L/R} = E_F \pm eV/2$, where E_F is the Fermi energy of the electrodes. Since $f(x)$ is the Fermi-Dirac distribution, Eq. (2.35) essentially establishes that the current at the voltage V is simply the integral of the V-dependent transmission coefficient, $T(E;V)$, over the energy window defined by the chemical potentials of the two electrodes, i.e., over the bias window.

Finally, in addition to the SIESTA convergence parameters a few more need to be set for the transport calculations. Here, the complex part of the integral leading to

the charge density is computed using 16 energy points on the complex semi-circle, 16 points along the line parallel to the real axis, and 16 poles. The integral over the real energies necessary at finite bias is evaluated over at least 500 points [76]. An electronic temperature of 300 K is used for all calculations.

3.2 Structural Analysis

A scheme of the device setups investigated in this work is presented in Fig. 3.1. In particular we have defined and investigated three configurations, namely opv3, opv3H, and opv32H. The first one refers to the phenylenevinylene oligomere bounded to the Au surfaces only via thiol groups, while the other two indicate that either one (opv3H) or two (opv32H) protonations have occurred. In both cases the additional H atom binds to the thiol site, thus transforming the ending group from thiol to thiolate.

As the transport properties of a molecule may vary with the contact geometry [128] it is important to establish the most relevant binding sites for the family of molecules under investigation. Previous exact quantum chemistry calculations[136] suggest that the S atom of the thiol group can be located either at the hollow or the top site of the gold surface. Theoretical work on the bonding of thiolates to Au found other sites (such as bridge sites) to be more favorable for some molecules [137, 138]. In particular, the binding to the hollow site has been shown to be energetically favorable when *sp* hybridization is at play. In this case the surface(Au)-S-C angle is 180^o [136, 138]. This is the starting binding geometry adopted in our calculations (the geometries are then optimized by the conjugate gradient method). The perpendicular distance between the S atom and the Au(111) surface plane for opv3 is optimized to 2.4 Å. This becomes 3.1 Å when a proton attaches to one of the thiol groups forming the opv3H molecule (note that the bond length for the remaining Au-thiol bond elongates

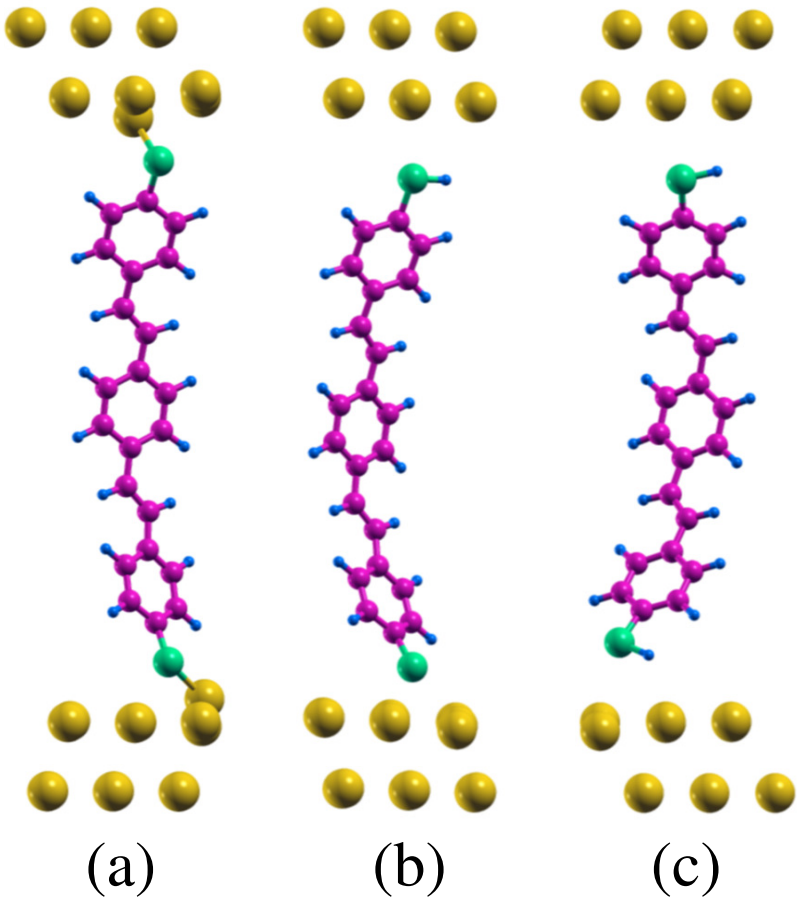

Figure 3.1: Schematic diagram of the devices investigated. These comprise various oligophenylenevinylene derivatives sandwiched between Au electrodes. Here we label as (a) opv3, (b) opv3H, and (c) opv32H, respectively, a oligophenylenevinylene molecule including either no, one, or two thiolate groups. Color code: blue=H, green=S, purple=C, and yellow=Au.

to 2.6 Å). Finally, when opv3 becomes doubly protonated (opv32H) both distances become 3.3 Å. For all the cases investigated we calculate the transport through both the trans-trans and the cis-trans isomers, which are shown in Fig. 3.2, although in general the two present rather similar transport properties. While we find that the energetically most favorable bonding site for opv32H is the hollow site, in general it is possible that the molecules bind at other sites. In order to elucidate the influence of the bonding site on the transport properties, we calculate the transmission across the trans-trans isomer of opv32H for different bonding sites and find that the resulting

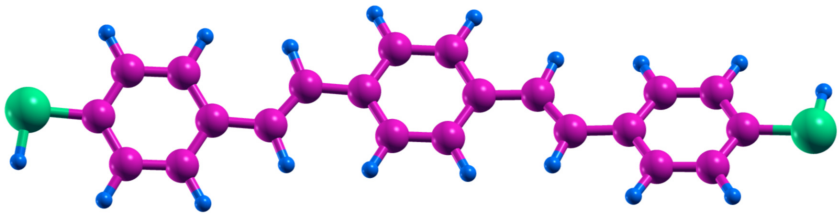

(a) cis–trans isomer

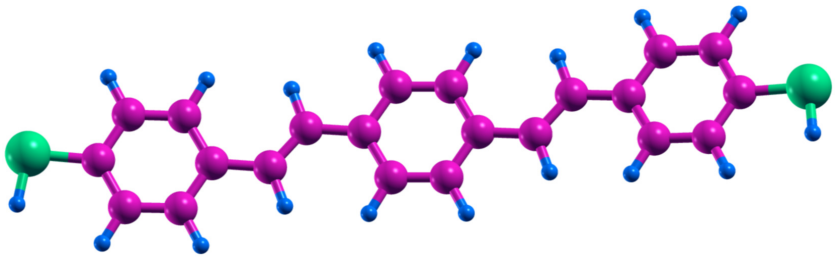

(b) trans–trans isomer

Figure 3.2: Schematic diagram of the two isomers of opv3 studied: (a) cis-trans and (b) trans-trans. Color code: blue=H, green=S, and purple=C.

changes as compared to the hollow site are small (Fig. 3.3). We therefore consider subsequently only the hollow site.

3.3 Linear Response Transport Properties

We start our analysis of the transport properties of this class of molecules by presenting, in Fig. 3.4, the zero-bias $T(E)$ as a function of energy, for the two opv3 isomers and their derivatives. These have been obtained both at the LDA level and by including the SIC. In general, we find a reduction of the transmission coefficient at the Fermi level, $T(E_F)$, and hence of the linear response conductance, with protonation regardless of the isomer and the calculation method (see Table 3.1 for details). This already demonstrates that protonation degrades the transport properties of thiol-bonded phenylenevinylene oligomeres and does not improve them as suggested originally [34].

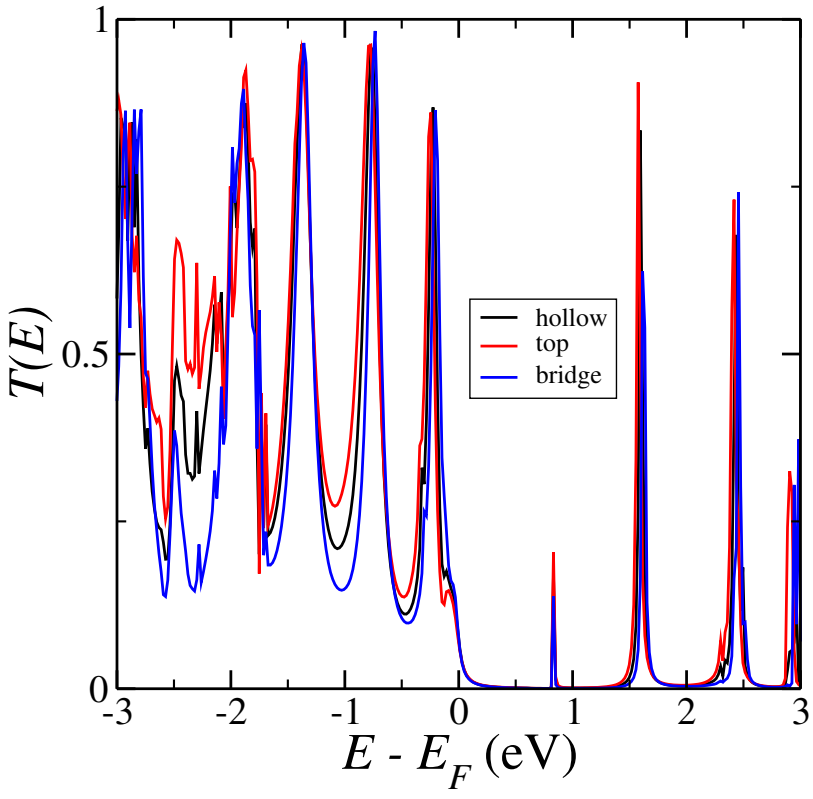

Figure 3.3: Transmission coefficient for hollow (energetically most favorable), bridge, and top site contact geometries of opv32H on Au(111).

When the calculations are conducted at the LDA level for all the molecules the transmission at the Fermi level is through the tail of a peak located just below E_F. The peak is downshifted upon the application of the SIC, which returns us a tunneling situation with no transmission peaks in the immediate vicinity of E_F. The magnitude of the SIC-induced shift of the transmission peak, however, depends on the protonation state of the molecule, being $\sim$0.5 eV for opv3, $\sim$1 eV for opv3H and $\sim$2 eV for opv32H. Such different shifts are expected from the SIC and will be explained later.

Let us now take a closer look at the effects of the protonation by using first the LDA results. When the molecule is attached to the Au surface with thiol groups only (opv3) the transmission coefficient directly below E_F is formed by a broad feature

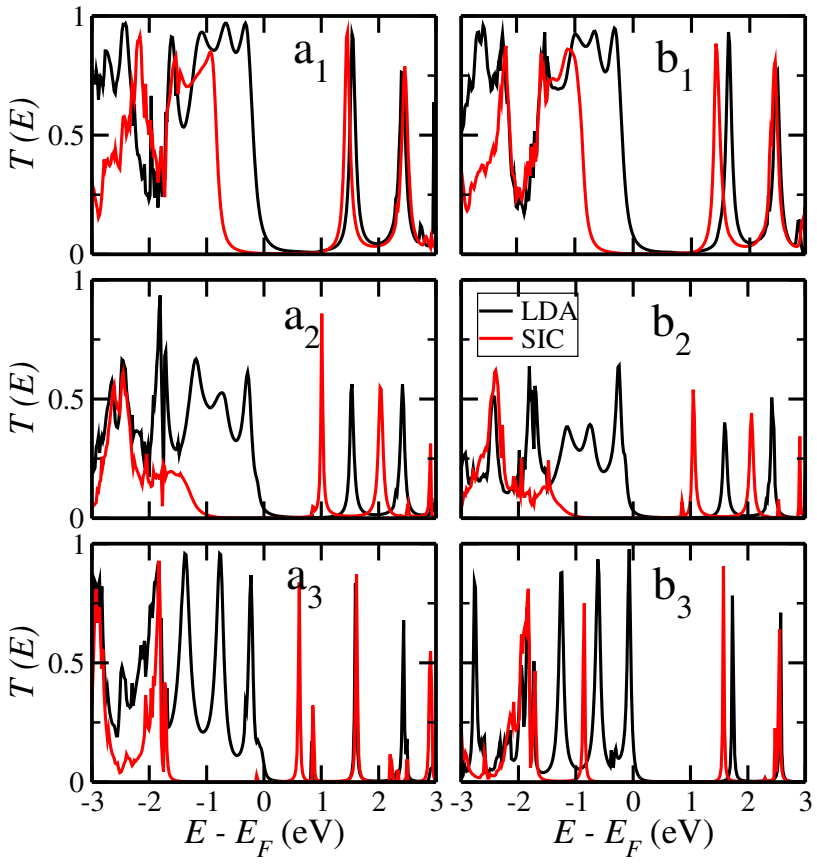

Figure 3.4: Zero-bias transmission coefficients $T(E)$ for the two isomers of the oligophenylenevinylene derivatives. Here a_1, a_2, and a_3 refer to the trans-trans isomers of opv3, opv3H, and opv32H, respectively, while b_1, b_2, and b_3 refer to their corresponding cis-trans isomers.

approximately 1.8 eV wide and with an average transmission of $T \sim 1$. The feature is composed of four distinct peaks, which overlap completely. A first protonation (opv3H) has the effect of reducing the average transmission to about 0.7 and to separate both the highest and the lowest peak of the four-peak structure. The separation occurs because of a general reduction of the peak width and not because of an energy shift. The second protonation (opv32H) continues this trend and now one can clearly observe four separated peaks. This essentially suggests that the main effect of the protonation is a weakening of the electronic coupling between the molecule and the electrodes, a feature which is consistent with the increased Au-S bond length upon

protonation.

In general, when the SIC is applied to the LDA Kohn-Sham electronic spectrum the occupied states are downshifted in energy to improve both the HOMO-LUMO gap [134] and the level alignment between the molecule and the electrodes [14, 128, 135]. The corrections scale with the occupation of the given state, so that one expects a larger downshift for states with weaker hybridization to the electrodes. For this reason in the SIC results the first transmission peak is further away from E_F for opv32H and for opv3H than for opv3. As a consequence, the relative conductance reduction upon protonation is more significant for the SIC then for the LDA. A second interesting feature of the SIC results is that there is essentially no difference between the zero-bias conductance of opv3H and opv32H, i.e., the molecule is sensitive only to the first protonation, while a subsequent one has little effect. Note that such insensitivity is perfectly met for the case of the trans-trans isomer, while the conductance drops by a further factor two for the cis-trans isomer. Note that the factor two is likely to be washed out in an experimental situation by fluctuations in either the molecule geometry, the binding structure with the electrodes, or the solvent[139]. When applying the SIC, however, the unoccupied levels remain in every situation approximately 0.7 eV away from E_F. While for the LDA the conductance

Table 3.1: Linear response (zero-bias) conductance of all the molecules investigated as calculated with LDA (G_{LDA}) and SIC (G_{SIC}).

Molecule	G_{LDA} ($\mathrm{M}\Omega^{-1}$)	G_{SIC} ($\mathrm{M}\Omega^{-1}$)
opv3 trans-trans	7.82	0.27
opv3H trans-trans	3.71	0.06
opv32H trans-trans	5.27	0.06
opv3 cis-trans	6.82	0.19
opv3H cis-trans	2.63	0.04
opv32H cis-trans	1.73	0.02

around E_F is always dominated by the HOMO level, this downshift results in an additional LUMO contribution for some of the configurations.

Spurious Peak in the Transmission Coefficient

Note that there is a peak in the transmission around E_F for some of the structures, which is especially notable if the transmission is plotted on a logarithmic scale (Fig. 3.5). This peak is due to a suface state of the Au(111) surface and is not a molecular state. The nature of the state is discussed in Ref. [135], where it is shown that the state is highly dispersive in the surface Brillouin zone, which implies for a given k_x-k_y-point that the state is visible in the partial density of states and transmission as a sharp resonance, at a different energy for every k_x-k_y-point. Importantly, in the mentioned reference it is also shown that a sharp resonance contributes to the transmission significantly only for perfectly symmetric junctions. In fact, as a potential is applied (i.e., introduction of asymmetry) the peak height is reduced and eventually becomes neglible. This can be seen in the bias dependent transmission for opv32H around E_F (Fig. 3.6). The reduction of the peak height is also reflected by a decrease of the differential conductance with increasing but small bias. For larger applied bias, and more generally for asymmetric junctions, therefore the transmission through the Au surface state does not contribute significantly to the conductance.

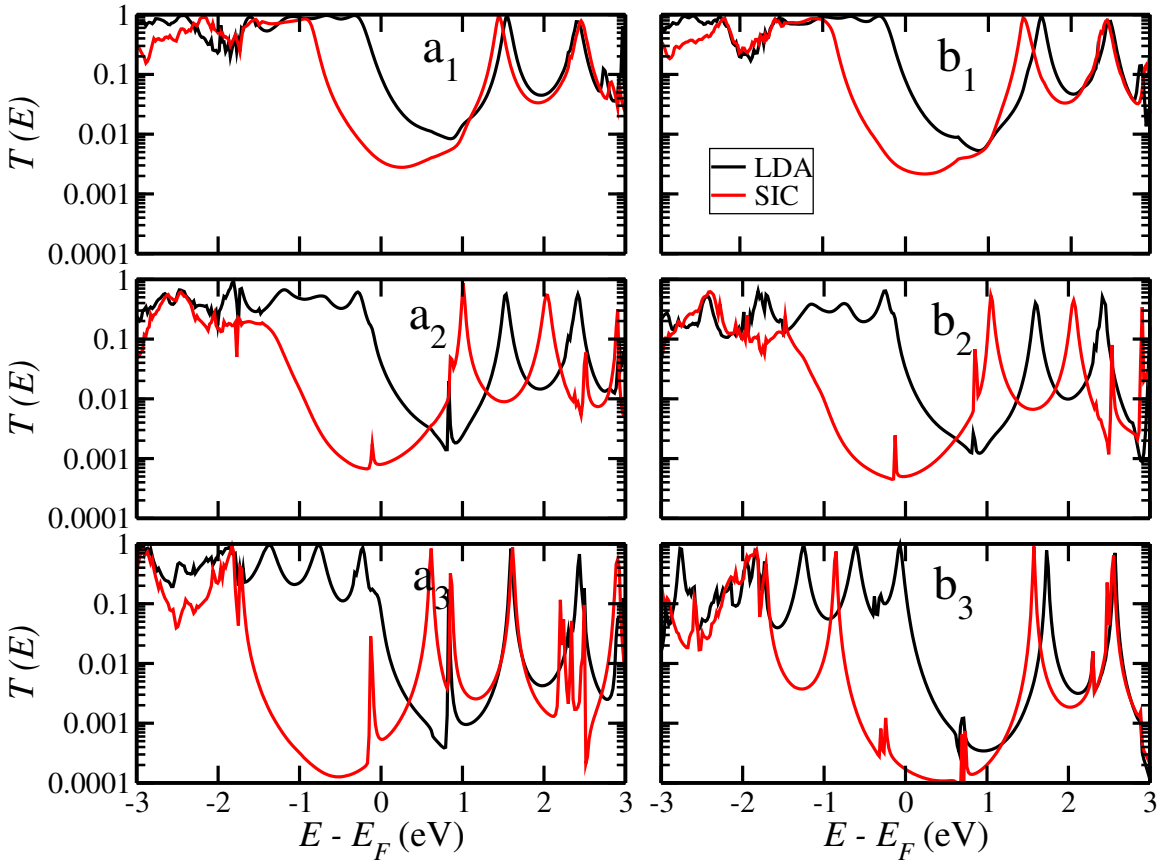

Figure 3.5: Same data as shown in Fig. 4, with the transmission plotted on a logarithmic scale.

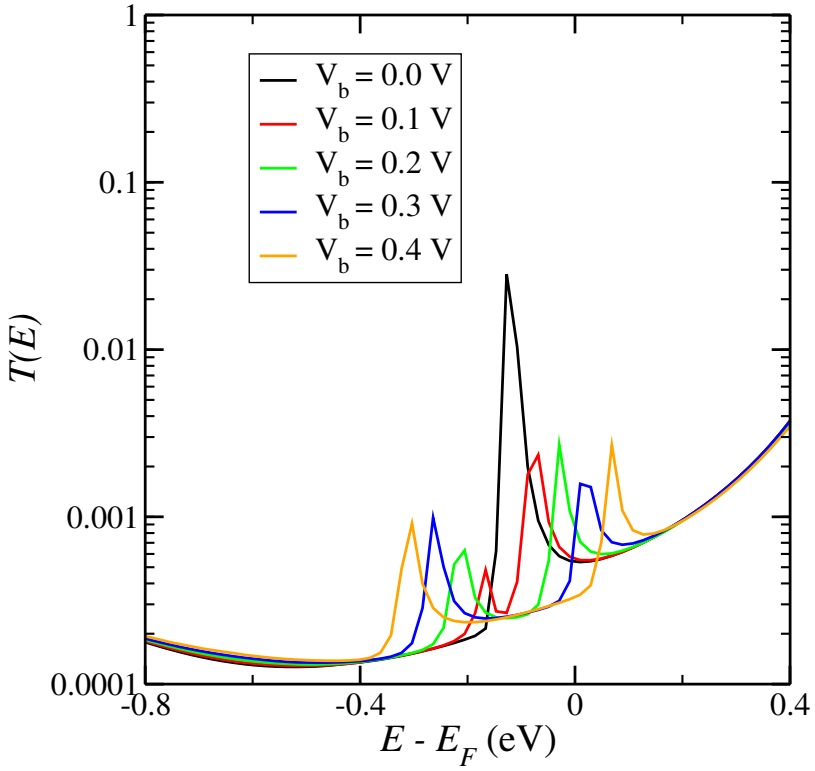

Figure 3.6: Evidence that the spurious peak of Fig. 4(a_3) does not contribute to the transmission.

Finally, we mention that in the SIC calculations for opv3H and opv32H also the LUMO levels experience a significant energy downshift. This is a spurious effect originating from the atomic approximation to the SIC used in this work, since in principle one should not expect any corrections for the unoccupied orbitals. In general, the spurious energy downshift of the LUMO may result in an artificial contribution of the LUMO to the conductance. This however is not the case here, since the unoccupied levels remain in every situation at least 0.7 eV away from E_F. As a consequence, the main result of the conductance reduction with protonation remains valid.

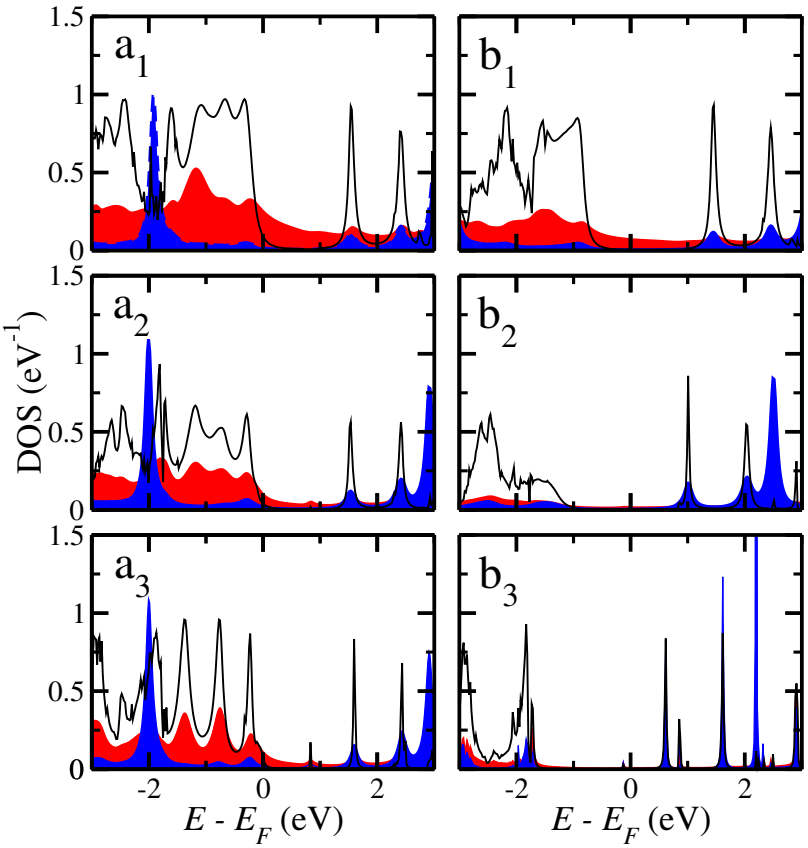

Figure 3.7: DOS projected on the C (blue shadowed area) and S (red shadowed area) atoms closest to the electrodes. For a better understanding the transmission coefficient at zero-bias is also plotted as thin black line. Panels a_1, a_2, and a_3, respectively, refer to opv3, opv3H, and opv32H calculated using the LDA. Panels b_1, b_2, and b_3 are corresponding results calculated using the SIC.

A better understanding of the transport properties in the different protonation configurations can be achieved by looking at the densities of state (DOS) of the molecules incorporated in the junctions. In Fig. 3.7 we report the DOS projected on the S and C atoms closer to the Au surface. This is presented only for the trans-trans isomer for both LDA and SIC. Note that very similar findings are obtained for the trans-cis configuration (not reported here). In Fig. 3.7 we also re-plot $T(E)$ so that a direct correspondence between the transmission and DOS can be established. The figure shows a clear correlation between the DOS of the most external S and C atoms and the transmission. In particular, we note that for the opv3 molecule the S DOS shows a broadly distributed feature corresponding to the energy region where the four-fold transmission structure appears. The feature then fragments in separated peaks, following the behavior of the transmission coefficient and indicating a reduction in the electronic coupling between the molecule and the electrodes. Additional information can be extracted from the plot of the first two occupied molecular orbitals responsible for the transport, presented in Fig. 3.8. The figure shows the transmission eigenchannels[85] originating from the left electrode. It can be seen that as opv3 is protonated the π conjugation connecting the two electrodes across the molecule is lost in favor of a situation with amplitude on the phenylenevinylene units but little on the linking groups to the electrodes.

The figure suggests that, as opv3 is protonated, the π conjugation connecting the two electrodes across the molecule is lost in favor of a situation where there is amplitude on the phenylenevinylene units but little on the linking groups to the electrodes. This confirms once again the reduction of the electronic coupling between the molecule and the electrodes upon protonation. The coupling strength is evident from the full width at half maximum and the height of the transmission peak. Indeed, adding two H atoms to the opv3 gives significantly different results as compared to

the addition of one H atom. For opv3H a large asymmetry is introduced by the single H atom: The peaks are still broad but the height is only about 0.5, which indicates that the coupling on the unprotonated side is preserved, while on the protonated side it is significantly reduced. When adding the H atom on both sides the coupling is everywhere weak, which is reflected by much sharper transmission and DOS peaks. The fact that the height of the transmission peaks is approximately 1 also indicates similar coupling strengths on both sides. Note that we only sample one possible surface of Au, namely the (111) surface. Moreover, we consider a perfectly flat surface, while the actual surface in the experiment can be subject to significant disorder. However, we expect the main result, that protonation leads to a reduced conductance as compared to the unprotonated molecule, to be robust for the different surface morphologies.

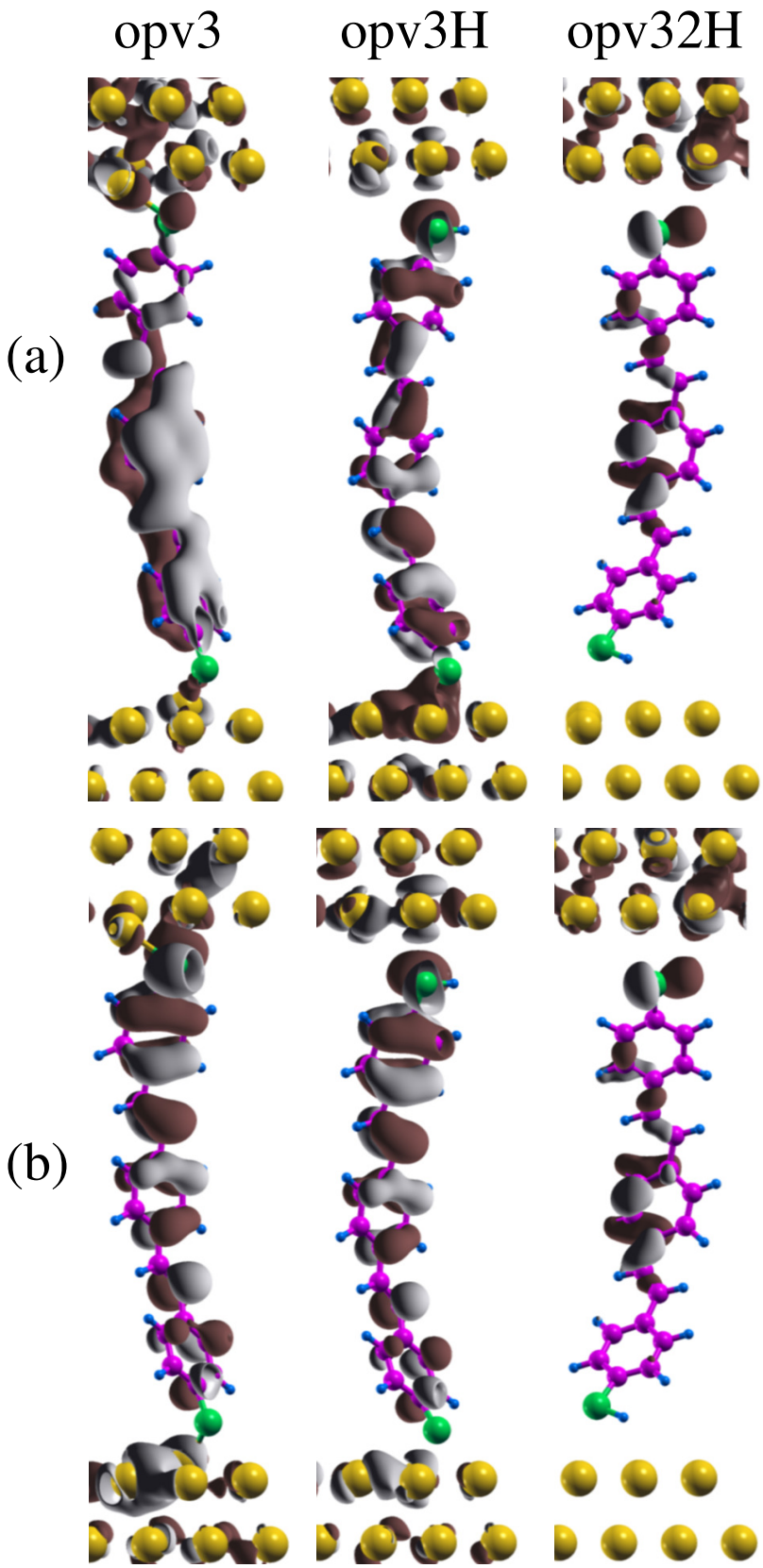

Figure 3.8: LDA isosurfaces of the transmission eigenchannels, showing that the first two occupied molecular orbitals contribute to the transmission. Panel (a) is for the HOMO−1 level and (b) for the HOMO level.

Table 3.2: Comparison between the experimental IP, EA, and HOMO-LUMO gap (IP−EA) of opv3, calculated either as total LDA energy differences, ΔSCF-LDA, or from the SIC Kohn-Sham eigenvalues. We report results for the SIC screening parameter, α, being either 0 (corresponding to pure LDA), 1/2 or 1.

	IP (eV)	EA (eV)	GAP (eV)
ΔSCF-LDA	5.7	2.7	3.0
SIC ($\alpha = 0$)	3.7	1.8	1.9
SIC ($\alpha = 1/2$)	3.9	1.8	2.1
SIC ($\alpha = 1$)	4.3	1.9	2.4
Experiment [140]	5.1	2.4	2.7

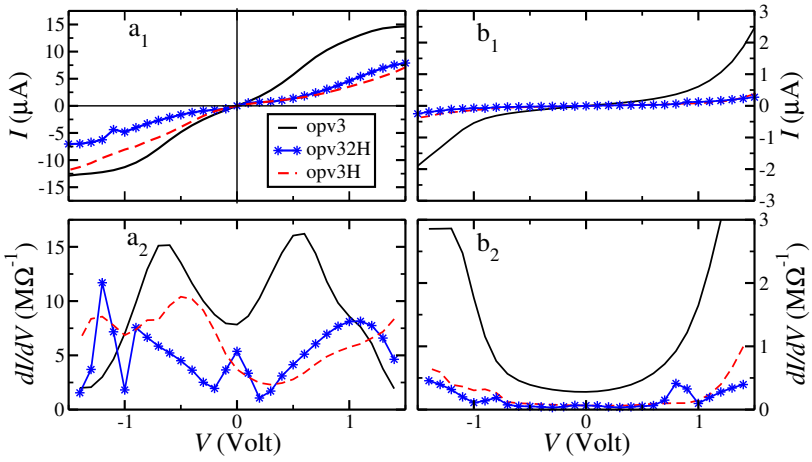

Figure 3.9: Current and differential conductance (calculated numerically) for the oligophenylenevinylene derivatives as a function of the bias voltage. The left panels, a_1 and a_2, refer to the LDA and the right panels, b_1 and b_2, to the SIC.

To conclude the section we comment on the appropriateness of using the SIC scheme for this transport calculation. In Table 3.2 we report the experimental values for the ionization potential (IP) and the electron affinity (EA) of opv3, together with those calculated from LDA total energy differences between neutral and charged molecules (ΔSCF-LDA), and from the Kohn-Sham eigenvalues. In the latter case we have performed calculations for the SIC screening parameter, α, being either 1 or 1/2. In general, we find that the SIC quasi-particle band structure reproduces relatively well the HOMO-LUMO gap and the absolute position of the HOMO level.

In particular, when $\alpha = 1$, the value used for the transport calculations, the SIC quasi-particle spectrum underestimates the experimental HOMO-LUMO gap by 0.3 eV and the IP by 0.8 eV. Since the molecule HOMO can be interpreted in DFT as the negative of the IP, one may conclude that even the SIC HOMO is 0.8 eV higher than the experimental one. This however describes the molecule in vacuum. When the molecule is attached to metallic electrodes two main effects need to be considered. On the one hand, charge re-distribution re-aligns the molecule energy levels with respect to the Fermi energy of the electrodes, so that usually the HOMO for the molecule in contact to the electrodes is higher than that in vacuum. On the other hand, image charge effects, not described at the level of local exchange and correlation functionals, reduce the HOMO-LUMO gap of the molecule[141]. The net result is that usually the Kohn-Sham quasi-particle spectrum calculated with SIC for the molecule attached to the electrodes offers a good description of the system[118, 128, 135, 142]. Given the fact that in this case the HOMO of the molecule, when calculated with SIC, is at least 1 eV below E_F, we can safely conclude that the transport is going to be always tunneling-like, regardless of the particular molecule.

3.4 Finite Bias Transport Properties

We now turn our attention to the finite bias transport properties of opv3 under different protonation conditions. In Fig. 3.9 we report the current-voltage characteristics, I-V, for all the opv3 derivatives, calculated with both the LDA and SIC. The first and most notable feature is that there is a significant reduction of both the current and the conductance upon the first opv3 protonation, while the second protonation produces only a minor effect. The finite bias calculation thus confirms the linear response calculation that protonation reduces the transmission of the molecule. How-

ever, in addition it adds the information that the reduction affects the rather large bias window approximately from +1 Volt to −1 Volt.

Going into more detail and starting from the LDA results (left panels), we observe that, although the current for opv3 is always larger than that for both opv3H and opv32H, this is not true for the conductance at biases $|V| > 1$ Volt. In fact, when the external voltage reaches that magnitude there is a decreasing differential conductance for all the derivatives, where this feature is sensibly more pronounced for opv3. As a consequence, the conductance for opv3 becomes smaller than for the two protonated derivatives, although the total current remains larger for the unprotonated case. Interestingly, the voltage at which the molecules present a decreasing differential conductance is rather close to the voltage at which the devices burn down in experiment[143]. These fine details, however, onset on top of rather smooth I-V curves, which do not show any drastic change of slope or particularly significant gap.

Moving to the SIC IV curves, the most notable difference with respect to the LDA results is a drastic reduction of the current over the entire bias window. This indeed is not surprising and simply reflects both the larger HOMO-LUMO gap calculated with the SIC and the downshift in energy of the HOMO, which was discussed previously. The SIC IV curves are smooth. However, now they show a clear activated region, i.e., a sudden change in slope as the bias exceeds a critical value. In particular, we observe the onset of a rather large current just before $|V| \sim 1$ Volt, with the increase being significantly more pronounced for opv3 than for opv3H and opv32H. As a consequence, the differential conductance is flat up to $|V| \sim 0.75$ Volt and then increases rapidly. In the case of the SIC there is no decreasing differential conductance over the bias window investigated so that the conductance of opv3 remains always larger than for the other two derivatives. Finally, we point out that, by large, the I-V characteristics are always symmetric with respect of the bias polarity, regardless of the exchange

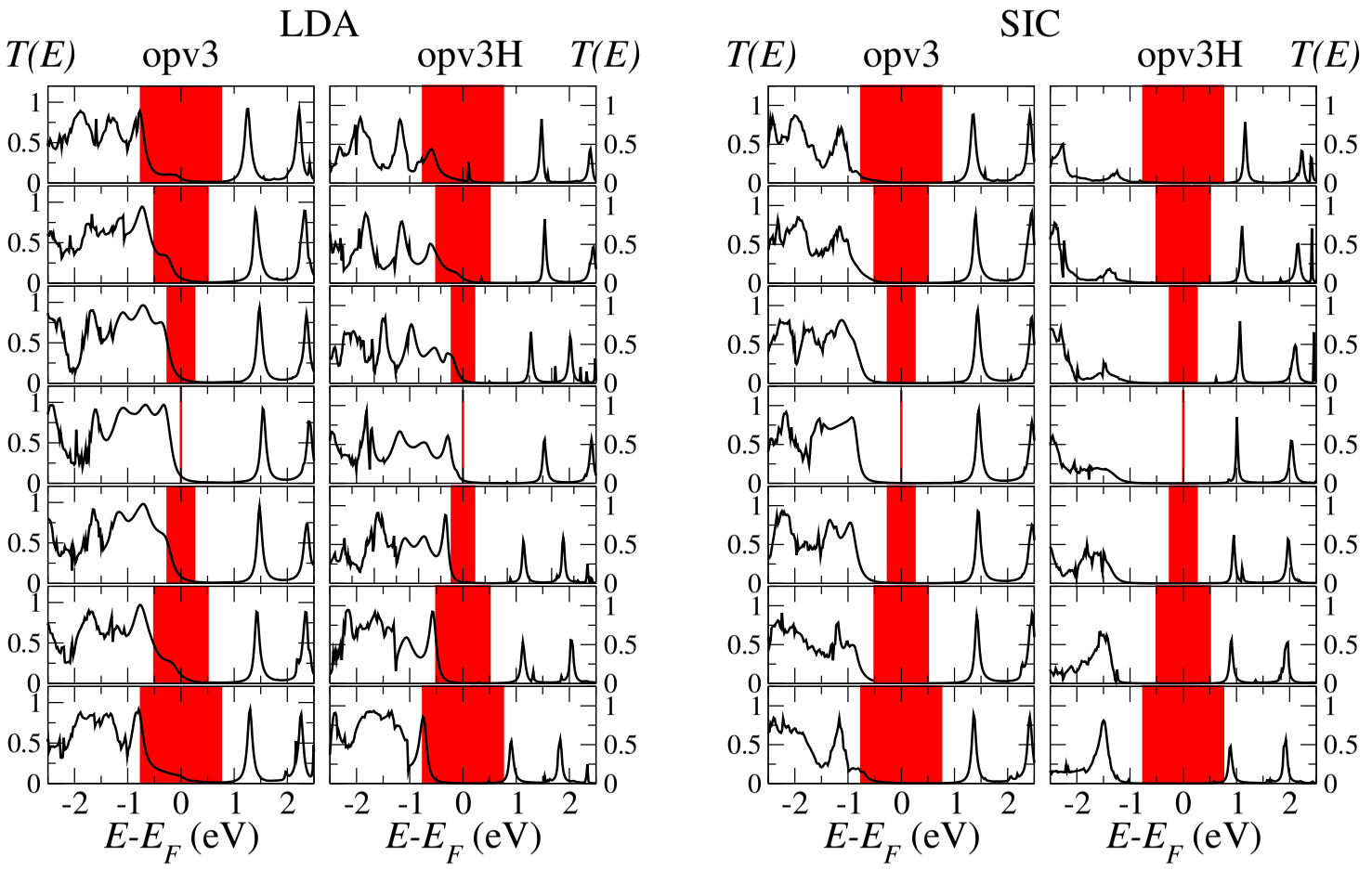

Figure 3.10: Transmission coefficient as a function of energy, $T(E;V)$, for different bias voltages. We show results for opv3 and opv3H as obtained with the LDA (left) and SIC (right). Panels from top to bottom correspond to the following bias voltages (in Volt): -1.5, -1.0, -0.5, 0, 0.5, 1.0, 1.5. The red boxes mark the bias window. The integral of $T(E;V)$ over the bias window determines the current at that particular voltage.

and correlation functional used. The only exception is encountered for opv3H, which shows a notable asymmetry. This is due to the fact that the molecule is bounded to the electrodes with two different anchoring groups at the two sides, i.e., the junction does not have inversion symmetry.

Recalling that the current is nothing but the integral over energy of $T(E;V)$, a more detailed understanding of the various I-V curves can be obtained by looking at the bias dependent transmission coefficients displayed in Fig. 3.10 for the LDA and SIC. In the figure we report $T(E;V)$ for opv3 and opv3H and for the following voltages (in Volts): -1.5, -1.0, -0.5, 0, 0.5, 1.0, 1.5. We do not present data for opv32H, since they are relatively similar to those of opv3H.

Let us start the analysis by looking at opv3 as calculated by the LDA (left hand side of Fig. 3.10). As reported before, when $V = 0$ the Fermi level of the electrodes cuts through the tail of the first peak in the HOMO multiplet and the conductance is relatively large. Upon a moderate bias increase ($|V| = 0.5$ Volt, regardless of the bias polarity) there is a rearrangement of the HOMO multiplet in such a way that no transmission peak enters the bias window. This means that the molecular energy level associated to the first conduction peak in the HOMO multiplet shifts downwards in energy following the lower of the two chemical potentials. In doing so the molecule avoids charging [144] and the conductance remains dominated by the tail of the first transmission peak, the only part of $T(E)$ having spectral weight within the bias window. As the bias further increases the highest energy HOMO peak enters the bias window (for instance this is clearly visible at -1.0 Volt). However, in doing so the peak height decreases with the net effect of reducing the conductance, see Fig. 3.9(a_2), while the current keeps increasing, see Fig. 3.9(a_1). This indicates the the electronic coupling between the associated molecular level and the electrodes has changed under bias. The dynamical re-arrangement of the electronic coupling in

a closely spaced multiplet of atomic orbitals is the mechanism for the decreasing differential conductance and it is rooted in the re-hybridization of the molecular orbital under bias [144].

The case of opv3H is by large similar to that of opv3. The molecular level associated to the first conduction peak in the HOMO multiplet again shifts downwards in energy following the lower of the two chemical potentials. This leads to a slow increase in the current as the larger bias window is counter-balanced by a loss in spectral weight within the window itself. This time, however, the details of $T(E;V)$ depend on the bias polarity, reflecting the asymmetry of the molecule. In fact, while for $V > 0$ the first peak in the HOMO multiplet shifts almost rigidly as the bias increases, for $V < 0$ the shift is accompanied by a significant distortion in the $T(E)$ profile. This is seen clearly at -1.5 Volt, where we find that essentially the two peaks have merged and are located almost entirely within the bias window, explaining why the current at negative bias voltage is slightly larger than at positive bias.

Finally we study the same $T(E;V)$ but now calculated using the SIC, see the right hand side of Fig. 3.10. Here the situation is much simpler, since the HOMO-LUMO gap is significantly larger than for the LDA and, at all voltages investigated, the chemical potentials of the electrodes remain far from any molecular level. This means that no state enters the bias window and little level re-normalization under bias is induced. As such the I-V curves remain rather featureless, since they are dominated by simple enlargement of the bias window over a rather flat $T(E;V)$. The minor asymmetry in the Current Voltage characteristics (I-V) curves is due to small differences in the binding geometry of the molecule to the left and right electrodes. Still some effects due to the asymmetry remain for the case of opv3, for which we can observe a systematic reduction of the amplitude of the first conductance peak as the bias window sweeps from positive to negative.

3.5 Summary

We have studied the switching behavior of opv3 and its single and double protonated derivatives, opv3H and opv32H. Our results show that the opv3 conducts approximately an order of magnitude more efficiently than its protonated variants. This contradicts the interpretation previously given, in which it was the protonated form to present larger conductance [34]. Our results are demonstrated robust against the choice of exchange and correlation functions and are consistent regardless on whether the calculation is done with LDA or SIC. Also important is the fact that the same result obtained for the linear response conductance is carried on to finite bias calculations, so that the opv3 form is more conductive over a $\sim$3 eV bias range. Moreover, the difference between the experimental [34] ON/OFF ratio is significantly lower than what we find under protonation. This is further evidence that the switching mechanism is not a protonation reaction. We can only speculate about the actual mechanism at this stage, e.g., reversible rearrangements of the bonding geometries of the thiol groups.

Chapter 4

Current-Induced Changes of Migration Energy Barriers in Carbon-Based Systems

In nanoscale electronic devices current-induced forces can be advantageous but they also can be a problem. On the one hand they can lead to device destruction, and on the other hand they can be used as key part of the device operation, for example in resistive switching memories [91, 145–147]. One prominent consequence of current-induced forces is electromigration, which is a momentum and energy transfer process from the flowing electrons to the ions, leading to atomic rearrangements and diffusion [100]. An important contribution to these forces is determined by the charge density redistribution caused by the electron flow [39, 101, 148]. The interaction between the current and the ions can also give rise to local heating [38, 149–152], which involves inelastic transitions among states of different energy.

C-based compounds, in particular graphene and carbon nanotubes (CNTs), are an important class of emerging materials for nanoscale devices [153–156]. In literature one can find multiple examples of current-induced ionic dynamics in such systems.

For instance, it has been shown that controlled doping of a CNT-based p-n junction can deteriorate under the application of an intense current over a long time [157] indicating atomic re-arrangement, and phenomena like etching [158] or clustering due to electromigration have been observed in both graphene and CNTs. These all indicate current-driven mass transport in C-based systems and the examples are many [159–161]. Other works [158, 162–165] have shown migration of metals and molecules on CNTs. Au moves driven by a current on the surface of graphene [163] and of other metals [158], while scanning transmission electron microscopy has demonstrated that vacancies and adatoms can migrate on the surface of CNTs due to the current flow [166].

The relative stability of two atomic structures is determined by the barrier for transforming one structure into the other. The energy needed for such process can be provided by temperature, whose distribution in a nanostructure can be highly non-homogeneously due to current-induced heating. For a given local temperature, atoms migration can be triggered by a reduction of the energy barriers along particular paths, and such reduction can be induced by a current. Migration barriers in nanomaterials are usually evaluated with the nudged elastic band (NEB) method, which determines the minimum energy path between two metastable configurations [167–169]. In this work we evaluate the possibility that a current, in addition to locally heating the device, can also reduce the energy barriers. In particular, we determine the changes in barrier heights for the motion of C adatoms on graphene and CNTs, and evaluate the possibility of annealing Stone-Wales (SW) defects in graphene. Current leading to directional motion of C adatoms could also be used to anneal vacancies. We demonstrate that the effect of current-induced forces on the migration barrier heights is qualitatively different in graphene and CNTs.

4.1 Computational Details

We use a set of systematic first principles simulations to understand the effect of current-induced forces in C-based systems. Our tool is the SMEAGOL code [76, 77, 170], which calculates the charge density, the transmission coefficient and the current across a two-probe device using the non-equilibrium Green's function formalism. The one-particle potential is provided by the SIESTA implementation of density functional theory [129, 171]. The current, I, is calculated using the Landauer formula in Eqn. (2.35). In general, the force acting on the i-th atom, $\mathbf{F}_i$, at the position $\mathbf{R}_i$ is given by a Hellmann-Feynmann equation, which can be expressed by the Euler-Lagrange equation of motion for classical ions as [100, 172]

$$\mathbf{F}_i = -\int \frac{\partial \nu}{\partial \mathbf{R}_i} \rho(\mathbf{r}) d\mathbf{r} \,, \tag{4.1}$$

where ν is the potential. Note that we consider quasi-static atomic motion (the velocity is close to zero), so that additional forces depending on the velocity are neglected [173, 174].

Under an applied voltage the forces are evaluated in SMEAGOL as detailed in Ref. [148]. Since for current-carrying open systems the forces can be non-conservative [18, 39], we obtain the NEB energy barrier heights for atomic motion by evaluating the work, U, done on an atom along the migration path [175]

$$U = -\sum_i \int \mathbf{F}_i \cdot d\mathbf{R}_i \,. \tag{4.2}$$

The total work is given by the sum over all the atoms. Within the NEB method a series of intermediate structures, so called beads, is constructed. These connect the structural configurations of the initial and final states. While moving between

adjacent images an additional spring force is added to ensure continuity of the path, thereby mimicking an elastic band [176]. A series of iterations is carried out to converge the images on the lowest potential energy path between the initial and the final structure.

We use a 5×8 graphene supercell containing 160 atoms to evaluate the energy barrier for the removal of a SW defect, a 3×11 supercell (132 atoms) for investigating the motion of adatoms, and a (5,5) metallic CNT (440 atoms). In all cases the cell size is above the critical value required to avoid any length dependence of the transport, and convergence has been monitored by performing a subset of calculations in which the system length was repeatedly doubled. Graphene is oriented with the y-axis perpendicular to its plane and the transport direction is along z. We use 10 k-points to sample the reciprocal space in the study of the SW defect in armchair-oriented graphene, while 5 k-points are used for the migration of adatoms on zigzag-oriented graphene. The exchange and correlation functional is treated at the level of local density approximation and we consider a double-ζ polarized basis set, a real space grid cutoff of 400 Ry, and an electronic temperature of 25 meV. During structural relaxation the forces are converged below 0.01 eV/Å.

4.2 Annealing the Stone-Wales Defect in Graphene using Current

The conventional way of removing defects in graphene is through annealing [177] or plasma treatment [178]. Here we start by investigating the possibility of removing SW defects with current-induced forces. The SW defect is formed when four C hexagons are transformed into two pentagons and two heptagons by rotating one of the C-C

bonds by 90° with respect to the mid-point of the bond [see left inset of Fig. 4.1(a)]. We find an energy barrier for converting SW-defective into pristine graphene of the order of 4 eV [see Fig. 4.1(a)], in agreement with previous theoretical results [179]. This rather large energy barrier ensures that both structures are stable.

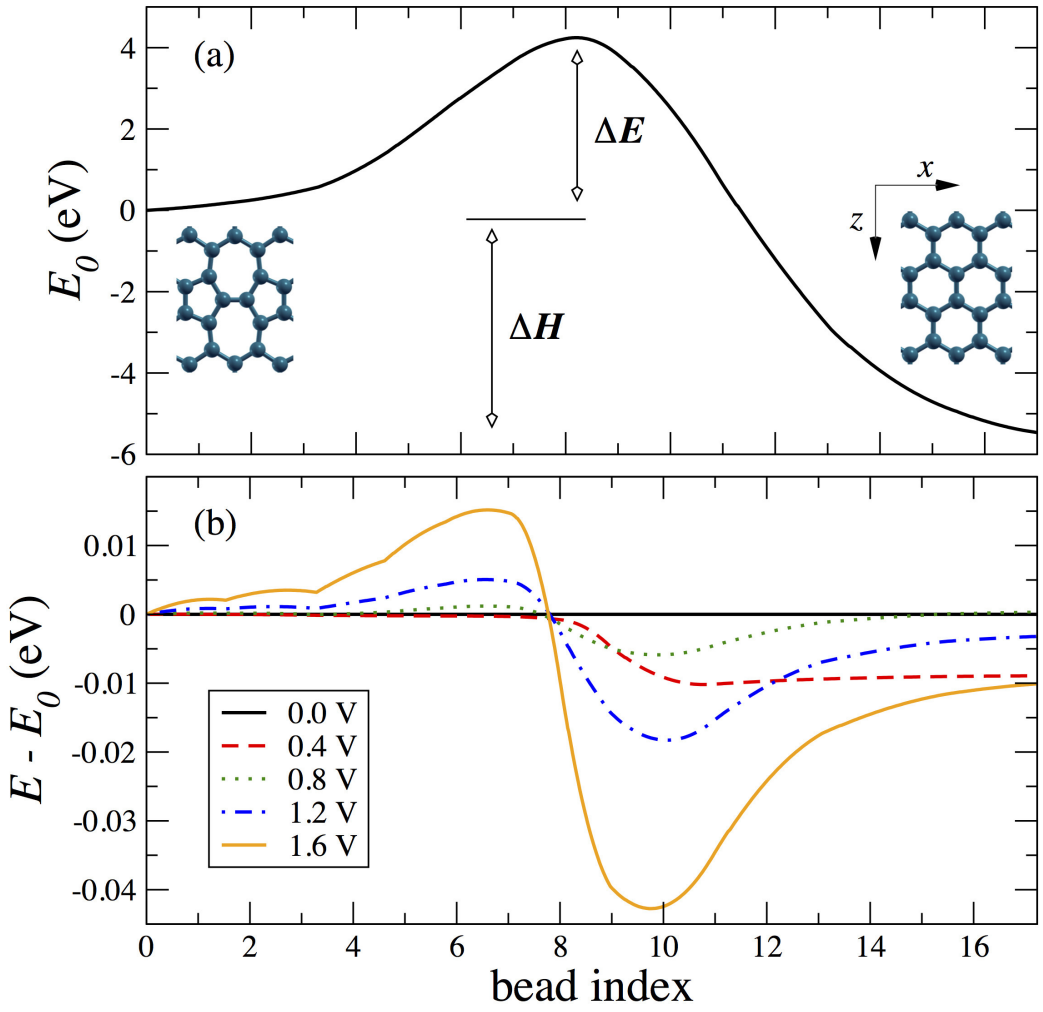

Figure 4.1: (a) Work as function of the path coordinate (bead) for a transition from a SW defect to pristine graphene. The energy barrier height is denoted by ΔE and the enthalpy of formation of pristine graphene by ΔH. (b) Difference between the work done at an applied bias and that at zero bias.

When a bias voltage causes current to flow, the barrier height changes, as shown in Fig. 4.1(b). The overall change, however, is small, < 0.05 eV even for a current density of $\sim 3.25 \times 10^4$ A/m corresponding to a bias of 1.6 V. An analysis of the

current-induced forces shows that the small change is because the forces themselves are small along the reaction path. We have evaluated whether the introduction of asymmetry in the system can increase the effect, by iso-electronically replacing the two moving C atoms with a B-N pair [180]. However, also for such asymmetric SW defect no significant current-induced barrier change is found. We thus conclude that current alone cannot anneal out SW defects.

4.3 Motion of Adatom on Graphene and CNT

A second important defect often found in graphene and CNTs is the C adatom, which can potentially move with an applied current pulse. Here we consider the migration of a C adatom on graphene, when this is oriented with the zigzag edge extending along the transport direction (z-axis) [see Fig. 4.2(a)]. After structure optimization the bridge site is found to be the most energetically favorable position for the C adatom. The adatom is located 1.87 Åabove the graphene plane and has equal bond distances of 1.53 Å to the two nearest C atoms. An identical bonding structure is found for the (5,5) metallic CNT with the bond distance now at 1.51 Å [see Fig. 4.2(b)]. These results are in good agreement with Ref. [181]. Note that the CNT has two non-equivalent bridge sites, indicated as A and C in Fig. 4.2(a), where site B is equivalent to site A. Site C has the lowest energy [181].

During the migration along the z-axis the adatom can move directly from site A to site B (path A1) or via a two-step process through site C (paths A2 and A3). Fig. 4.2(c) shows the work profile for path A1 at equilibrium for both graphene (solid curve) and the CNT (dashed curve). The barrier height in graphene is calculated at 0.6 eV, in good agreement with previously published results [179]. Note that the paths A1, A2 and A3 are all equivalent in graphene when no voltage is applied. In

contrast, for the CNT paths A1 and A2 are not equivalent even at equilibrium, while paths A2 and A3 are. For the CNT path A1 has a barrier height of 0.37 eV, which is somewhat smaller than that of graphene, while path A2 (dash-dotted curve) has a significantly larger barrier, 1.39 eV.

Fig. 4.3(a) shows the work profile for the A1 path in the CNT at different V_b. We find a notable reduction of the barrier height together with an increasingly more negative total work as the bias gets larger. Note that such reduction is directional, namely the barrier decreases when the adatom moves against the current flow (from A to B), while it increases when it moves in the opposite direction along the current flow (from B to A). Such result is consistent with the experimentally observed current induced electromigration. Fig. 4.3(d) shows that the current through the system is significant and it varies little as the adatom migrates along the path. It reduces when the adatom moves from A to B until it reaches the mid-point and thereafter increases again.

Next, in Figs. 4.4(a) and 4.4(b) we compare the bias-induced barrier height changes for graphene and the CNT. While for graphene the changes are smaller than 0.1 eV over the considered bias range, they are as large as 0.5 eV for the CNT. The energy barrier for path A1, the lowest energy path for the CNT, is reduced by about a factor two when a bias of 1.6 V is applied. This will lead to a significantly enhanced migration rate.

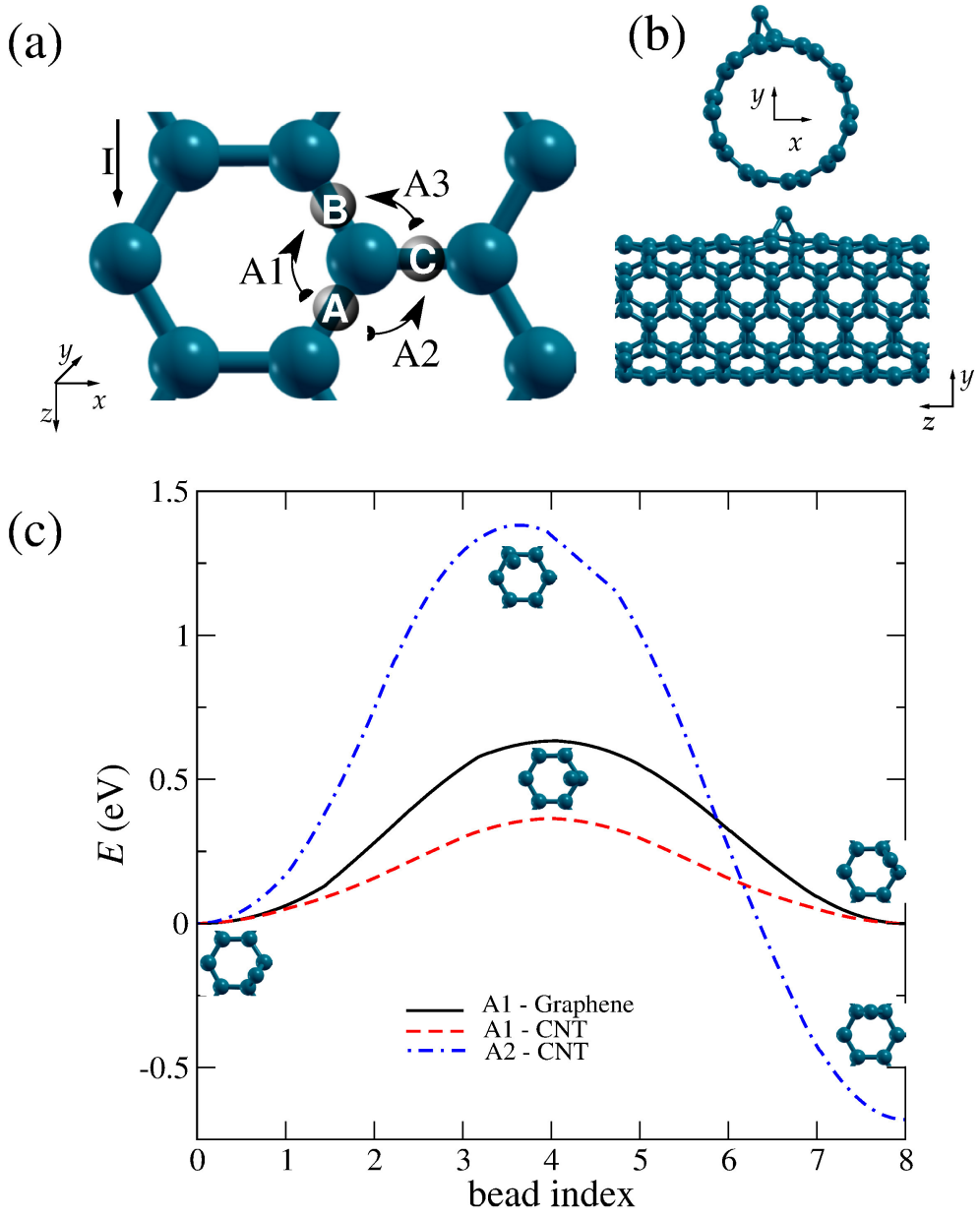

Figure 4.2: (a) Schematic path considered in the NEB calculations of an adatom migration on graphene and CNT. A, B, and C represent the metastable positions of the carbon adatom, and A1, A2, and A3 are the paths taken by the adatom in the direction shown. (b) Structure of the adatom on the CNT. (c) NEB profiles for the migration of the C adatom through path A1 on graphene and through paths A1 and A2 on the CNT.

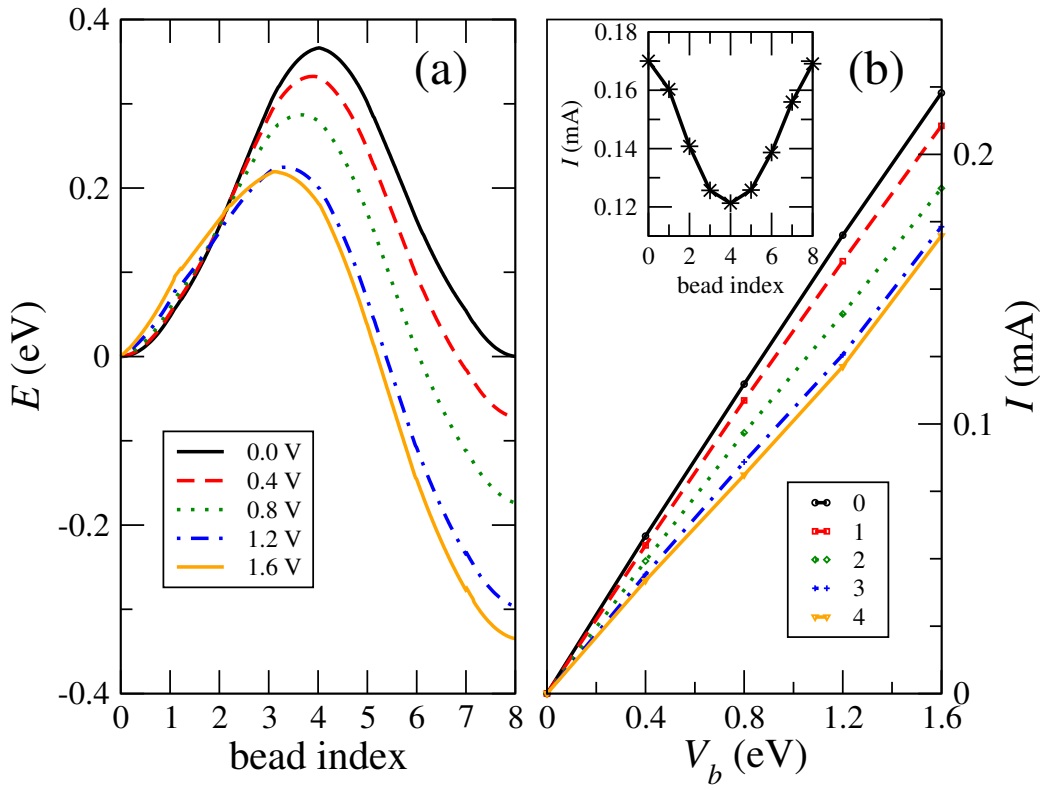

Figure 4.3: (a) NEB profiles under bias for the migration of the C adatom on a (5,5) CNT through path A1. (b) Current versus voltage curves for the first four beads of path A1. The insert is the current at 1.2 eV.

In order to understand the different behavior of graphene and the CNT in Fig. 4.5 we plot the current induced forces at 1.6 V along the migration path, which is mainly along the z direction. The order of magnitude of the current-induced forces is similar for the two systems, however the component parallel to the migration path is small for graphene. Moreover, in graphene the z component of the current-induced forces changes sign along the path, leading to a cancellation of the total work done. In contrast for the CNT the z component is large and has the same sign along all the path, leading to a significant net work.

It is important to note that the electric field plays only a minor role in the reduction of the barrier height. This can be verified by evaluating the current-induced forces for a scattering region of double length (79.8 Å) kept at the same bias, i.e. sustaining

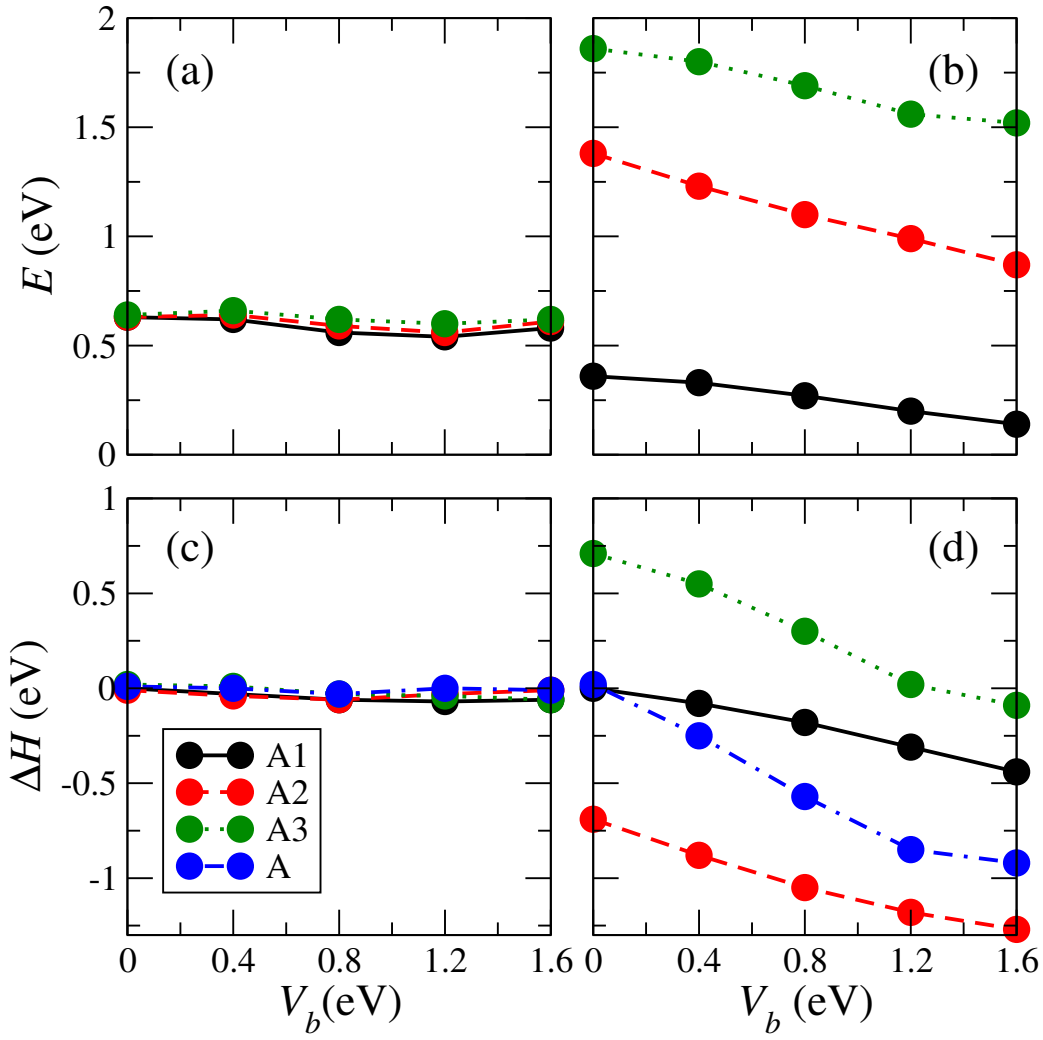

Figure 4.4: Barrier height, W, for the migration of a C adatom on (a) graphene and (b) the CNT. Enthalpy of migration, ΔH, of a C adatom on (c) graphene and (d) the CNT [A=A2+A3−A1].

an electric field twice as small. We found that the current across the two systems is approximately the same and so are the current-induced forces (see Fig. 4.6). This confirms that the forces are predominantly current- and not field-induced.

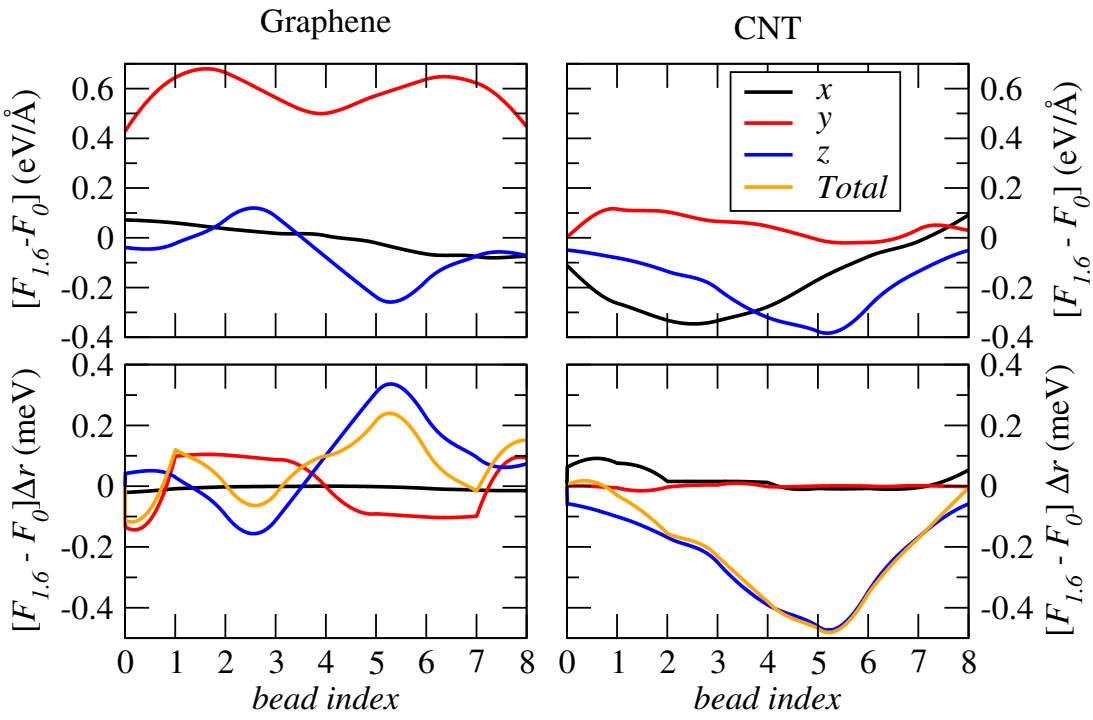

Figure 4.5: Current induced forces, $\Delta\mathbf{F} = \mathbf{F}_{1.6\mathrm{V}} - \mathbf{F}_{0\mathrm{V}}$, for graphene and the CNT along the migration path A1, and their components along the migration path $\Delta F_\mathrm{s} = \Delta\mathbf{F} \cdot \Delta\mathbf{R}/|\Delta\mathbf{R}|$ [see Eq. (4.2)], where $\Delta\mathbf{R}$ is the displacement vector of the adatom from one bead to the next. ΔF_s is rather small and changes sign along the path for graphene, leading to a vanishing overall current induced work, while it is large and has the same sign over all the path for the CNT.

4.4 Effect of Current-induced Forces on CNT Chiralities.

Furthermore, we note that the findings are generally valid for CNTs of different chirality by comparing results for three different types of metallic CNTs (see Fig. 4.7). We considered metallic CNTs with different chiralities, namely (6,3) and (7,4). The direction of the path is different for the different chiralities, so that also the 0 bias energy profile is different. For the path used for the (6,3) chirality the 0 bias barrier height is 0.39 eV and, and for the (7,4) chirality it is 0.14 eV. For the (6,3) and (7,4) chiralities we find that the barrier height is reduced by about 0.35 and 0.18

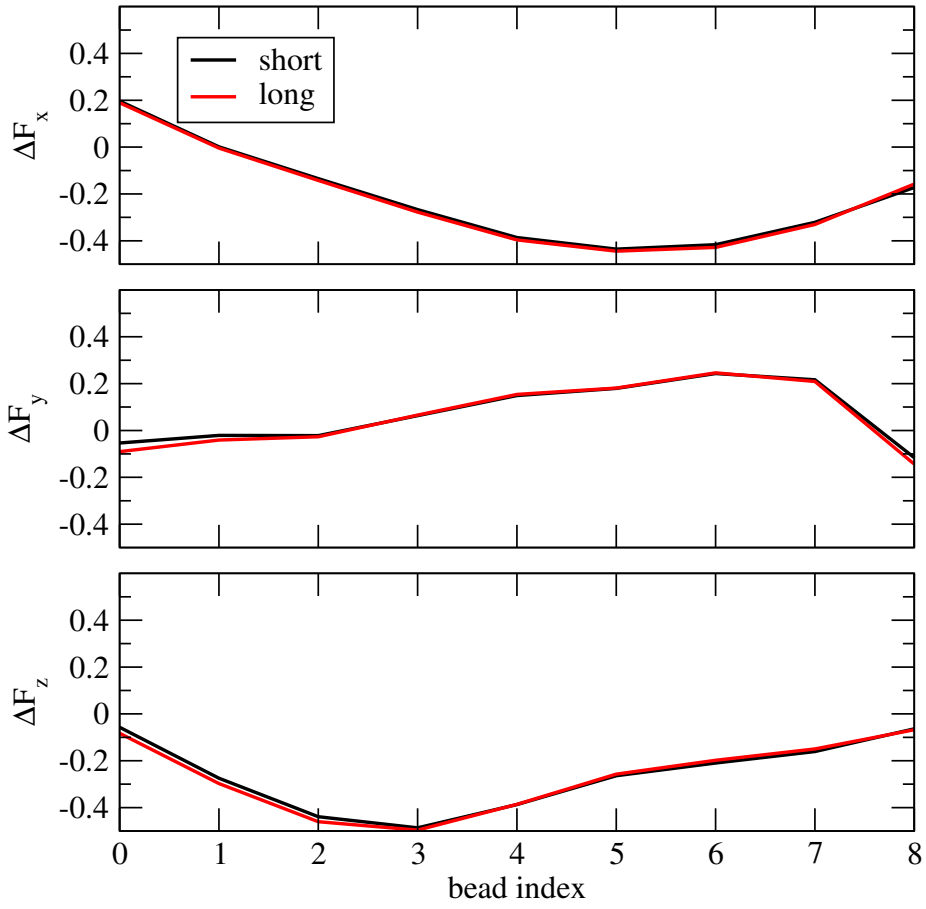

Figure 4.6: Current-induce forces on the adatom on CNT at 1.6 V for the two different lengths of the scattering region (39.90 Å ("short") and 79.81 Å ("long")), as function of the bead index.

eV, respectively, at 1.6 V. These results show that qualitatively the current induced energy barrier suppression is analogous for all considered CNTs, and differ only on a quantitative level, which shows that our results are generally valid for different types of CNTs.

4.5 Total Work Done on the Migrating Adatom

A second important quantity besides the barrier height is the total work done by the system to move the adatom from the initial to the final point along a given path. If this work is negative, additional kinetic energy is provided to the migrating adatom.

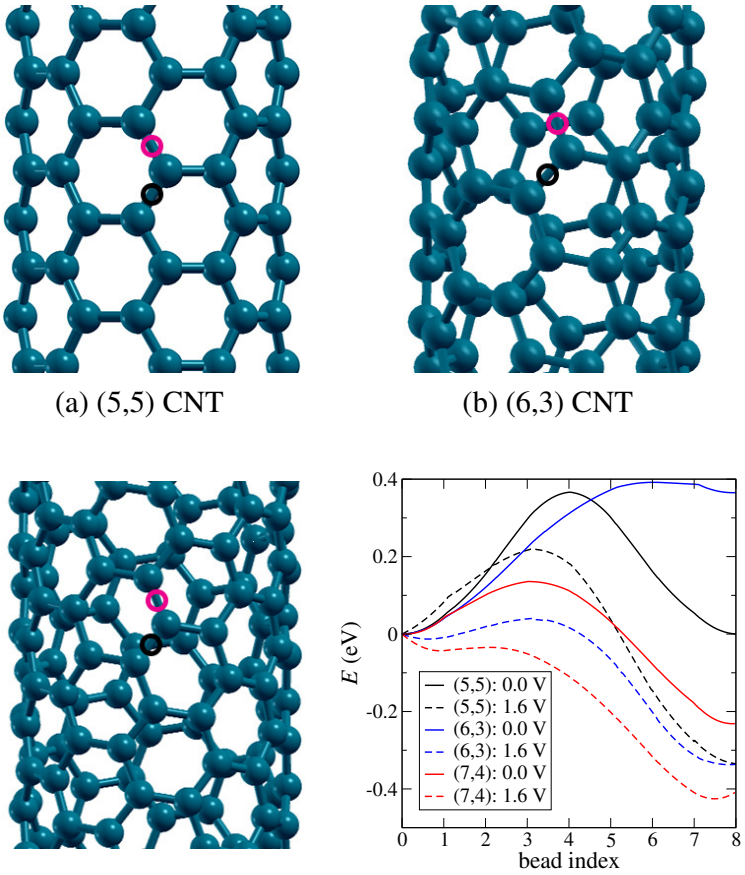

Figure 4.7: Energy barriers at 0 and 1.6 V, for a (5,5), a (6,3), and a (7,4) CNT. The reduction of the barrier is qualitatively similar for the (5,5), (6,3), and (7,4) CNT. The migration path is from A to B (against the flow of current). Solid lines represent the 0.0 V and dashed line for the 1.6 V barrier heights. The end-point atomic structures of the migration paths are indicated for the three considered chiralities, where the pink circle corresponds to the bead with index 0, and the black circle represents the bead with index 8.

For graphene we obtain zero work at equilibrium by symmetry, and even under bias this remains vanishingly small [Fig. 4.4(c)]. For the CNT at equilibrium the work along path A1 is zero, since sites A and B are equivalent, while for paths A2 and A3 we obtain opposite signs and a magnitude of 0.7 eV, which is equal to the energy difference between a C atom adsorbed on sites A and C [Fig. 4.4(d)]. When a bias is applied, for all paths the work is negative, and of the order of -1 eV, indicating a strongly exothermic evolution.

Importantly, our results allow us to address the question on whether the current-induced forces acting on the adatom are conservative. We consider the work along the closed path A [dash-dotted curves in Figs. 4.4(c) and (d)], where we first follow paths A2 and A3 and then A1 in the reversed direction. For conservative forces the total work along the path has to be zero. At zero bias this is indeed the case for both systems, showing that in absence of a current the force field is conservative. For graphene, even under bias, the work along the closed path A remains close to zero, whereas for the CNT it is significant and increases in magnitude with the bias until it reaches the value of -1 eV at 1.6 V. This indicates that for an adatom migrating on a CNT the force field is highly non-conservative. In the SI we provide a qualitative explanation for the general origin of the non-conservativeness of current-induced forces.

4.6 Origins of the Current Induced Forces

Here we give a short intuitive description for the origins of the current induced forces in DFT-NEGF simulations, of their non-conservativeness, and of the involved approximations.

In general, when current flows through a system and gets scattered at an obstacle, there will usually be an accumulation of electrons on the side of the obstacle closer to the electrode with the higher chemical potential, and a depletion of electrons on the opposite side. In a classical picture the positive nucleus of such an obstacle (adatom in our case) will then be attracted to the side with the negative charge (where electrons accumulate), which results in a net current induced force, and which in this case points against the current flow. More generally the finite bias leads to depopulation of some of the states in the junction, and increased population of other states. Such a change

of orbital populations leads to a general change of the forces, which can point in any direction, and will depend on the system. All these combined effects lead to forces in x, y, and z direction, and are the origin of the phenomenon of electromigration.

We show that for a realistic system of a C adatom moving on a CNT such forces are not conservative. In an intuitive picture, the non-conservativeness of the forces arises since the current densities in the system are not homogeneous. If for example an adatom moves against the current flow along bonds with high current density, and assuming that the current flow is along positive z, while the current induced forces point towards $-z$, then it will typically gain a large amount of energy by the current induced force. We can then move the atom along a path perpendicular to the current flow to a part of the system with a smaller current density. We then move it back to its original z coordinate along this path with low current density, and where typically the current induced forces are reduced. The energy loss will then be smaller then the energy gain we obtained when moving the atom towards smaller z. Note that even if the forces have x and y components, the work involved in the motion of the adatom perpendicular to the current flow cancels over a closed path, if we consider a structure that is periodic along z. Following a closed path we can therefore obtain a non-zero net work, which means that the forces are non-conservative. We demonstrate this in Fig. 5 of the main manuscript, where moving the adatom against the current flow along one path (A1), and back on another path (A2$\rightarrow$A3), a net work is done on the adatom.

We summarize by pointing out the restrictions of the used DFT-NEGF method. The main approximation is that we assume that the motion of the atoms is always quasi-static. This corresponds to neglecting the momentum transfer from the flowing electrons to the nuclei, and considering only the forces arising from the changes in electrostatic and chemical bonding energies. This implies that we do not consider

current-induced heating effects, which would lead to vibrations (motion) of the atoms around the lowest energy path.

4.7 Summary

In summary, we have demonstrated that first principles calculations can be used to quantitatively evaluate the change in energy barriers for an atomic migration process. We find that the results strongly depend on the system, not being a ubiquitous consequence of the current. The barrier height for annealing of SW defects is found to be insensitive to the current, as it is that for C adatoms migration on graphene. We have shown that this effect is due to the fact that the force component along the migration path almost vanishes, despite the total force is large. The situation is very different for adatoms migration of on CNTs, where the current reduces the energy barrier of up to a factor two. We have also demonstrated that the adatoms gain significant energy as they migrate along the current-driven path. Finally, we have addressed the fundamental question of whether the current-induced forces are non-conservative. This was previously shown to be the case in model systems and here it is demonstrated within density functional theory. Indeed the motion of the adatom along a closed path results in a substantial work, demonstrating the non-conservativeness of the current-induced forces.

Chapter 5

Quantum Transport through Tunable Molecular Diodes

Organic electronics is expected to play a key role in future semiconductor industry, as it costs less to process an organic than an inorganic semiconductor [109]. In addition, promising intrinsic device functionalities such as the rectification in molecular junctions are offered [6, 104, 182]. However, despite recent advances, the rectification (diode) behavior of single molecule junctions is not well understood [44, 183]. Being determined by the ability of the system to support current differently in two directions, molecular diodes were early analyzed by Aviram and Ratner [45]. They exploit the energy gap between the highest occupied molecular orbital (HOMO) of the donor and the lowest unoccupied molecular orbital (LUMO) of the acceptor. Various similar concepts later have been predicted theoretically and demonstrated experimentally [35, 184–186]. In a single molecule rectifier typically a donor-acceptor molecule is placed between gold electrodes using a thiol group as linker because of its high flexibility under stress [187]. For example, such contacts can be achieved by mechanical break-junction techniques [34, 188].

Recent experiments have addressed the charge transport through symmetric tetra-

phenyl and non-symmetric dipyrimidinyl-diphenyl molecular diodes [184]. A pronounced rectification has been observed for the non-symmetric molecule, with larger current in the direction from dipyrimidinyl (acceptor) to diphenyl (donor), but not for the symmetric molecule, suggesting that the properties of the junction can be tuned by chemical substitution that breaks the symmetry. However, the effect of the composition has not been investigated systematically. We thus study the rectification behavior of a series of non-symmetric molecular diodes consisting of pyrimidinyl and phenyl rings, covalently bound to two electrodes. We identify the conditions that yield an optimal performance of the junction and derive general rules for designing molecular diodes.

5.1 Computational Details

We employ the SIESTA [130] implementation of density functional theory, which uses an atomic orbital basis set. For C, N, S, and Au a double-zeta polarized basis is used with a 30 meV global energy shift [129]. All core electrons are described by normconserving pseudopotentials of Troullier-Martins type [131], including scalar relativistic corrections [132]. A cutoff energy of 600 Ry is used and the local density approximation (LDA), as parameterized by Ceperley and Alder [133], is employed for the exchange-correlation functional. Since the LDA underestimates the electron localization, we also apply the atomic self-interaction correction (ASIC). Generally, the ASIC corrects the occupied states by downshifting them in energy and improves the level alignment between molecule and electrode as well as the HOMO-LUMO gap [35]. The parameter controlling the amount of ASIC added to the LDA is set to $\alpha = 0.7$, as this value gives reliable results for molecular systems [134, 189].

All structures are geometrically optimized with a force threshold of 0.02 eV/Å.

Using the optimized geometries, we perform quantum electron transport calculations in the non-equilibrium Green's function framework as implemented in the SMEAGOL package [76], which builds up on SIESTA and for which we use the same convergence criteria as for the electronic structure calculations. In the transport calculations the complex part of the integral yielding the charge density is computed using 16 energy points on the complex semi-circle, 16 points along the real axis, and 16 poles. For finite bias the integral over the real energies is evaluated for at least 500 points. An electronic temperature of 300 K is used in all calculations.

5.2 Structural and Compositional Analysis

Figure 5.1 shows representative molecular setups with varying donor-acceptor compositions: pyrimidinyl-triphenyl, dipyrimidinyl-diphenyl, and tripyrimidinyl-phenyl. Referring to the number of involved N atoms (two in every pyrimidinyl ring) these cases will be called 2N, 4N, and 6N, respectively. Thiol groups are used to bind the molecules to the Au(111) electrodes. We find that the most favorable binding site is the Au(111) hollow site, due to *sp* hybridization, which is in agreement with previous ab-initio calculations [136]. Moreover, we note that the planar structures of the molecules do not develop significant distortions in the geometry optimizations. Figure 5.2 provides isosurfaces of the HOMO and LUMO of the isolated dipyrimidinyl-diphenyl molecule. The HOMO is localized in the acceptor region, see Fig. 5.2(middle), whereas the LUMO is centered at the first pyrimidinyl after the acceptor-donor contact and extends over the whole molecule, see Fig. 5.2(bottom).

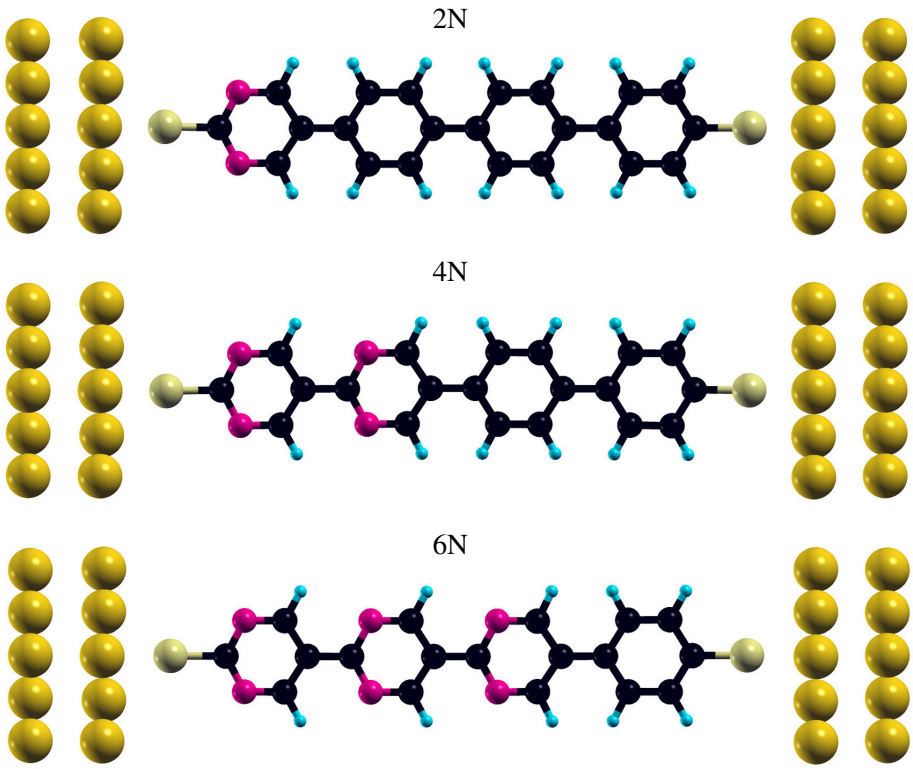

Figure 5.1: Structures of the pyrimidinyl-triphenyl (2N), dipyrimidinyl-diphenyl (4N), and tripyrimidinyl-phenyl (6N) transport configurations. Blue, black, purple, yellow, and gold color denotes H, C, N, S, and Au atoms, respectively. The molecules are terminated by thiol groups. Only the first two atomic layers of the Au electrodes are shown.

5.3 Linear Response Regime

We first study the transport properties of the 2N, 4N, and 6N systems by analyzing the zero-bias transmission coefficients as function of the energy in Fig. 5.3. Results are obtained at the LDA and ASIC levels. In both cases, the first transmission peak below the Fermi energy is significantly reduced when the number of pyrimidinyl rings increases (and therefore the number of phenyl rings decreases), whereas all other peaks show only minor modifications. This observation can be explained by the fact that the amount of charge transfer from the donor to the acceptor region is reduced. For the LDA there is a tiny transmission at the Fermi energy through the tails of the HOMO peaks, whereas the ASIC shifts those to lower energy, as expected, so that the

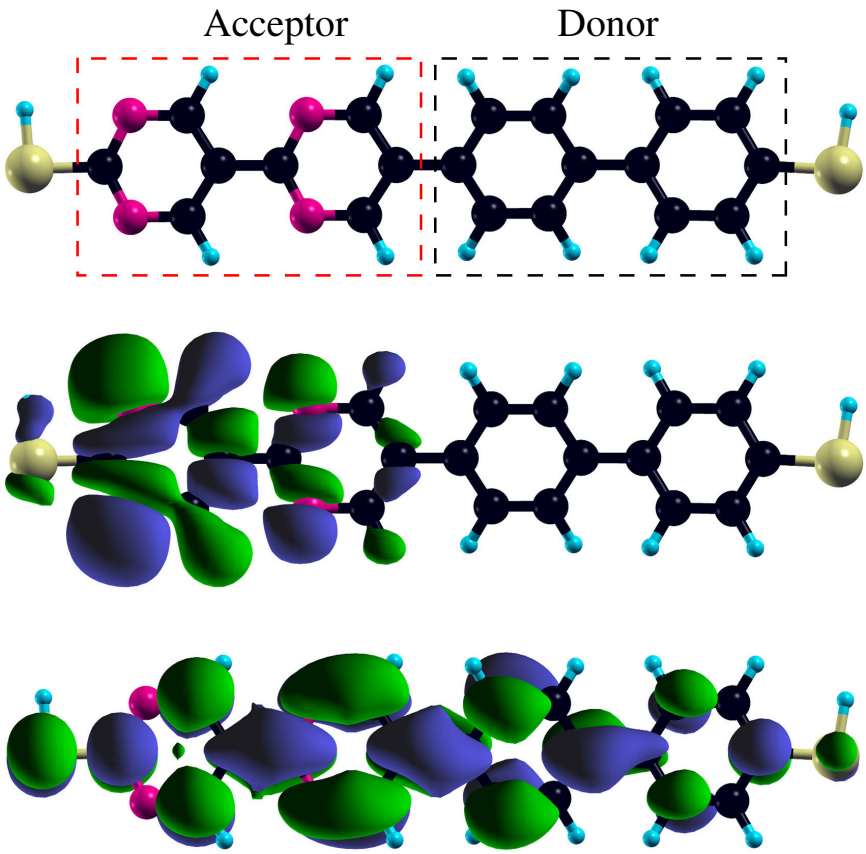

Figure 5.2: Dipyrimidinyl-diphenyl diode with acceptor and donor regions (top), HOMO (middle), and LUMO (bottom).

transport is purely due to tunneling. All other transmission features, in particular the LUMO peak, are hardly modified upon application of the ASIC.

Figure 5.4 presents N densities of states obtained at the LDA and ASIC levels, showing no major difference besides the HOMO-LUMO gap, which is improved by the ASIC from 2.30 eV to 2.56 eV. We will later show that the I-V characteristics obtained from the ASIC indeed agrees well with experiment [184]. The fact that the difference between the ionization potential and electron affinity of the molecule in gas phase (4.43 eV) is higher shows that the alignment of the molecular levels is substantially affected by the presence of the electrodes. Both the HOMO and HOMO-1 are dominated by N states, since pyrimidinyl acts as acceptor. When the size of the pyrimidinyl region

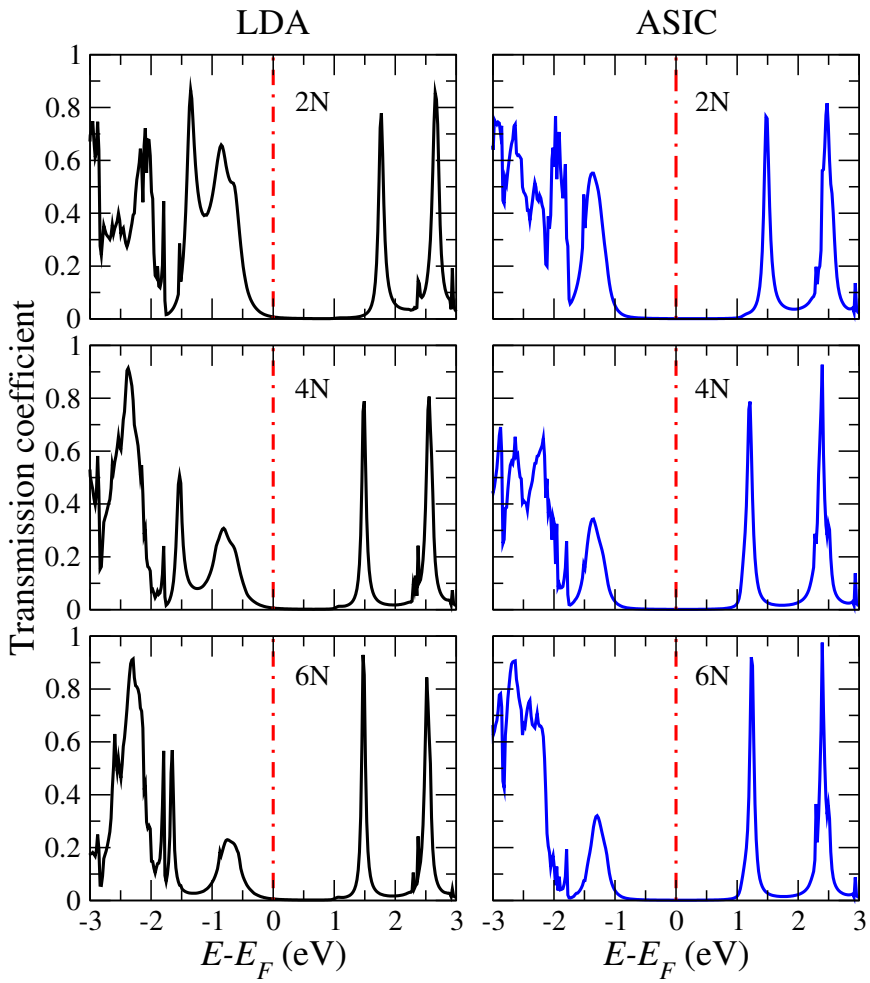

Figure 5.3: Zero-bias transmission coefficients of the 2N (top), 4N (middle), and 6N (bottom) configurations. The left panels present LDA results and the right panels ASIC results.

varies from 2N to 6N the splits into different peaks since the N atoms in different distances to the electrode experience different chemical environments. Since they are key for the transport, Fig. 5.5 shows for the HOMO−1, HOMO, and LUMO orbitals the corresponding transmission wave functions (transmission from left to right), for the 4N system as an example. We observe in each case that the transmission relies mainly on the π-orbitals. For the HOMO−1 (top) the transmission wavefunction is localized on the phenyl region and for the HOMO (middle) on both ends of the molecule. On the other hand, for the LUMO it is centered on the first pyrimidinyl

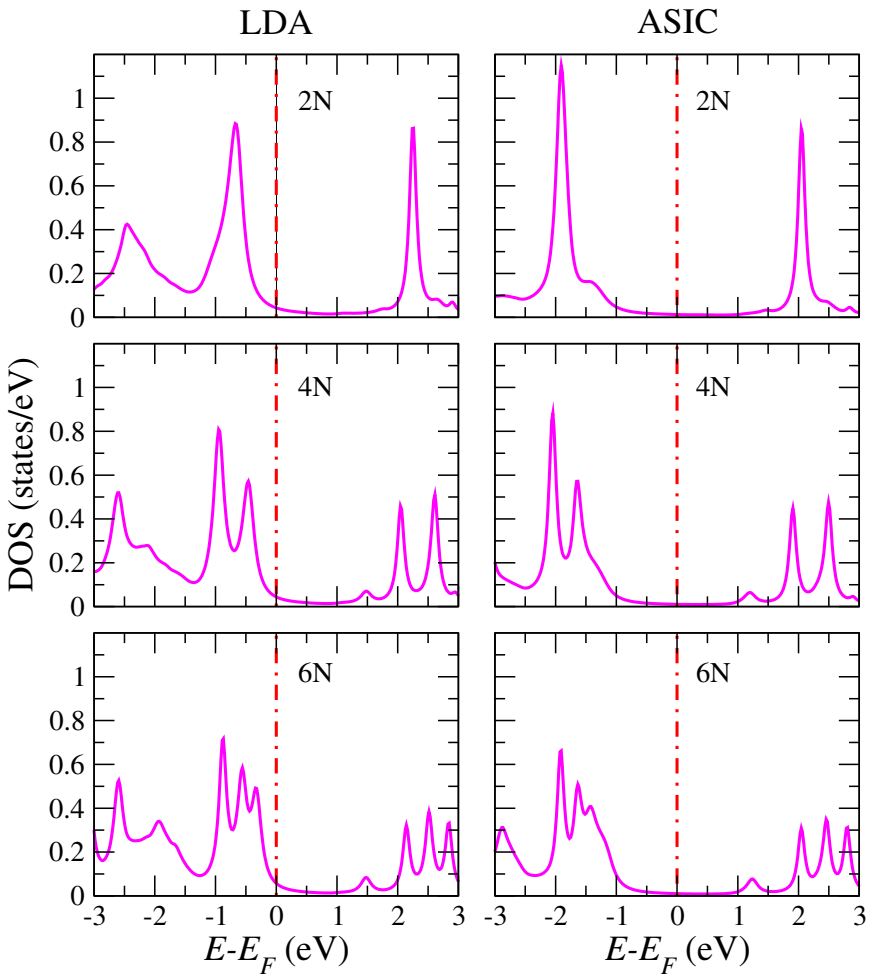

Figure 5.4: Densities of states of 2N (top), 4N (middle) and 6N (bottom). The left panels present LDA results and the right panels ASIC results.

ring after the acceptor-donor contact, thus resembling the shape of the LUMO itself, compare Fig. 5.2(bottom).

5.4 Finite Bias Regime

We now turn to finite bias transport. Both for the LDA and ASIC we observe an asymmetry between positive and negative bias in the I-V characteristics, similar for all three systems, see Fig. 5.6. On the other hand, the negative differential conductance around -1 V appears only for the LDA, because for the ASIC no transmission

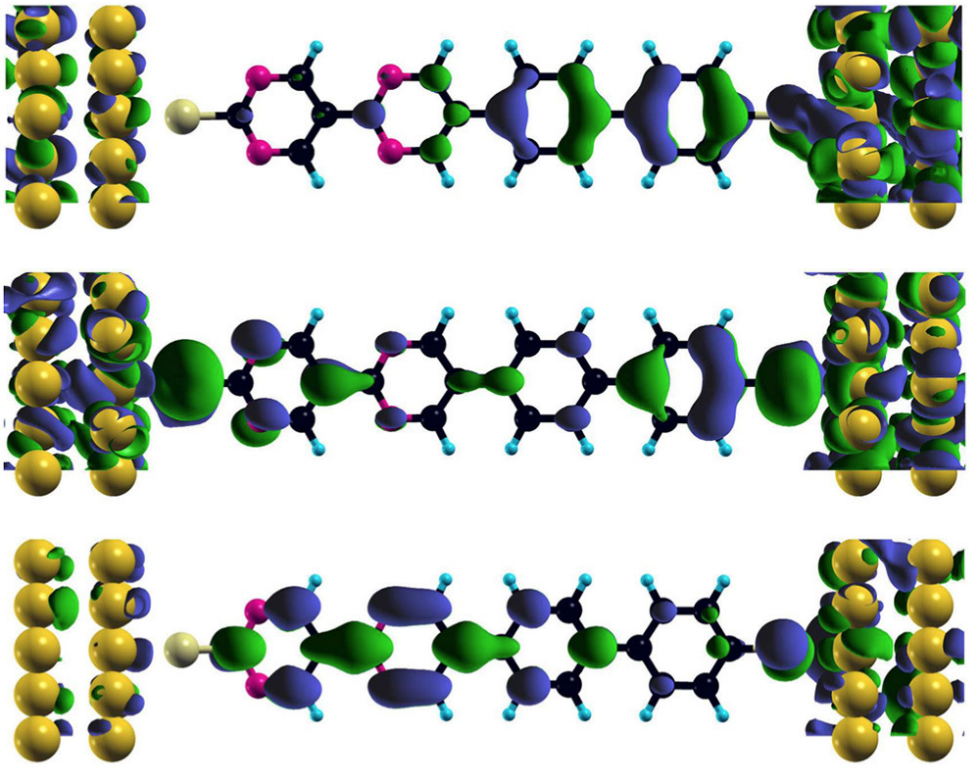

Figure 5.5: Transmission wavefunctions of the dipyrimidinyl-diphenyl molecule, calculated with ASIC, showing the HOMO−1 (top), HOMO (middle), and LUMO (bottom).

peak crosses the Fermi energy at this voltage. As expected for a molecular diode, the current under negative bias is finite [46]. The bias-dependent transmission coefficients shown in Fig. 5.7 (obtained at the ASIC level) reveal under bias (both positive and negative) a shift of the HOMO peak towards the Fermi energy, accompanied by a loss of intensity. This corresponds to a high slope in the I-V characteristics when the HOMO peak enters the bias window. Moreover, since the LUMO peak shows hardly any shift, the HOMO-LUMO gap is reduced. The transport is hole dominated at low bias, because the tail of the HOMO peak contributes at the Fermi energy much more than that of the LUMO peak, which starts playing a role only at higher bias, see Fig. 5.7. We can now also understand the asymmetry of the I-V characteristics: The overlap of the black curve with the green bias window is larger for positive than

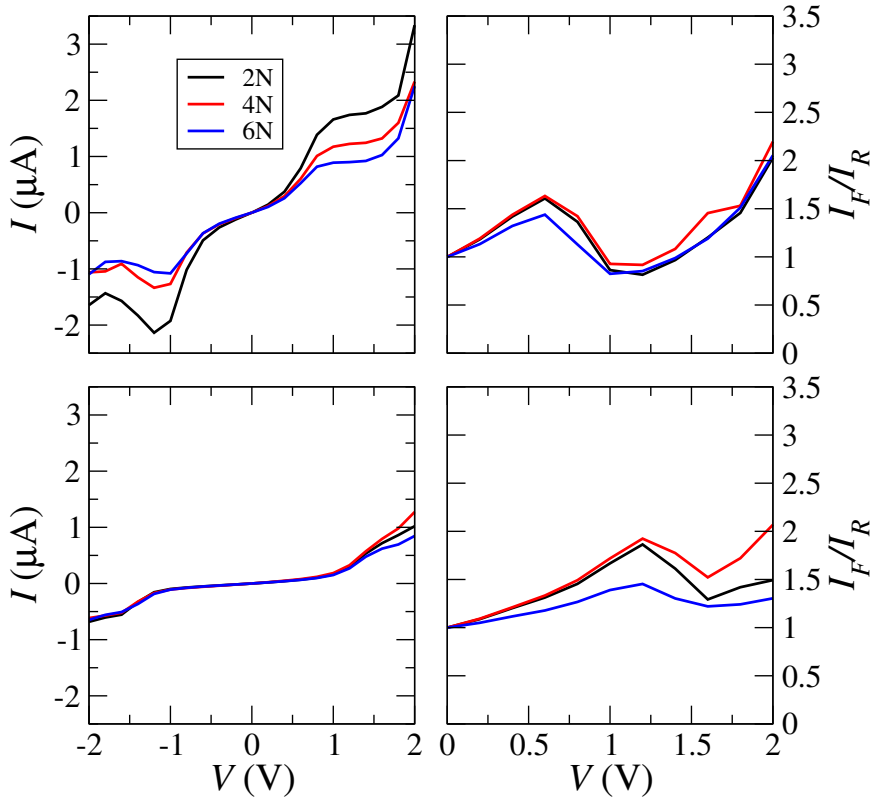

Figure 5.6: Current-voltage characteristics (left) and rectification behavior (right). The top panels present LDA results and the bottom panels ASIC results.

for negative bias of the same magnitude.

5.5 Hypothetical Configurations

It can be expected that two molecular diodes connected in series improve the rectification behaviour. To investigate this situation, we couple two dipyrimidinyl-diphenyl molecules by means of a σ-type C-C bond in the transport direction, see the tandem configuration shown in Fig. 5.8(left,top). In addition, we rearrange the order of the phenyl and prymidinyl rings in this configuration such that the structure has maximal asymmetry, see Fig. 5.8(left,bottom). The zero-bias transmission coefficient of the tandem configuration [Fig. 5.9(a)] shows close similarity to the 4N configuration [Fig. 5.3] concerning the HOMO-LUMO gap. The intensity of the HOMO peak is

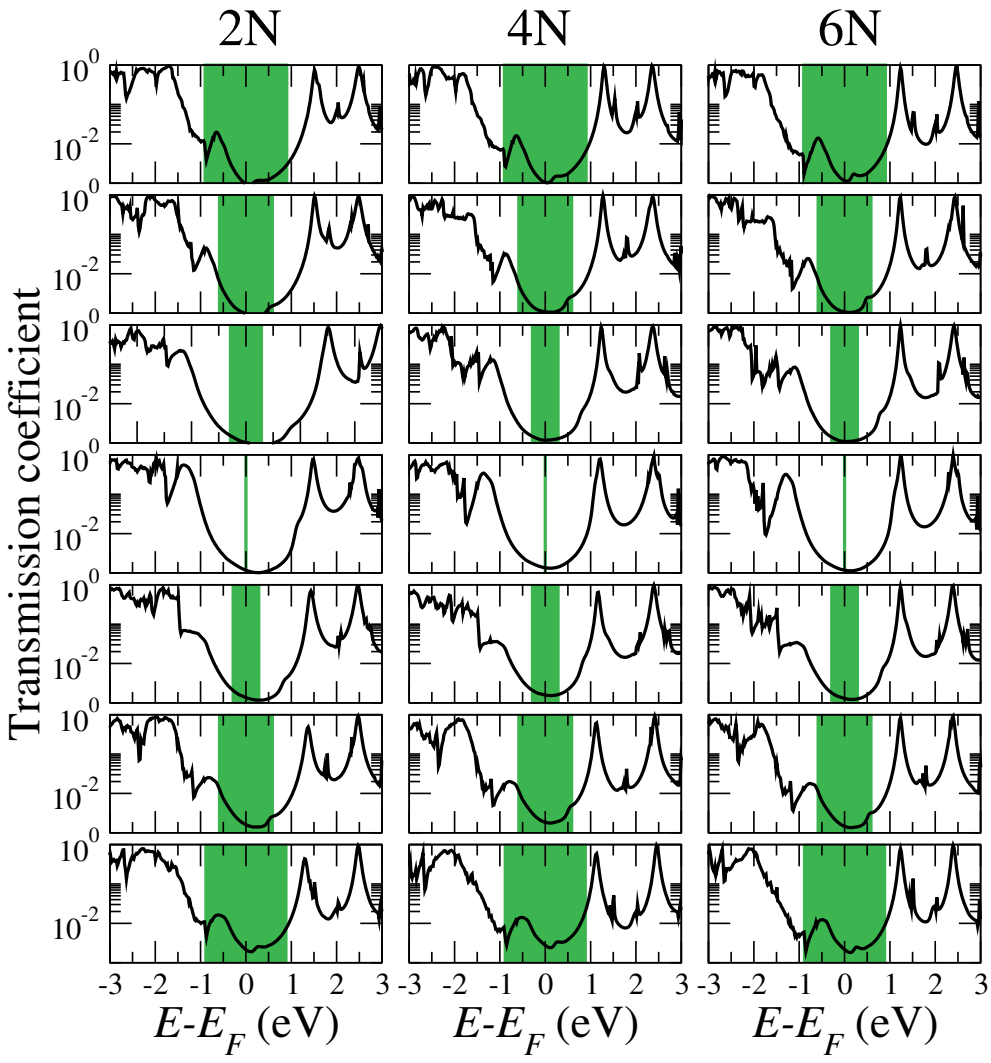

Figure 5.7: Finite-bias transmission coefficients of the 2N (left), 4N (middle), and 6N (right) configurations obtained with ASIC for bias voltages of (top to bottom, in V): −1.8, −1.2, −0.6, 0, 0.6, 1.2, and 1.8. The bias window is marked by green color.

significantly reduced because of the serial arrangement of two molecules. According to Fig. 5.8(right,top), the transmission wave function of the LUMO (at zero bias) is delocalized essentially over the whole molecule and declines towards the electrodes. Therefore, the system cannot be understood in terms of the two coupled molecules but acts as an entity. For the asymmetric configuration the intensity of the LUMO peak is significantly reduced, since the transmission wavefunction in Fig. 5.8(right,bottom) is much more localized than for the tandem configuration.

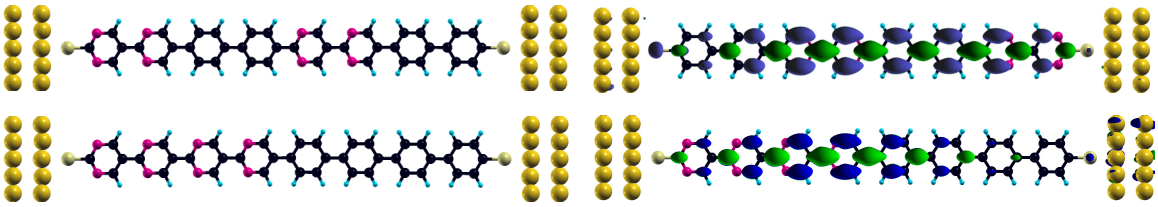

Figure 5.8: Structures (left) and transmission wave functions (right) of the tandem (top) and asymmetric (bottom) configurations, see the text for details.

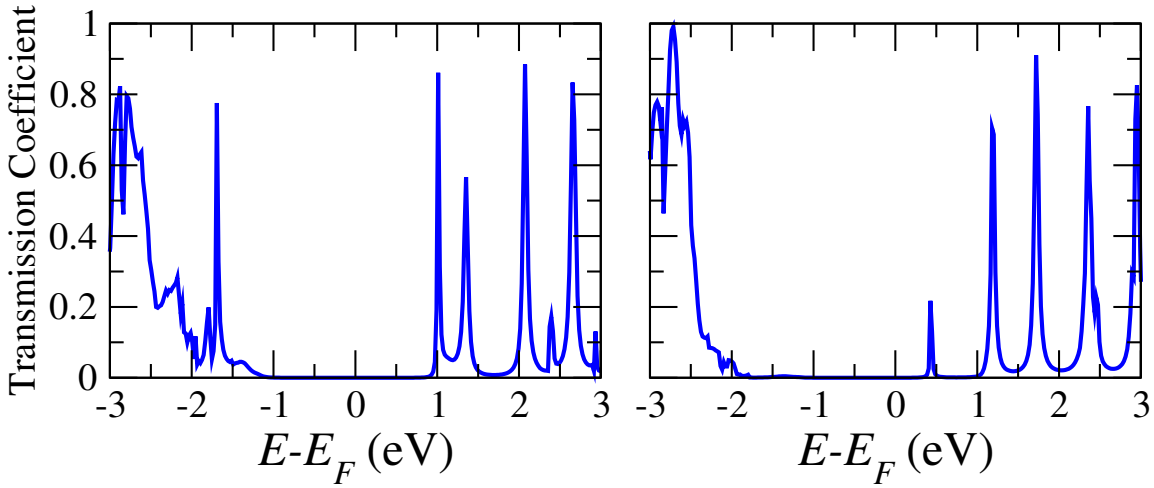

Figure 5.9: Zero-bias transmission coefficients of the tandem (left) and asymmetric (right) configurations, calculated with ASIC.

Figure 5.10 shows for the tandem configuration a higher threshold voltage of about 1.4 V, because the tail of the HOMO transmission peak is strongly suppressed (which becomes obvious on a logarithmic scale), as well as a slightly improved rectification behaviour, as compared to the 4N configuration [Fig. 5.6]. The I-V characteristics of the asymmetric configuration in Fig. 5.10 reveals as a new feature a significant current under positive bias, because the LUMO transmission peak has shifted much closer to the Fermi energy, see Fig. 5.9(right), and therefore now carries the current. Since under negative bias the current is as small as for the tandem configuration, Fig. 5.10 demonstrates a strongly enhanced rectification behaviour of the asymmetic configuration at small voltages.

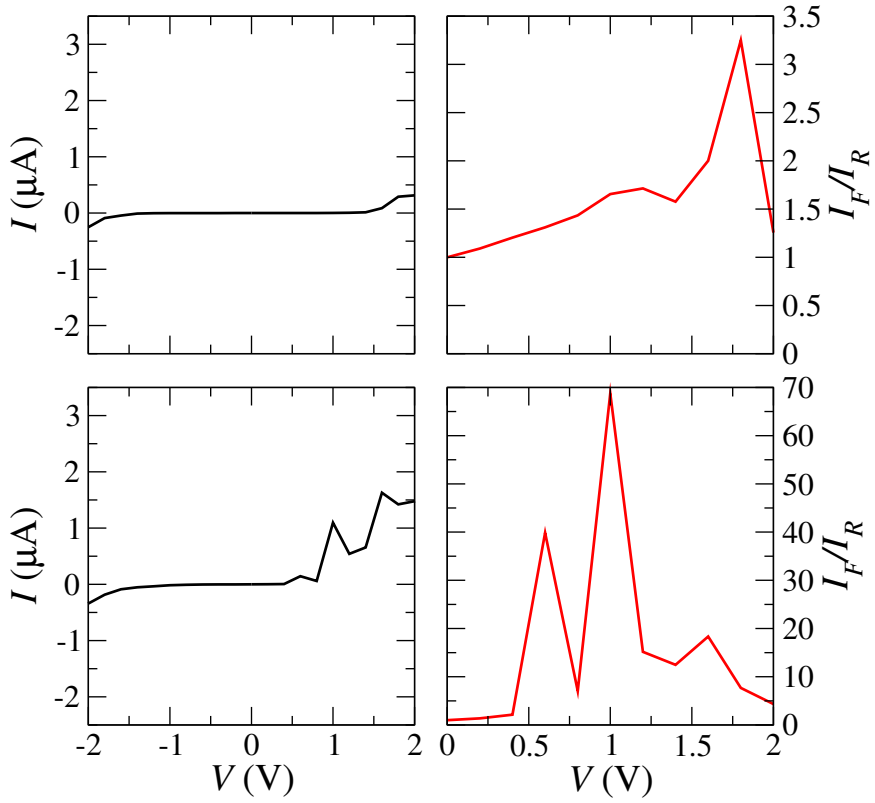

Figure 5.10: Current-voltage characteristics (left) and rectification behavior (right). The top panels refer to the tandem configuration and the bottom panels to the asymmetric configuration.

5.6 Summary

In summary, we have studied the potential of the dipyrimidinyl-diphenyl molecule and its derivatives in rectifier applications. In particular, we have investigated the roles of the acceptor and donor rings and the consequences when their ratio is changed. Serial connection of two molecules improves the rectification behavior and the threshold voltage as compared to a single molecule diode. When the pyrimidinyl and phenyl rings are sorted to maximize the asymmetry of the molecule, the rectification ratio is enhanced by about one order of magnitude, because the current now is due to the LUMO instead of the HOMO.

Chapter 6

Negative Differential Conductance in Two-Dimensional C-Functionalized Boronitrene

Two-dimensional materials today are attracting continuous interest for both basic scientific and technological reasons [190–192]. While graphene and its derivatives have been studied in detail, the interest in two-dimensional boron nitride, henceforth referred to as boronitrene, is growing rapidly. The material shares with graphene both the structure (lattice mismatch of 1.5%) and the total number of valence electrons of neighboring atoms. However, it is insulating with a very large band gap of 6.0 ± 0.5 eV [193]. Band gap tuning by functionalization with C has been realized by several groups and shows great potential for materials design, because the defects can be well controlled [194–197]. In particular, it recently has been demonstrated that the band gap can be reduced to the range required for typical semiconductor devices [198]. Indeed, materials based on B/C/N networks are interesting for numerous applications in nano-scale devices, energy harvesting, and catalysis, for example [199].

Heterostructures of boronitrene and graphene nowadays are subject of extensive

experimentally studies [200–202]. Interesting features, including negative differential conductance (increasing voltage leads to decreasing current and vice versa; Negative Differential Conductance (NDC)), have been reported, which can be exploited in low-noise amplification, high-frequency oscillators, analog-to-digital conversion, and digital logics, for example [203]. NDC also has been found in N-doped graphene [204] and oligophenylene molecules sandwiched between graphene electrodes [205]. Its origin can be related, for example, to the bias dependence of interface states [206, 207], the orientation of molecular ligands [208], the tunneling through localized states [209, 210], and the change of molecular charge states [211, 212]. In the present work we study C-functionalized boronitrene (C-BN) and demonstrate that defect design not only can reduce the band gap but even can result in metallicity. We analyze the two-dimensional transport behavior, focusing on the metallic cases, and find extraordinary I-V characteristics, including NDC.

6.1 Computational Details

We use density functional theory as implemented in the SIESTA code [130] with an atomic orbital double-zeta polarized basis set. The core electrons are described by norm-conserving Troullier-Martin pseudopotentials including scalar relativistic corrections. The cutoff energy is set to 600 Ry and the local density approximation (Ceperley-Alder flavor) is employed for the exchange-correlation functional. All technical parameters are converged carefully and all the structures under investigation are optimized with a force threshold of 0.04 eV/Å (first the geometry of the unit cell and afterwards the atomic positions). C atoms are substituted in boronitrene (xz-plane) along either the armchair or the zigzag direction (z-axis) of the honeycomb structure.

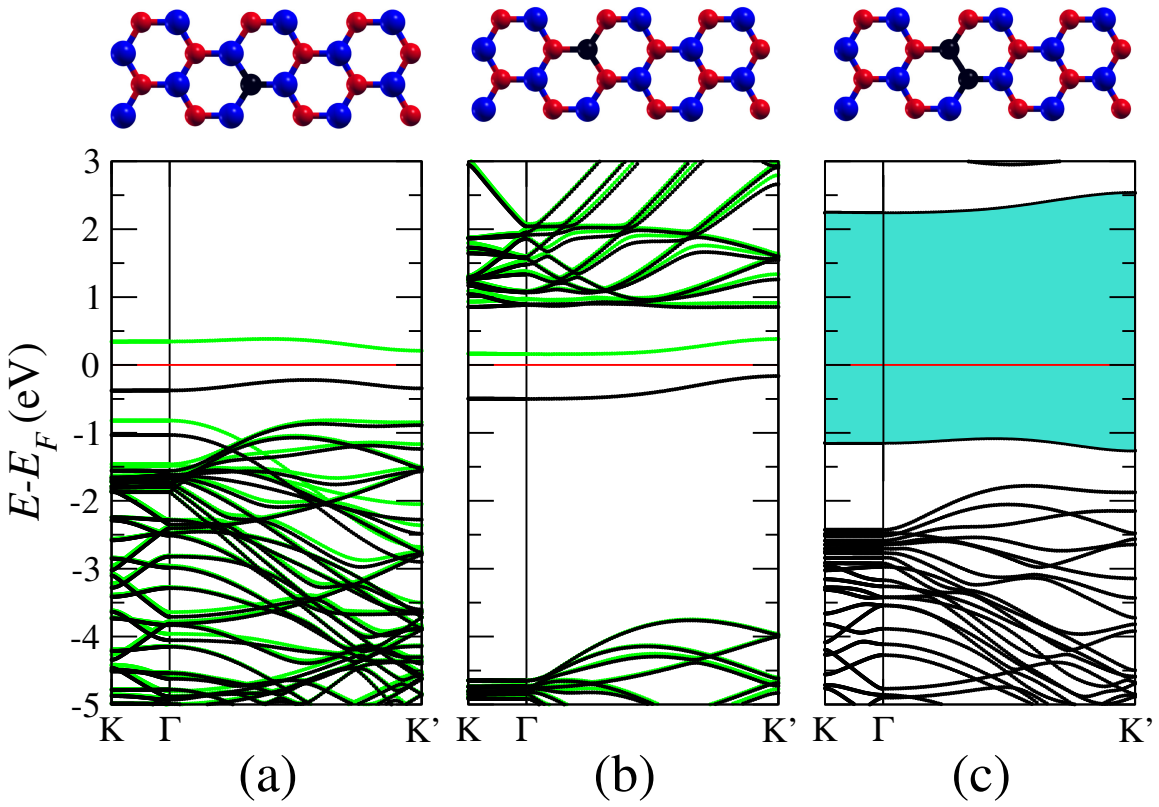

Figure 6.1: Band structures for (a) N substitution, (b) B substitution, and (c) BN pair substitution with C.

Transport calculations are performed using the optimized geometries in the non-equilibrium Green's function approach as implemented in the SMEAGOL code [76]. The same convergence criteria are used as in the electronic structure calculations. The current $I(V)$ is calculated using the transmission coefficient $T(E,V)$ and the Landauer formula, where the bias V is applied symmetrically to the electrodes. The complex integration to obtain the charge density is computed using 16 points on the semi-circle, 16 points parallel to the real axis, and 16 poles. At finite bias the integration over the real energies is evaluated using at least 500 points. An electronic temperature of 300 K is employed.

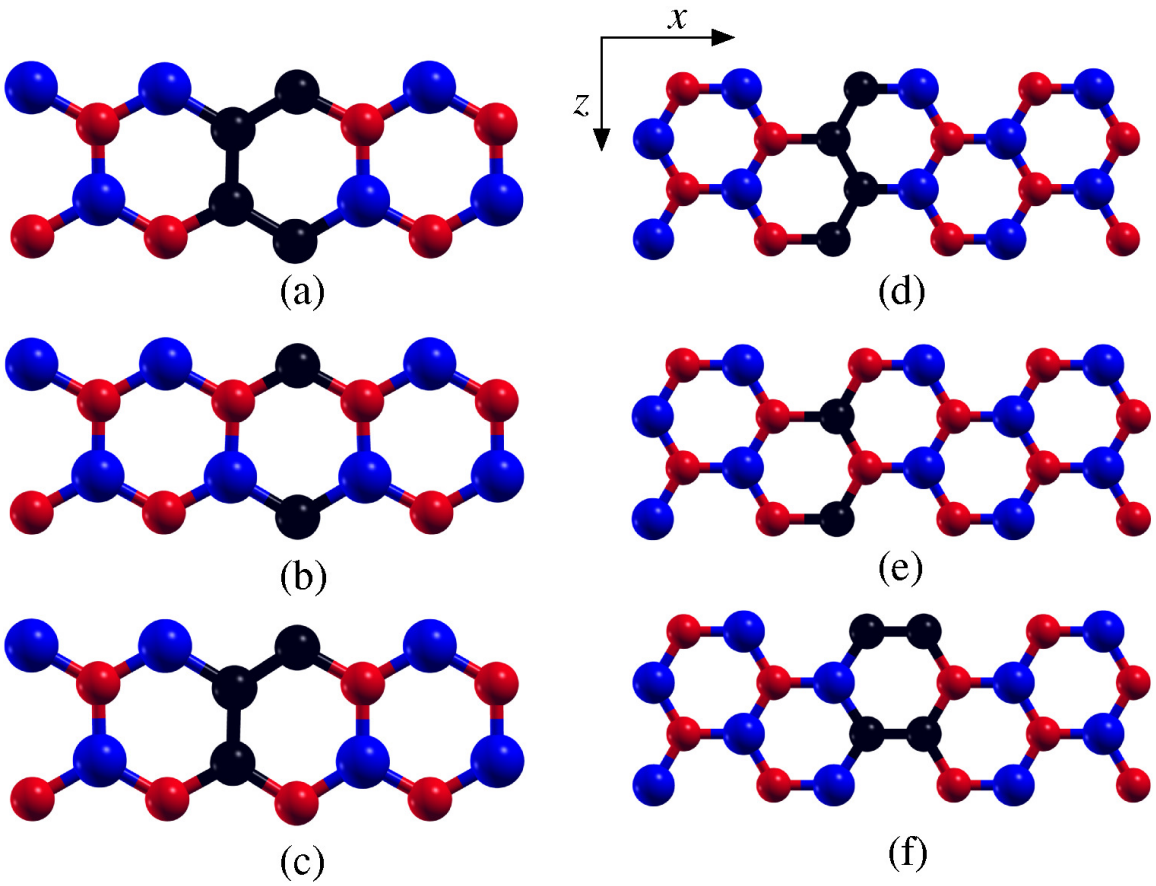

Figure 6.2: C-BN configurations under study: (a) armchair line, (b) armchair single, (c) armchair staggered, (d) zigzag line, (e) zigzag single, and (f) zigzag staggered.

6.2 Equilibrium State Properties

Substitutional C doping in boronitrene breaks the symmetry of the honeycomb structure (initial space group $P\bar{6}3mmc$, final space group $Pmma$). We present in the following band structures along the K-Γ-K′ path, where K=(0,0,$\frac{1}{2}$) and K′=($\frac{1}{2}$,0,0). Substitution of a single N and B atom, respectively, by C results in electron and hole doping, see Fig. 6.1(a,b). On the other hand, replacing a BN pair by two C atoms gives no qualitative change of the band structure but reduces only the band gap, see Fig. 1(c). We therefore have to turn to more complex substitution patterns in order to achieve specific properties. In the following we will study armchair line, single, and

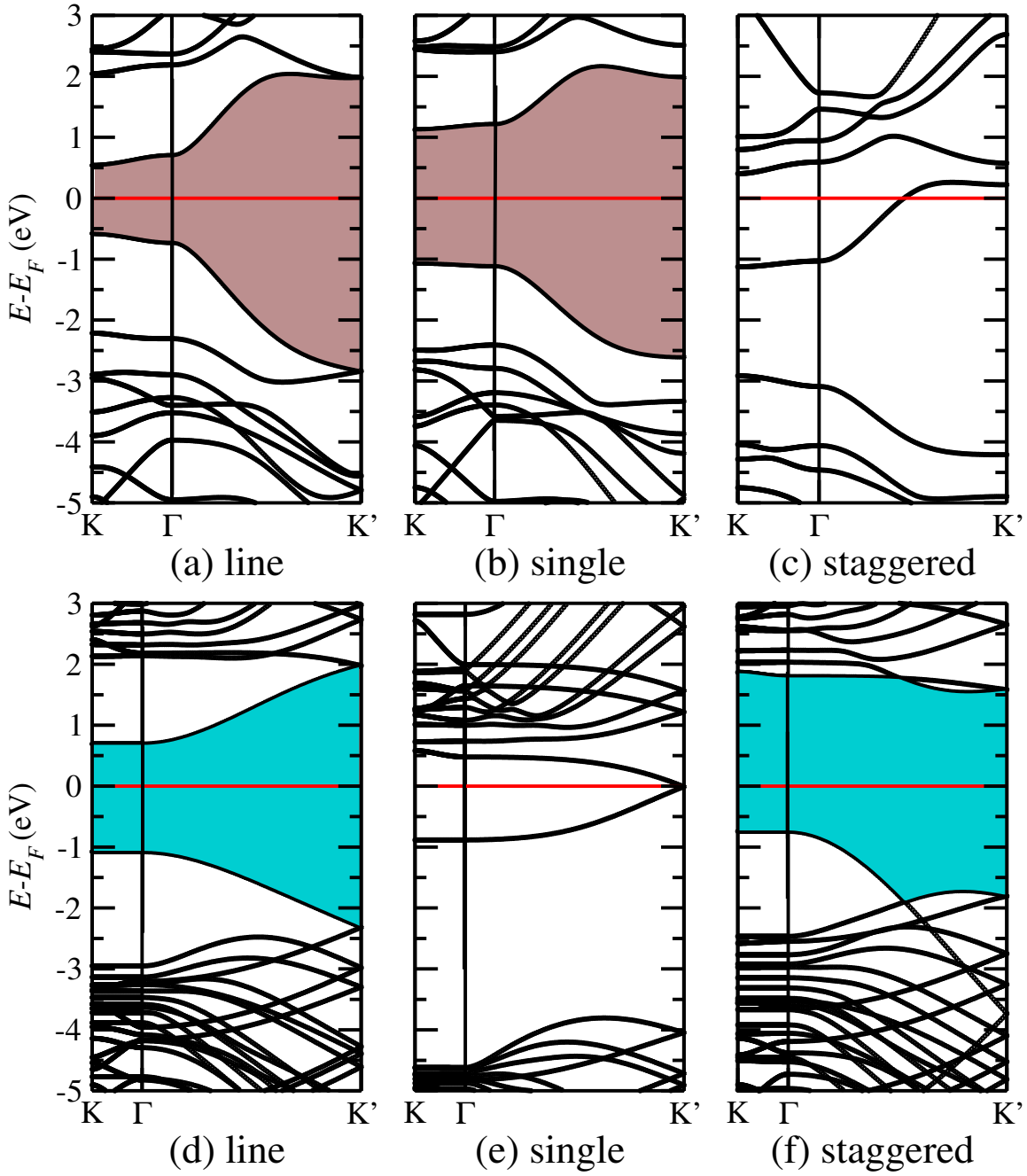

Figure 6.3: Band structures for the (a-c) armchair and (d-f) zigzag C-BN configurations defined in Fig. 2.

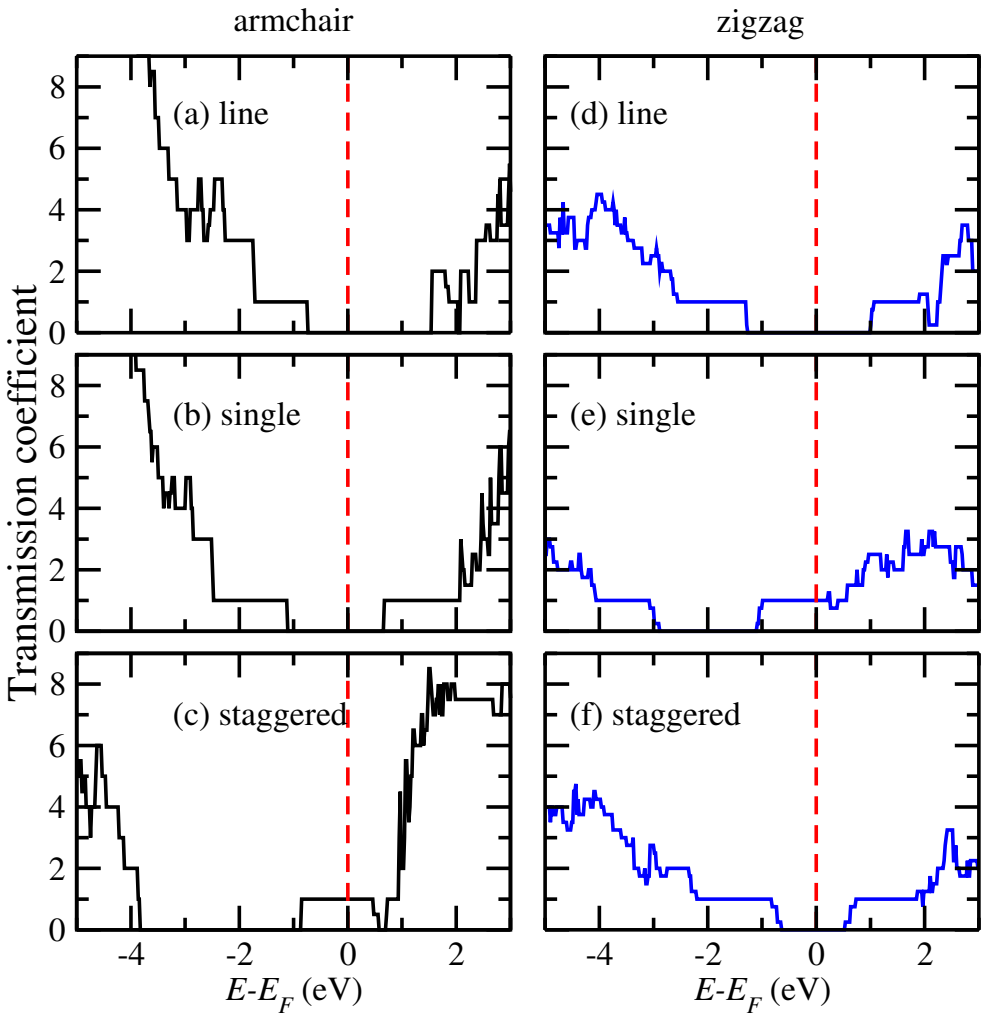

Figure 6.4: Transmission coefficients at zero bias for the (a-c) armchair and (d-f) zigzag C-BN configurations defined in Fig. 2.

staggered configurations, see Fig. 6.2(a-c), and the respective zigzag configurations, see Fig. 6.2(d-f).

According to Fig. 6.3(a,b) the armchair line and single configurations have reduced direct band gaps of 1.1 eV and 2.5 eV, respectively, as compared to the theoretical (4.6 eV) [213] and experimental (6.0 ± 0.5 eV) [193] values of boronitrene. As to be expected, when more C atoms are introduced the reduction is more pronounced. The band gaps in Fig. 6.3(a,b) appear at the K point, which represents the transport direction in real space. Since in the armchair line and single configurations the same

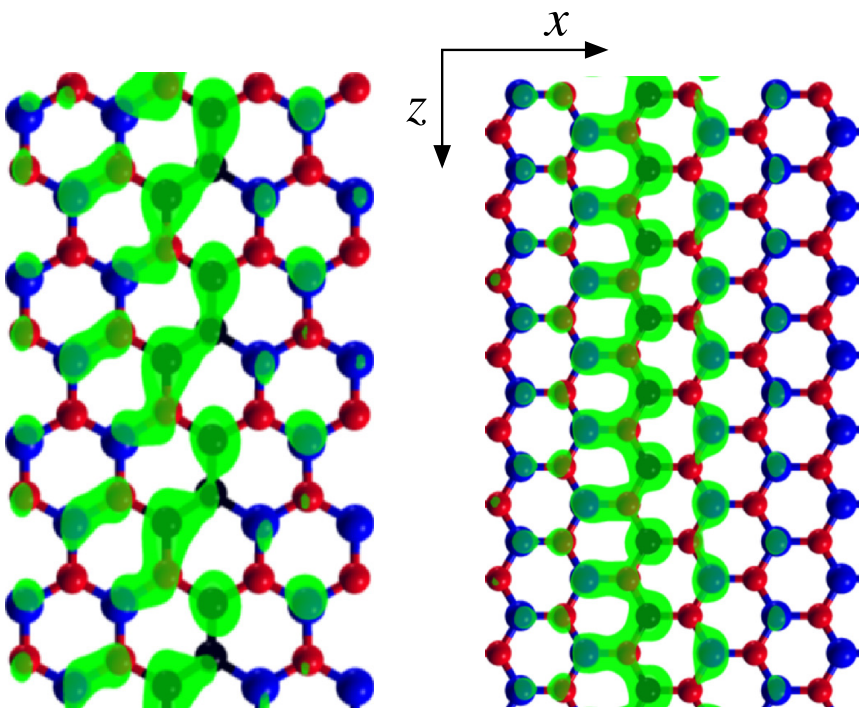

Figure 6.5: Isosurface of the modulus of the transmission wavefunction, showing the contributions to the transmission at the Fermi energy for the metallic configurations. The isovalue is 0.015 electrons/a_B^3.

amount of B and N atoms is substituted by C atoms, the conduction band minimum and valence band maximum in these cases are formed by π and π^* bands, respectively. On the other hand, for the armchair staggered configuration we obtain a metallic nature, see Fig. 6.3(c), due to the extra electron introduced by replacing two B atoms and only one N atom per supercell by C atoms.

For the zigzag line and staggered configurations (being charge neutral substitutions) we observe band gaps of 2.3 eV and 1.6 eV, respectively, see Fig. 6.3(d,f). Since the latter has both an indirect (2.3 eV) and a direct (2.5 eV) band gap, it is interesting from the optical perspective, even though the energy difference between the two band gaps is relatively small. The zigzag single configuration, see Fig. 6.3(e), is found to be semiconducting, because the two extra electrons per supercell introduced

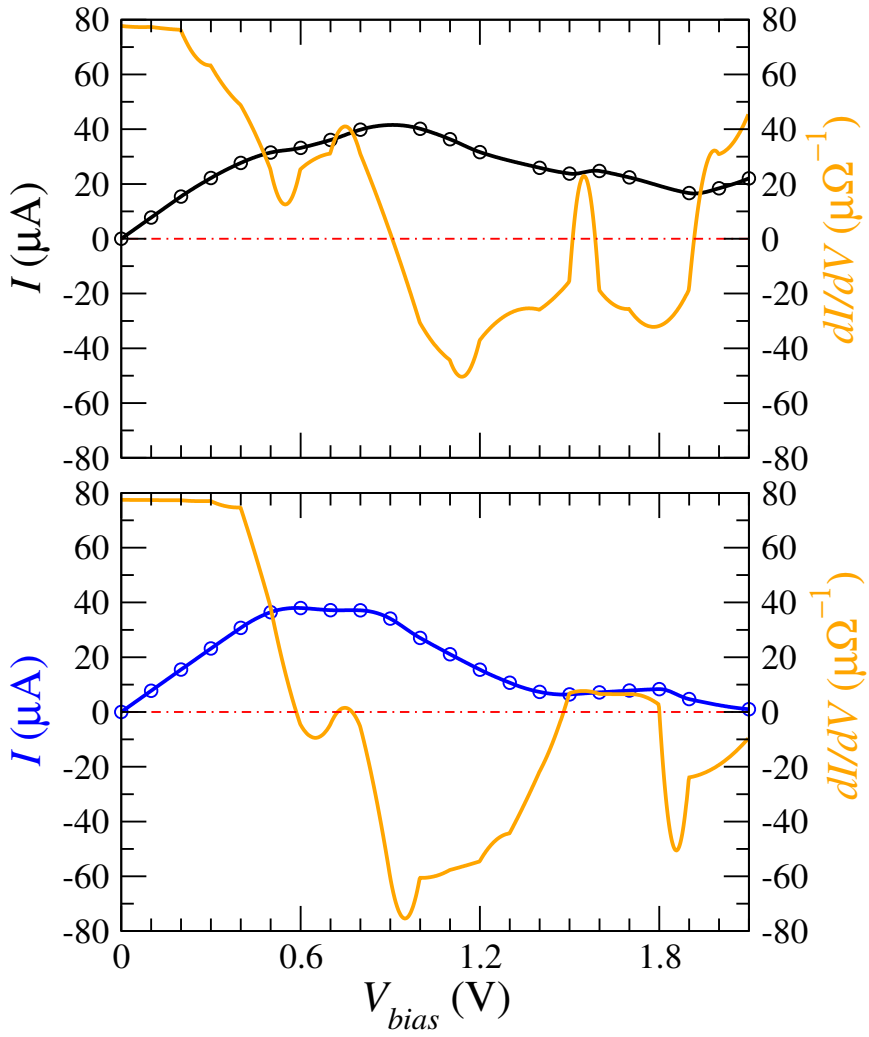

Figure 6.6: I-V characteristics for the (top) armchair staggered and (bottom) zigzag single configurations.

by replacing two B atoms by C atoms fill an additional band. Interestingly, the band gap is exactly zero, which gives rise to a Dirac-like spectrum at the K′ point. The consequences are discussed below.

The zero bias transmission coefficient $T(E, V = 0)$ is presented in Fig. 6.4 for the six configurations under investigation. Absence of a transmission channel at the Fermi energy in Fig. 6.4(a,b,d,f) reflects the semiconducting characters as mentioned before. On the other hand, we find a single transmission channel at the Fermi energy in Fig. 6.4(c,e), reflecting conductance quantization in the characteristic form of a one-

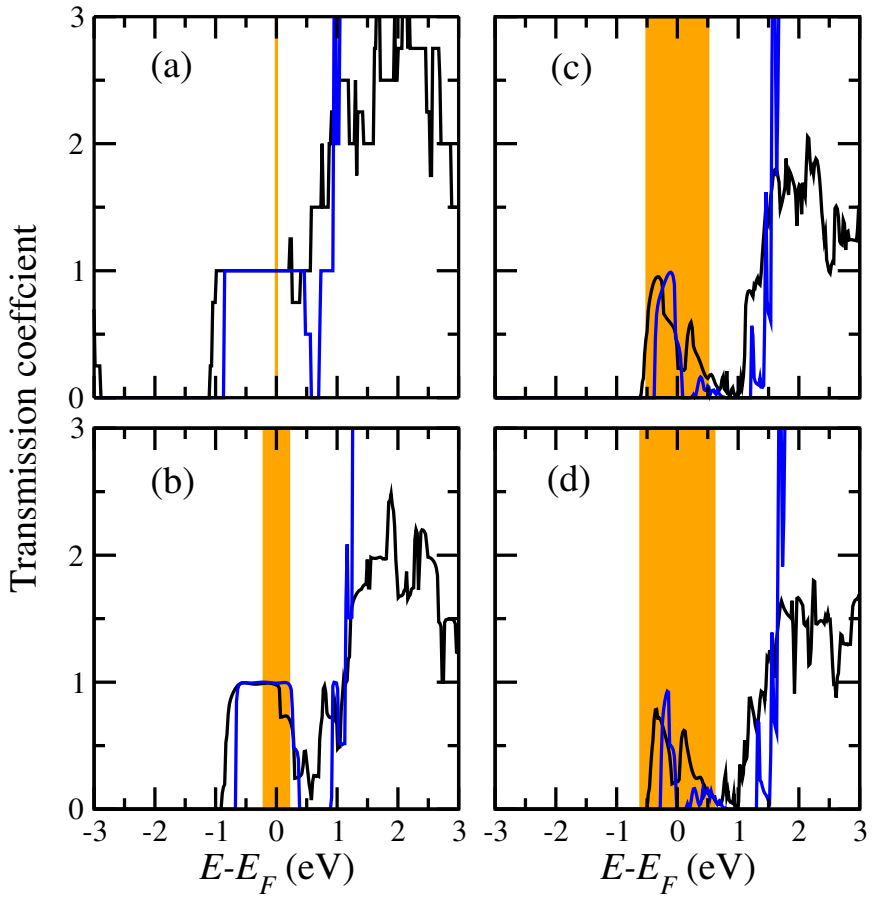

Figure 6.7: Transmission coefficients at biases of (a) 0 V, (b) 0.4 V, (c) 1 V, and (d) 1.2 V for the (black) armchair staggered and (blue) zigzag single configurations. Orange color highlights the bias interval.

dimensional wire. Figure 6.5 shows for the metallic configurations isosurface plots of the transmission wavefunction, representing the probability to find a charge carrier at a specific point in space. The results suggest transport through the π conjugated states (p_z-like eigenchannels). The amplitude of the wavefunction decays fast away from the defects.

6.3 Finite Bias Calculations

High bias voltages are needed for tunneling electrons through the semiconducting configurations because of the rather large band gaps. For the metallic armchair

staggered and zigzag single configurations the dependence of the current on the bias voltage, $I(V)$, is presented in Fig. 6.6. Both systems behave ohmic for small bias, as reflected by flat regions in the dI/dV curves. At higher bias we obtain a strongly non-linear behavior of $I(V)$ with regions of n-type NDC. The first such region appears for the armchair staggered configuration between 0.8 V and 1.5 V and for the zigzag single configuration between 0.6 V and 1.5 V. The corresponding peak-to-valley ratios are 1.8 and 6.5, respectively. These values are comparable to literature data for crystalline silicon for different doping levels [214, 215]. For graphene nanoribbons of various widths values between 1.3 and 10 have been reported [216]. Importantly, the order of magnitude is appropriate for application in switches and memory devices [217, 218].

Figure 6.7 shows the bias-dependent transmission coefficient, $T(E, V)$, which gives insight into the origin of the observed NDC. Reference biases of 0 V, 0.4 V, 1 V, and 1.2 V are investigated. We find a drastic reduction in the tunneling for increasing bias voltage both for the armchair staggered and zigzag single configurations in the non-ohmic region ($V > 0.2$ V). We observe also a change in the energy dependence of $T(E, V)$ around the Fermi energy for the higher biases within the entire bias interval (orange color). This modification of the mobility of the charge carriers combined with the changes of the available states in the leads under bias gives rise to the observed NDC.

6.4 Summary

In summary, we have investigated the potential of C-functionalized boronitrene in amplifier or switching devices. The material can be tuned from insulating to semiconducting and further to metallic bevavior by means of the orientation (zigzag or

armchair) and shape of the C defects. We have determined the electronic transport through C-functionalized boronitrene employing the non-equilibrium Green's function formalism within a first-principles framework. In general, the material develops a versatile nature with promising electronic properties due to the functionalization. In particular, we observe bias regions of NDC for specific defect configurations with high peak-to-valley ratios. Our approach allows us to systematically understand the transport characteristics in terms of the energy and bias-dependent transmission coefficient and wavefunction.

Chapter 7

Magnetoresistance of Mn-decorated Topological Line Defects in Graphene

Carbon nanomaterials [219], such as graphene, fullerenes [220], and nanotubes [221], host exciting physical and chemical phenomena and therefore are provoking a lot of scientific activity. The spatial confinement of the electronic states in such systems is key for their properties and also determines the interaction with other matter. In its ideal form, graphene consists of a two-dimensional honeycomb lattice of sp^2 hybridized C atoms. However, various structural imperfections can arise, for example line defects, for which the formation of pairs of pentagonal and octagonal rings allows the system to reduce the internal strain. This defect with fractional chirality was predicted previously for nanotubes [222] and, referring to the arrangement of the rings, is called 8-5-5-8 topological line defect. It has been observed in as-growngraphene [223] and can also be induced in a controlled fashion by electron irradiation [224, 225]. In general, the intentional introduction of defects into graphene is a topic that currently receives enormous attention, because it can lead to a multitude of applications [226–

232]. Moreover, the interactions between defects in graphene and metal atoms have been explored extensively in the literature [233–237]. Selective deposition of Pt atoms at graphene line defects recently has been demonstrated in Ref. [238].

Magnetic sensors based on the magnetoresistance of a material have been investigated intensively for quite a while [239, 240]. In addition, magnetoresistant materials are of great interest in the field of spintronics, see Ref. [241] and the references therein. In this context, graphene nanoribbons recently were found to offer high magnetoresistance [242], although rough edges lead to enhanced scattering and little control over the material properties. Moreover, the growth of nanoribbons on a substrate always introduces some amount of disorder [243]. On the other hand, adsorption of transition-metal atoms can be utilized to introduce spin polarization in graphene [244]. In addition, at least for a low concentration of adatoms, the magnetization can be tuned by varying the Fermi energy, either by applying a gate voltage or by suitable doping [245]. Since adsorption and desorption on surfaces are largely controlled by surface defects [246], stable line defects in graphene are expected to trigger a selective decoration, which is useful for engineering spin transport channels. The one-dimensional transport through such an arrangement resembles that through an atomic wire. However, the distance between the magnetic centers in decorated line defects is typically much too large to induce magnetoresistance. In this chapter work, we propose a strategy to overcome the limited controllability that graphene nanoribbon edges suffer from. For introducing spin polarization and magnetoresistance in graphene, we decorate a 8-5-5-8 topological line defect with Mn atoms. Strong preferential bonding results in very stable structures. Despite the large distance between the magnetic centers, we demonstrate a high magnetoresistance mediated by RKKY interaction. This effect is explained by a very strong induced π magnetism of the graphene host, which results in directed spin transport.

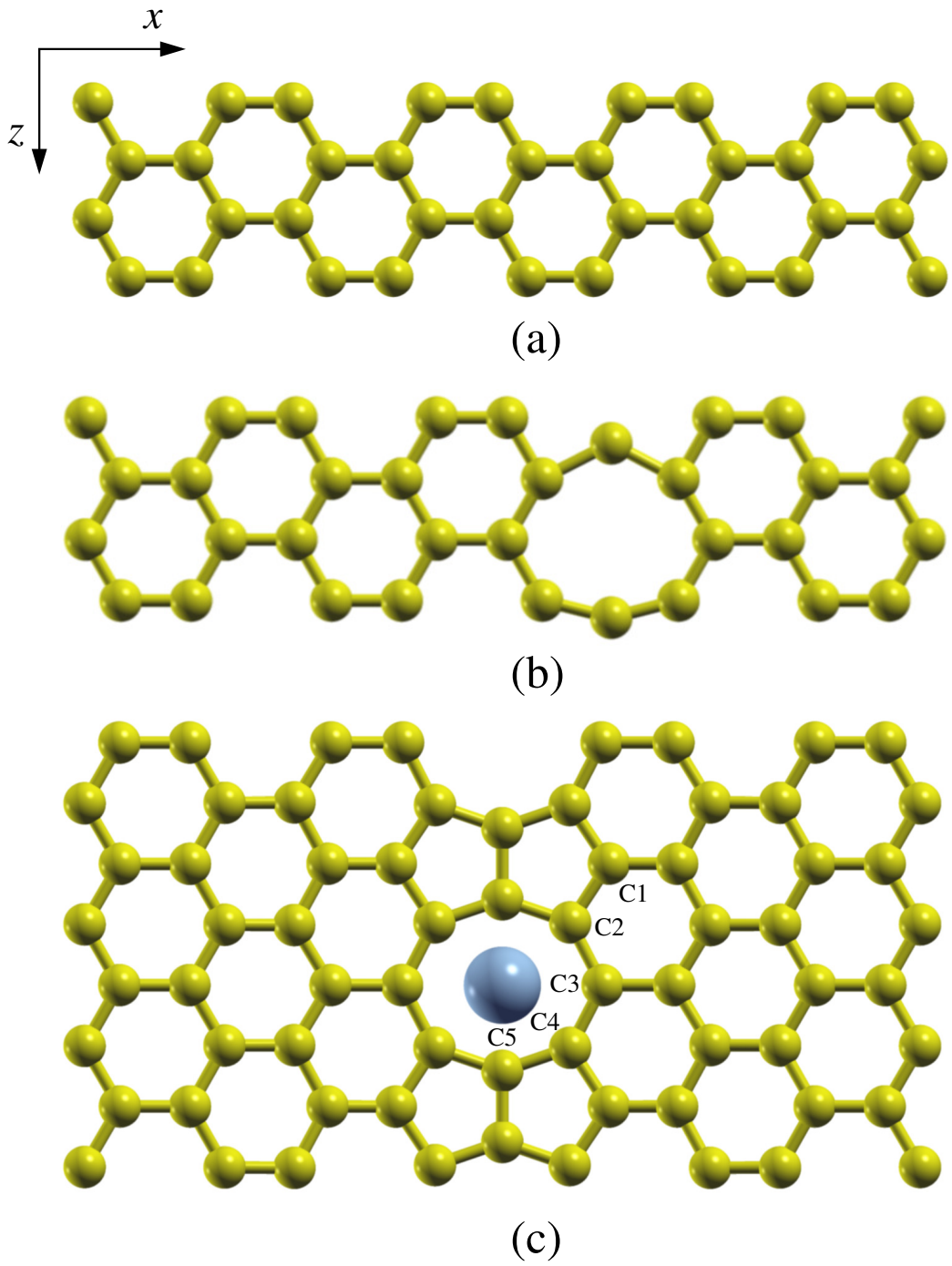

Figure 7.1: Structure of (a) graphene, (b) graphene with line defect, and (c) graphene with 50% Mn-decorated line defect. The labeling of the C atoms takes into account the symmetry of the structure.

7.1 Computational Details

Our calculations are based on density functional theory and the generalized gradient approximation to the exchange correlation potential in the Ceperley-Alder flavor. We use the SIESTA code [247], which employs linear combinations of atomic orbitals as basis functions (double zeta polarization) and norm-conserving pseudopotentials. An energy cutoff of 300 Ryd is used. The pseudopotentials and basis sets have been tested for diamond as well as graphite. Moreover, the Brillouin zone is sampled on a $30 \times 1 \times 30$ Monkhorst-Pack k-mesh. Geometry optimizations are carried out by the conjugate gradient method until the forces acting on the atoms have declined below 0.04 eV/Å^{-1}. Band structures are studied along the high symmetry direction $\Gamma-$K and along the topological line ($\Gamma-$C). The transport is determined by the nonequilibrium Green's function approach as implemented in the SMEAGOL package [76], where the scattering region consists of 8 replica of the cell shown in Fig. 7.1(a), stacked along the z direction, and each lead of 2 replica. The cell of defective graphene is shown in Fig. 7.1(b). Since Mn decoration is favorable on the line defect irrespective of the Mn coverage [248], we address the cases of 50% and 100% occupation of the octagonal rings, see Fig. 7.1(c). Periodic boundary conditions are imposed to the leads, making them semi-infinite, and the electronic temperature is set to 300 K. The technical parameters are the same as in the electronic structure calculations, except that a $5\times1\times1$ k-mesh is used. We do not take into account the spin orbit interaction, since the effects are expected to be negligible.

The spin dependent current $I_\alpha(V)$ is obtained from the Landauer-Büttiker formula in Eqn. 2.51 and given as,

$$I_\alpha(V) = \frac{e}{h}\int_{-\infty}^{\infty} T_\alpha(E,V)[f_L(E-\mu_L) - f_R(E-\mu_R)]dE, \tag{7.1}$$

where $\mu_{L/R}$ is the chemical potential of the left/right electrode, V the applied bias voltage, $f_{L/R}$ the Fermi-Dirac distribution function, T_α the transmission, and α the spin. The spin dependent zero bias conductance is

$$G_\alpha(E) = \frac{e^2}{h} T_\alpha(E) = \frac{e^2}{h} \mathrm{Tr}[\Gamma_L G^R \Gamma_R G^A]_\alpha, \tag{7.2}$$

where Γ_L/Γ_R is the broadening matrix of the left/right electrode and $G^{R/A}$ the retarded/advanced Gren's function. Introducing the quantum of conductance, $G_0 = 2e^2/h$, we have $G_\alpha(E = E_F) = G_0 T_\alpha(E_F)/2$. The total conductance amounts to $G(E) = \sum_\alpha G_\alpha(E)$. Moreover, we define the magnetoresistance as [249, 250]

$$\mathrm{MR} = \frac{G_P - G_{AP}}{G_P}, \tag{7.3}$$

where P and AP, respectively, denotes parallel and antiparallel alignment of the magnetizations of the two electrodes.

7.2 Equilibrium State Properties

Pristine graphene is non-magnetic and shows a characteristic Dirac cone at the Fermi level, see Fig. 7.2(a). Even though in the line defect the C coordination remains three (with bond angles between 90° and 150°), the band structure is modified prominently, see Fig. 7.2(b). Particularly, the system becomes metallic, while remaining non-magnetic. The Dirac cone shows strong deformations and a slight energetic shift, so that the Dirac point appears 0.07 eV below the Fermi energy.

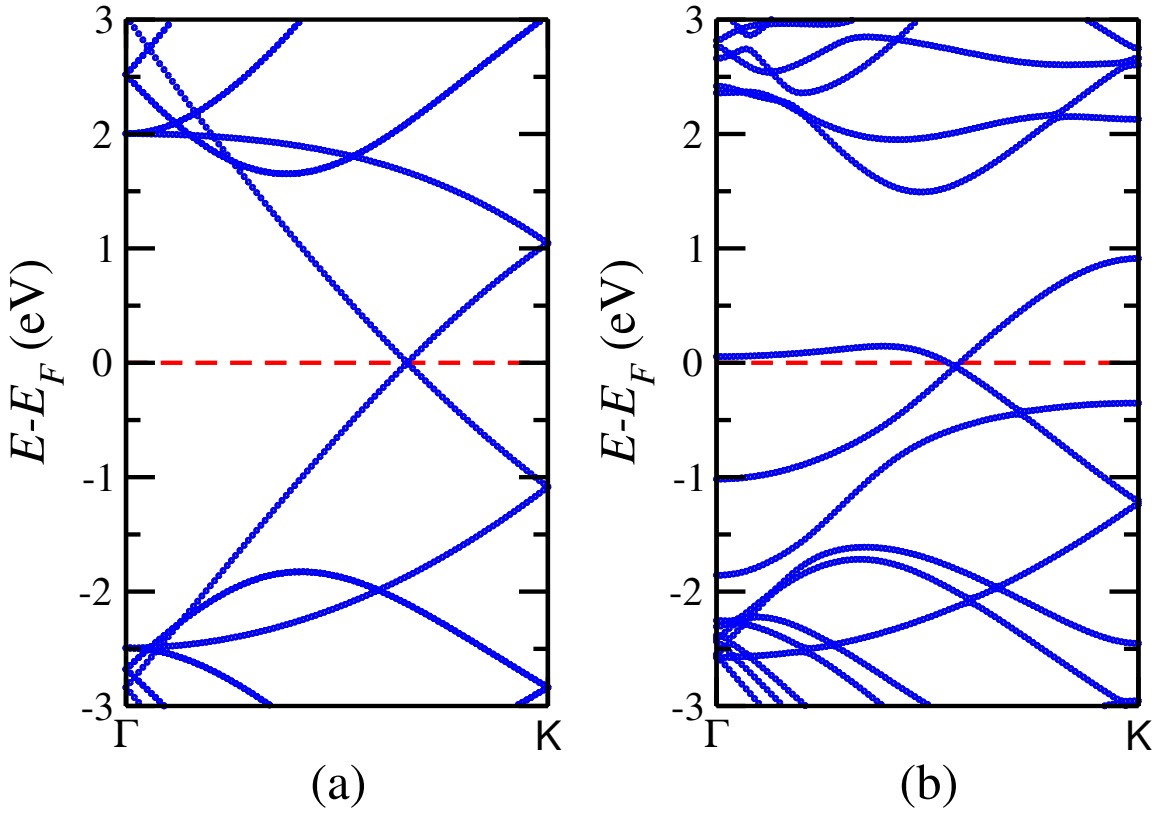

Figure 7.2: Band structures of graphene (a) without and (b) with line defect. Both cases show spin degeneracy.

Table 7.1: Magnetic moments (in μ_B) and C-Mn distances (in Å) for 50% and 100% Mn-decorated line defects.

	50%		100%	
site	moment	distance	moment	distance
C1	0.01	3.80	0.05	3.32
C2/C4	0.06	2.73	0.13	2.12
C3	0.06	2.82	0.03	2.30
C5	0.10	2.67	−0.02	2.34
Mn	0.22	—	0.10	—

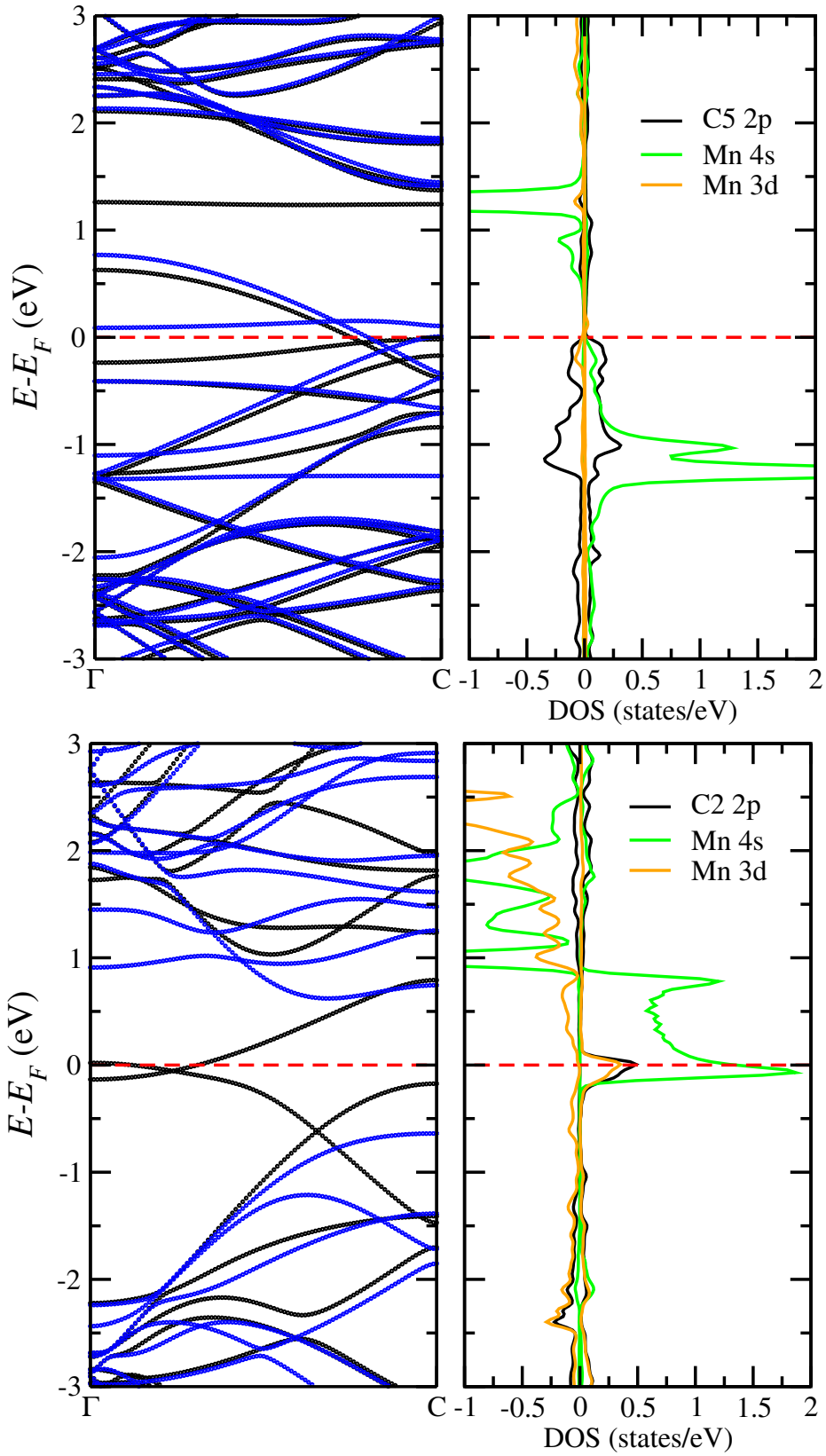

Figure 7.3: Spin polarized band structures and partial densities of states for (top) 50% and (bottom) 100% Mn coverage.

We find that Mn atoms are most favorably absorbed on top of the C octagonal rings, confirming Ref. [248], and thus form an atomic chain along the line defect. The adsorption energy (energy difference before and after adsorption) per Mn atom amounts to -0.82 eV and -0.53 eV for 50% and 100% coverage, respectively, and, according to Table I, the spin polarization of Mn is also very different (magnetic moments of 0.22 μ_B and 0.10 μ_B). Both comes along with significantly shorter distances of the Mn atoms to the graphene sheet for high coverage. As a consequence of these deviating structural relaxation patterns, the Mn densities of states in Fig. 3 exhibit distinct differences for the two systems. In particular, the width of the Mn 4s states is significantly enhanced, reflecting a strong interaction. Importantly, we observe that the Mn atoms induce substantial spin polarization of the electronic states at the neighboring C sites, see Table I. The effect is enhanced for 100% Mn coverage, particularly at the Fermi energy, where we find a pronounced spin majority peak of strongly hybridized Mn and C states. The distance between the magnetic centers is shorter and thus the spin polarization is much less localized than in the case that neighbouring C octagons do not host Mn atoms (50% Mn coverage). The widely spread spin polarization creates a continuous path of polarized states along the line defect (C1-C2-Mn/C3-C4-C1-...) for full Mn coverage only.

Adsorption of Mn on the top of the octagonal rings induces magnetic moments of 4.99 and 5.07 μ_B for 100% and 50% coverage, respectively. Thus, the Mn coverage influences the magnetism only slightly. We have calculated the energy difference between antiferromagnetic and ferromagnetic ordering of the Mn magnetic moments along the line defect and find the ground state to be ferromagnetic with an energy preference of 0.17 eV per Mn atom. Band structures and densities of states for the Mn-decorated systems are shown in Fig. 7.3. The band structures show that for 50% Mn coverage both spin channels are metallic, while 100% Mn coverage results in a

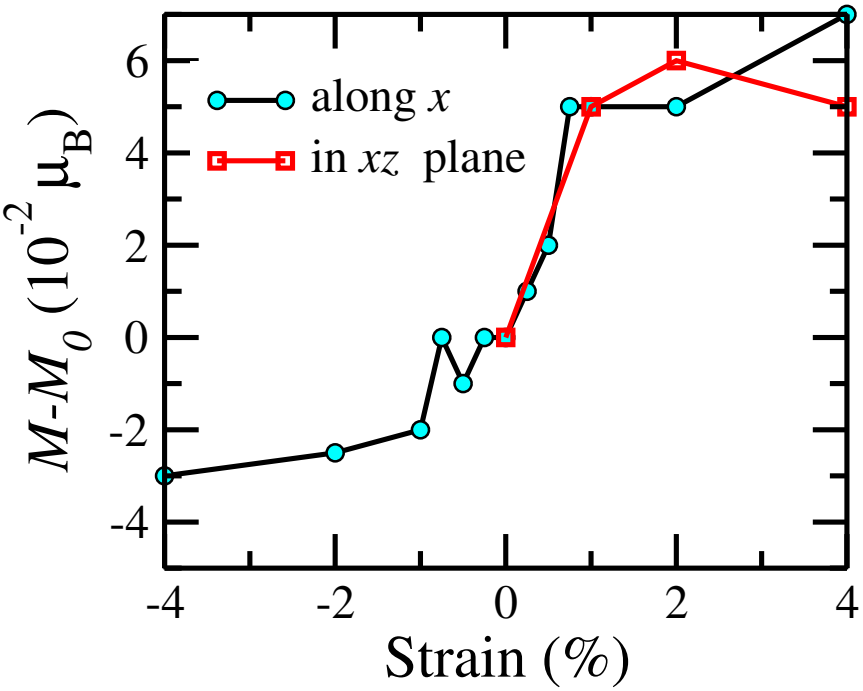

Figure 7.4: Modification of the total magnetic moment by strain along the x axis and in the xz plane for 100% Mn coverage.

half-metallic nature. In the latter case strong hybridization between the Mn and C2 states is visible in the density of states at the Fermi energy.

Table I shows the magnetic moments of the Mn and neighboring C atoms for both coverages. The rather small values obtained for Mn are due to strong interaction with the adjacent C atoms, as evidenced by the mentioned Mn-C hybridization. Accordingly, the C neighbors develop a partially very significant spin polarization. We have also studied to which extent the Mn-C coupling can be modified by uniaxial or biaxial strain due to changes in the local atomic structure and therefore in the Mn-C hybridization. The results in Fig. 7.4 show that the total magnetic moment increases/decreases only very slightly under tensile/compressive strain, remaining always localized on the Mn and neighboring C atoms.

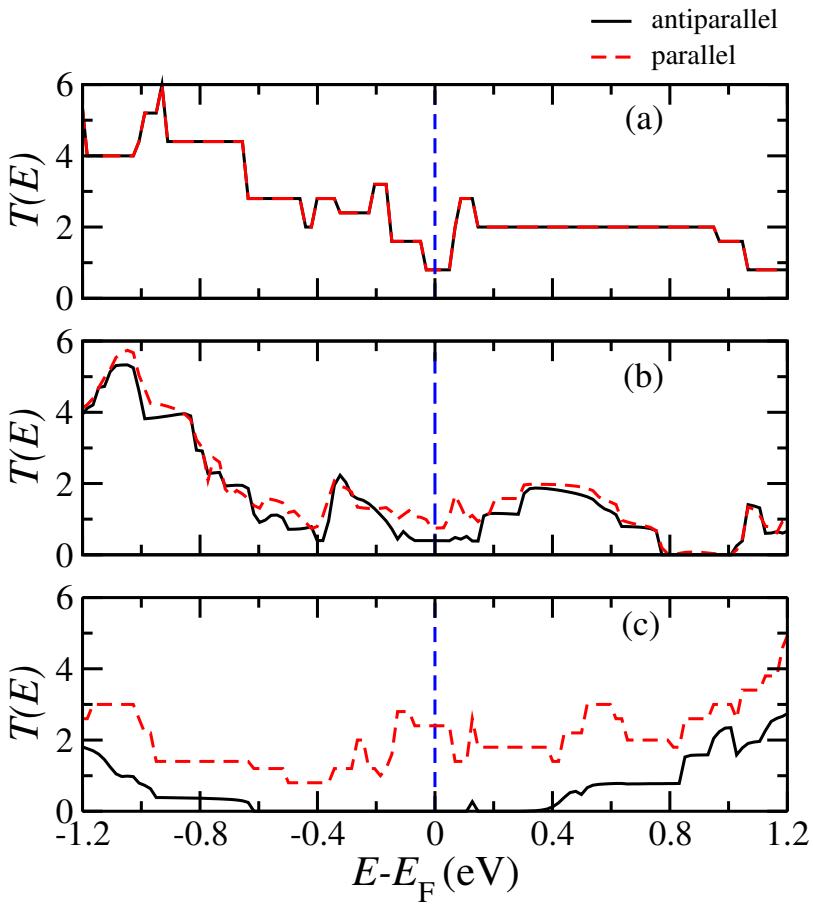

Figure 7.5: Transmission coefficient at zero bias for the (a) pristine, (b) 50% Mn-decorated, and (c) the 100% Mn-decorated line defect.

7.3 Spin-Polarized Transport Properties of Mn Decorated Line Defect

Due to the perturbation of the C electronic states and the induced magnetic moment, the transport properties of the line defect are strongly affected by the Mn decoration. The zero bias transmission coefficients for the (a) pristine, (b) 50% Mn-decorated, and (c) 100% Mn-decorated line defects are shown in Fig. 7.5. Figure 5(a) demonstrates degeneracy between parallel (P) and antiparallel (AP) alignments of the electrode magnetizations. The transport quantization is clearly visible (transport channels). According to Fig. 5(b), for 50% Mn coverage both the P and AP configurations

Table 7.2: Conductance and magnetoresistance at zero bias for various systems.

line defect	G_P (μS)	G_{AP} (μS)	MR (%)
pristine	0.62	0.62	–
50% Mn-decorated	0.55	0.29	47
100% Mn-decorated	2.40	10^{-11}	100

give rise to transmission around the Fermi energy, where the resistance is lower in the P configuration. This leads to a magnetoresistance of 47% at zero bias, see Table II. For 100% Mn coverage, see Fig. 5(c), the shorter Mn-Mn distance and enhanced interaction with the C host (transport path of ferromagnetically coupled atoms created; see above) results in a suppression of the transmission in the AP configuration and thus a magnetoresistance of 100%, see Table II.

Turning to the dependence of the magnetoresistance on the bias voltage, Figs. 7.6(a) and (b) demonstrate for the pristine and 50% Mn-decorated line defects essentially linear and almost identical IV characteristics for the P and AP configurations. On the contrary, for 100% Mn coverage we observe in Fig. 7.6(c) charging up to 0.1 eV (band gap in the minority spin channel) and thereafter a strongly suppressed I_{AP}, as expected from the above discussion. Under growing bias we find that I_{AP} continues to grow, whereas I_P quickly saturates. Therefore, the magnetoresistance is reduced to around 70% at $V = 0.4$ V.

7.4 Summary

In summary, we have demonstrated tunable spin dependent transport along a topological line defect in graphene by Mn decoration. Interestingly, the magnetic properties depend hardly on strain, which is important as strain typically cannot be avoided in exfoliated graphene. The transport properties turn out to vary strongly with the Mn

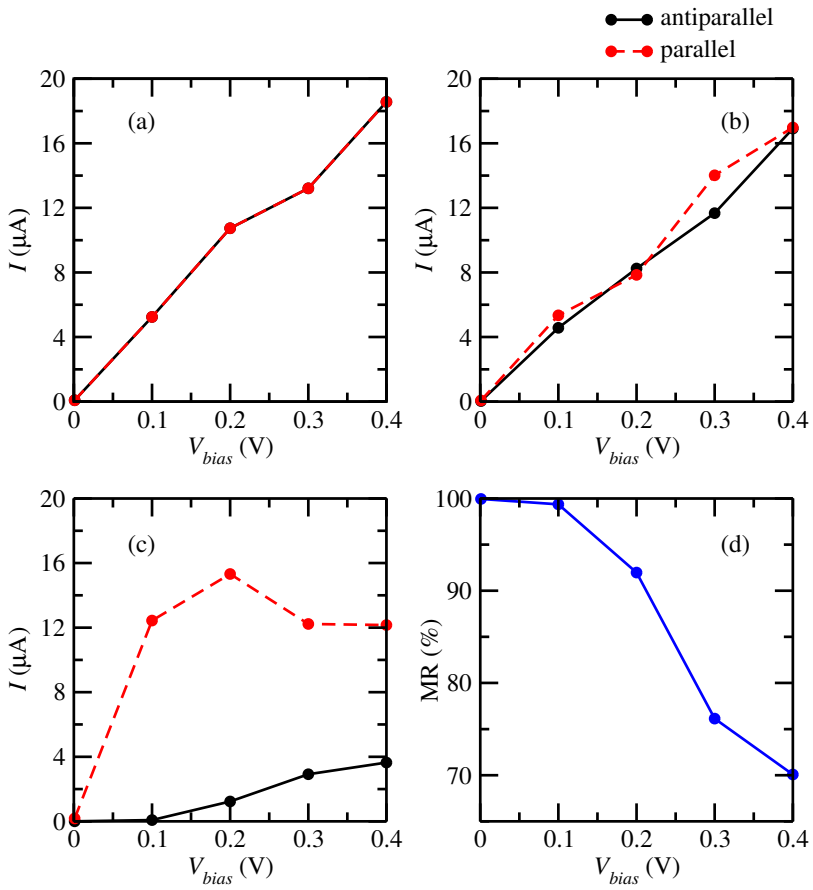

Figure 7.6: I-V characteristics for the P and AP configurations of the (a) pristine, (b) 50% Mn-decorated, and (c) 100% Mn-decorated line defect. (d) Magnetoresistance for case (c).

coverage. In particular, a magnetoresistance of 47% is obtained for 50% Mn coverage at zero bias, which grows to 100% when the line defect is completely decorated with Mn atoms. For bias voltages up to 0.4 V we obtain high values of the magnetoresistance for the 100% Mn-decorated line defect, which therefore has great potential from the application point of view.

Chapter 8

Conclusion and Outlook

Nanoscale organic and inorganic materials are vital components of next generation electronics. Rapid development of devices and applications requires the conventional silicon-based electronics (three-dimensional materials) to be replaced or modified by the novel low-dimensional materials. Despite the many appealing characteristic properties of these materials, fundamental understating of their microscopic properties need to be thoroughly investigated and established. This thesis focuses on exploiting the electronic and quantum transport properties of novel materials such as molecular switches and rectifiers with negative differential conductance and high rectification ratio. In addition, magnetoresistance and current-induced forces in graphene and carbon nanotubes have been studied.

Danilov and co workers [34] proposed a model switch comprising of oligophenylene-vinylene molecule sandwich between gold electrodes, whose bonding terminals are the thiol group. In their work, they proposed that switching this molecule from low to high conductance states requires the attachment of hydrogen atom to the thiol end group forming a thiolate, which can be reversibly switched by thermal agitation. Our study confirmed the existence of the two different conductance states, but disagrees on the switching mechanism. We have studied the switching behaviour of opv3, and

its protonated species (opv3H, and opv32H). In contrast to the results of Danilov, we found that opv3 conducts approximately an order of magnitude more than its protonated variants. It is worth nothing that our results are consistent regardless of whether LDA or ASIC is used and it demonstrated robustness against the choice of exchange and correlation functionals used. Note that the linear response results are carried onto finite bias up to 3 eV showing that opv3 conducts more than its protonated species. Moreover, the difference between the experimental [34] ON/OFF ratio is significantly lower than what we find under protonation. This is further evidence that the switching mechanism is not a protonation reaction. Further work is required to determine the actual switching mechanism. The potential areas of interest are reversible rearrangements of the bonding geometries of the thiol groups, rotation of the middle benzene ring, contact asymmetry.

To understand molecular junctions, the effect of current induced forces is required. Also, current induced forces provides insight on device degradation. Motivated by these needs, we carried out theoretical calculations within the framework of DFT and NEGF on SW defect in graphene, adatom on both graphene and carbon nanotubes. We find that the results strongly depend on the system, not being a ubiquitous consequence of the current. The barrier height for annealing of SW defect is found to be insensitive to the current, compared to C adatoms migration on graphene. This effect is due to the fact that the force components along the migration path vanishes irrespective of the large total force. However, the situation is very different for adatom migration on CNTs. Current induced forces reduces the migration barrier height substantially. Furthermore, we address the issue of the conservativeness of current induced forces. We showed for the first time using DFT that current induced forces could be non-conservative by considering the work done in a close path for the adatom migration on CNTs. This work can be extended to seek understanding of the

effect of current on the vibrational modes of the adatom. And also the general effect of current on the thermal coefficient.

Furthermore, we probed the directional effect of current on single molecules rectification. The dipyrimidinyl-diphenyl molecule and its derivatives in application for rectifiers. First, we investigated the roles of the acceptor and donor rings and the consequences when their ratio is changed. For this case, we found optimal rectification when the molecules consist of acceptors and donors in equal measures. We went further to show that a serial arrangement of two of the molecule (tandem configuration) improves rectification. Furthermore, we increased the asymmetry of the tandem configuration that gave enhanced rectification ratio. The inclusion of asymmetry of the tandem configuration is essential to optimized rectification ratio in this class of molecular junction.

We have functionalized boronitrene with carbon to produce current based effect such as the Negative differential conductance. First, we showed that the large band gap of BN can be tuned from insulating to semiconducting and further to metallic behavior by means of varying the shape and composition of the C defects introduced. In particular, we observe bias regions of NDC for specific defect configurations with high peak-to-valley ratios.

Finally, we demonstrated spin-dependent transport along a Mn-decorated topological line defect in graphene. These line defects have been observed experimentally. We found substantial preferential bonding of the Mn atoms at octagonal hollow sites of the line defect. This overcomes the problem associated with transition-metal atoms mobility on graphene. Equally, we found that the magnetic properties depend sparingly on stain, as strain typically cannot be avoided in exfoliated graphene. The spin-dependent transport properties turn out to vary strongly with the Mn coverage. In particular, we found that magnetoresistance behavior is a consequence of induced

strong π magnetism in the graphene host.

The work accomplished in this thesis can be extended in different aspects. Physical realization and experimental verification of the proposed devices can be carried out. This realization will open new frontiers and understanding towards the functionality of the proposed high rectification diodes and the switching devices as well as other interesting features like NDC and magnetoresistance. More work can be directed towards finding out the actual mechanism by which the opv3 molecule in the presence of gold electrodes switches. We suggest that the rotation of the middle phenyl ring be investigated, contact geometries should equally be explored. Other effects like the phonon contribution to transport properties needs to be exploited to further increase device longevity.

REFERENCES

[1] M. Ratner, "A brief history of molecular electronics," Nature Nanotechnology **8**, 378 (2013).

[2] T. Huang, J. Zhao, M. Feng, A. A. Popov, S. Yang, L. Dunsch, and H. Petek, "A Molecular Switch Based on Current-Driven Rotation of an Encapsulated Cluster within a Fullerene Cage," Nano Letters **11**, 5327 (2011).

[3] B. Capozzi, J. Xia, O. Adak, E. J. Dell, Z.-F. Liu, J. C. Taylor, J. B. Neaton, L. M. Campos, and L. Venkataraman, "Single-molecule diodes with high rectification ratios through environmental control," Nature Nanotechnology **10**, 522 (2015).

[4] J. C. Cuevas, "Single-molecule diodes: The environment does the trick," Nature Nanotechnology **10**, 486 (2015).

[5] N. Fuentes, A. Martín Lasanta, L. Álvarez de Cienfuegos, M. Ribagorda, A. Parra, and J. M. Cuerva, "Organic-based molecular switches for molecular electronics," Nanoscale **3**, 4003 (2011).

[6] S. V. Aradhya and L. Venkataraman, "Single-molecule junctions beyond electronic transport." Nature Nanotechnology **8**, 399 (2013).

[7] M. E. Gemayel, K. Börjesson, M. Herder, D. T. Duong, J. A. Hutchison, C. Ruzié, G. Schweicher, A. Salleo, Y. Geerts, S. Hecht, E. Orgiu, and P. Samorì, "Optically switchable transistors by simple incorporation of photochromic systems into small-molecule semiconducting matrices," Nature Communications **6**, 6330 (2015).

[8] J. Martínez Blanco, C. Nacci, S. C. Erwin, K. Kanisawa, E. Locane, M. Thomas, F. von Oppen, P. W. Brouwer, and S. Fölsch, "Gating a single-molecule transistor with individual atoms," Nature Physics **11**, 640 (2015).

[9] S. Y. Quek, M. Kamenetska, M. L. Steigerwald, H. J. Choi, S. G. Louie, M. S. Hybertsen, J. B. Neaton, and L. Venkataraman, "Mechanically controlled binary conductance switching of a single-molecule junction." Nature Nanotechnology **4**, 230 (2009).

[10] C. Bruot, J. Hihath, and N. Tao, "Mechanically controlled molecular orbital alignment in single molecule junctions," Nature Nanotechnology **7**, 35 (2011).

[11] P. Nirmalraj, D. Thompson, A. Molina Ontoria, M. Sousa, N. Martín, B. Gotsmann, and H. Riel, "Nanoelectrical analysis of single molecules and atomic-scale materials at the solid/liquid interface," Nature Materials **13**, 947 (2014).

[12] G. P. Lansbergen, R. Rahman, C. J. Wellard, I. Woo, J. Caro, N. Collaert, S. Biesemans, G. Klimeck, L. C. L. Hollenberg, and S. Rogge, "Gate-induced quantum-confinement transition of a single dopant atom in a siliconFinFET," Nature Physics **4**, 656 (2008).

[13] J. T. Obodo, M. U. Kahaly, and U. Schwingenschlögl, "Magnetoresistance of Mn-decorated topological line defects in graphene," Physical Review B **91**, 014413 (2015).

[14] N. M. Caffrey, T. Archer, I. Rungger, and S. Sanvito, "Prediction of large bias-dependent magnetoresistance in all-oxide magnetic tunnel junctions with a ferroelectric barrier," Physical Review B **83**, 125409 (2011).

[15] J. Mathon and A. Umerski, "Theory of tunneling magnetoresistance of an epitaxial Fe/MgO/Fe(001) junction," Physical Review B **63**, 220403 (2001).

[16] S. Peng, Y. Zhang, M. Wang, Y. Zhang, and W. Zhao, "Magnetic Tunnel Junctions for Spintronics: Principles and Applications," in *Wiley Encyclopedia of Electrical and Electronics Engineering*, Vol. 1936 (John Wiley & Sons, Inc., Hoboken, NJ, USA, 2014) pp. 1–16.

[17] Z. Qian, R. Li, X. Zhao, S. Hou, and S. Sanvito, "Conceptual molecular quantum phase transistor based on first-principles quantum transport calculations," Physical Review B **78**, 2 (2008).

[18] D. Dundas, E. J. McEniry, and T. N. Todorov, "Current-driven atomic waterwheels." Nature nanotechnology **4**, 99 (2009).

[19] M. Brandbyge, "Computational nanoscience: Atomic waterwheels go to work," Nature Nanotechnology **4**, 81 (2009).

[20] M. A. Reed, "Conductance of a Molecular Junction," Science **278**, 252 (1997).

[21] H. Park, A. K. L. Lim, A. P. Alivisatos, J. Park, and P. L. McEuen, "Fabrication of metallic electrodes with nanometer separation by electromigration," Applied Physics Letters **75**, 301 (1999).

[22] A. F. Morpurgo, C. M. Marcus, and D. B. Robinson, "Controlled fabrication of metallic electrodes with atomic separation," Applied Physics Letters **74**, 2084 (1999).

[23] X. D. Cui, "Reproducible Measurement of Single-Molecule Conductivity," Science **294**, 571 (2001).

[24] S. R. Nicewarner Pena, R. Freeman Griffith, B. D. Reiss, L. He, D. J. Pena, I. D. Walton, R. Cromer, C. D. Keating, and M. J. Natan, "Submicrometer Metallic Barcodes," Science **294**, 137 (2001).

[25] A. Bezryadin, C. Dekker, and G. Schmid, "Electrostatic trapping of single conducting nanoparticles between nanoelectrodes," Applied Physics Letters **71**, 1273 (1997).

[26] L. Qin, "On-Wire Lithography," Science **309**, 113 (2005).

[27] M. Brink, "Letters To Nature," Nature **417**, 725 (2002).

[28] H. Yu, Y. Luo, K. Beverly, J. F. Stoddart, H. R. Tseng, and J. R. Heath, "The Molecule-Electrode Interface in Single-Molecule Transistors," Angewandte Chemie - International Edition **42**, 5706 (2003).

[29] H. S. J. van der Zant, Y.-V. Kervennic, M. Poot, K. ONeill, Z. de Groot, J. M. Thijssen, H. B. Heersche, N. Stuhr Hansen, T. Bjørnholm, D. Vanmaekelbergh, C. A. van Walree, and L. W. Jenneskens, "Molecular three-terminal devices: fabrication and measurements," Faraday Discussions **131**, 347 (2006).

[30] S. Jan van der Molen and P. Liljeroth, "Charge transport through molecular switches," Journal of Physics: Condensed Matter **22**, 133001 (2010).

[31] T. Sendler, K. Luka Guth, M. Wieser, Lokamani, J. Wolf, M. Helm, S. Gemming, J. Kerbusch, E. Scheer, T. Huhn, and A. Erbe, "Light-Induced Switching of Tunable Single-Molecule Junctions," Advanced Science **2**, 1500017 (2015).

[32] Z.-Q. Fan, Z.-H. Zhang, F. Xie, X.-Q. Deng, G.-P. Tang, C.-H. Yang, and K.-Q. Chen, "Reversible switching in gold-atomorganic-molecule complex induced by reversible bond formation," Organic Electronics **18**, 101 (2015).

[33] M. Baghernejad, X. Zhao, K. Baruël Ørnsø, M. Füeg, P. Moreno García, A. V. Rudnev, V. Kaliginedi, S. Vesztergom, C. Huang, W. Hong, P. Broekmann, T. Wandlowski, K. S. Thygesen, and M. R. Bryce, "Electrochemical Control of Single-Molecule Conductance by Fermi-Level Tuning and Conjugation Switching," Journal of the American Chemical Society **136**, 17922 (2014).

[34] A. V. Danilov, S. E. Kubatkin, S. G. Kafanov, K. Flensberg, and T. Bjørnholm, "Electron transfer dynamics of bistable single-molecule junctions." Nano Letters **6**, 2184 (2006).

[35] J. T. Obodo, K. Gkionis, I. Rungger, S. Sanvito, and U. Schwingenschlögl, "Hydrogen bonding as the origin of the switching behavior in dithiolated phenylene-vinylene oligomers," Physical Review B **88**, 085438 (2013).

[36] F. Niroui, A. I. Wang, E. M. Sletten, Y. Song, J. Kong, E. Yablonovitch, T. M. Swager, J. H. Lang, and V. Bulović, "Tunneling Nanoelectromechanical Switches Based on Compressible Molecular Thin Films," ACS Nano **9**, 7886 (2015).

[37] T. J. W. Wagner and D. Vella, "Switch on, switch off: stiction in nanoelectromechanical switches," Nanotechnology **24**, 275501 (2013).

[38] Z. Yang, M. Chshiev, M. Zwolak, Y. Chen, and M. Di Ventra, "Role of heating and current-induced forces in the stability of atomic wires," Physical Review B **71**, 041402(R) (2005).

[39] T. N. Todorov, D. Dundas, and E. J. McEniry, "Nonconservative generalized current-induced forces," Physical Review B **81**, 075416 (2010).

[40] J.-T. Lü, T. Gunst, P. Hedegård, and M. Brandbyge, "Current-induced dynamics in carbon atomic contacts," Beilstein Journal of Nanotechnology **2**, 814 (2011).

[41] B. C. Hsu, I. Amanatidis, W.-l. Liu, A. Tseng, and Y.-c. Chen, "Effects of Current-Induced Forces on Pt-Benzene-Pt Single-Molecule Junctions," The Journal of Physical Chemistry C **118**, 2245 (2014).

[42] D. Sheppard, R. Terrell, and G. Henkelman, "Optimization methods for finding minimum energy paths," The Journal of Chemical Physics **128**, 134106 (2008).

[43] V. Mujica, M. A. Ratner, and A. Nitzan, "Molecular rectification: why is it so rare?" Chemical Physics **281**, 147 (2002).

[44] C. Van Dyck and M. A. Ratner, "Molecular Rectifiers: A New Design Based on Asymmetric Anchoring Moieties," Nano Letters **15**, 1577 (2015).

[45] A. Aviram and M. Ratner, "Molecular rectifiers," Chemical Physics Letters **29**, 277 (1974).

[46] H. Liu, N. Wang, P. Li, X. Yin, C. Yu, N. Gao, and J. Zhao, "Theoretical investigation into molecular diodes integrated in series using the non-equilibrium Green's function method." Physical Chemistry Chemical Physics: PCCP **13**, 1301 (2011).

[47] T. Kim, Z.-F. Liu, C. Lee, J. B. Neaton, and L. Venkataraman, "Charge transport and rectification in molecular junctions formed with carbon-based electrodes." Proceedings of the National Academy of Sciences of the United States of America **111**, 10928 (2014).

[48] L. Yuan, N. Nerngchamnong, L. Cao, H. Hamoudi, E. del Barco, M. Roemer, R. K. Sriramula, D. Thompson, and C. A. Nijhuis, "Controlling the direction of rectification in a molecular diode," Nature Communications **6**, 6324 (2015).

[49] Z. Yang, Y.-L. Ji, G. Lan, L.-C. Xu, X. Liu, and B. Xu, "Design molecular rectifier and photodetector with all-boron fullerene," Solid State Communications **217**, 38 (2015).

[50] M. L. Perrin, E. Galan, R. Eelkema, F. Grozema, J. M. Thijssen, and H. S. J. van der Zant, "Single-Molecule Resonant Tunneling Diode," The Journal of Physical Chemistry C **119**, 5697 (2015).

[51] K. Wang, J. Zhou, J. M. Hamill, and B. Xu, "Measurement and understanding of single-molecule break junction rectification caused by asymmetric contacts," Journal of Chemical Physics **141**, 054712 (2014).

[52] W.-H. Zhu, G.-H. Ding, and B. Dong, "Negative differential conductance and hysteretic current switching of benzene molecular junction in a transverse electric field," Nanotechnology **25**, 465202 (2014).

[53] P. Zhao, D. S. Liu, H. Y. Liu, S. J. Li, and G. Chen, "Low bias negative differential resistance in C60 dimer modulated by gate voltage," Organic Electronics: physics, materials, applications **14**, 1109 (2013).

[54] J. Zhou, S. Samanta, C. Guo, J. Locklin, and B. Xu, "Measurements of contact specific low-bias negative differential resistance of single metalorganic molecular junctions," Nanoscale **5**, 5715 (2013).

[55] S. A. Wolf, "Spintronics: A Spin-Based Electronics Vision for the Future," Science **294**, 1488 (2001).

[56] J.-J. Li, M.-L. Bai, Z.-B. Chen, X.-S. Zhou, Z. Shi, M. Zhang, S.-Y. Ding, S.-M. Hou, W. Schwarzacher, R. J. Nichols, and B.-W. Mao, "Giant Single-Molecule Anisotropic Magnetoresistance at Room Temperature," Journal of the American Chemical Society **137**, 5923 (2015).

[57] R. N. Mahato, H. Lulf, M. H. Siekman, S. P. Kersten, P. A. Bobbert, M. P. de Jong, L. De Cola, and W. G. van der Wiel, "Ultrahigh Magnetoresistance at Room Temperature in Molecular Wires," Science **341**, 257 (2013).

[58] C.-H. Hsu, Y.-H. Chu, C.-I. Lu, P.-J. Hsu, S.-W. Chen, W.-J. Hsueh, C.-C. Kaun, and M.-T. Lin, "Spin-Polarized Transport through Single Manganese Phthalocyanine Molecules on a Co Nanoisland," The Journal of Physical Chemistry C **119**, 3374 (2015).

[59] R. M. Martin, *Electronic Structure, Basic Theory and Practical Methods* (Cambridge University Press, 2004).

[60] M. Born and J. R. Oppenheimer, "Zur quantentheorie der molekeln," Annalen der Physik **84** (1927).

[61] W. Kohn and L. J. Sham, "Self-Consistent Equations Including Exchange and Correlation Effects," Physical Review **140**, A1133 (1965).

[62] A. Dario, *First Principles Study of Two Rhodium Surfaces upon Carbon Monoxide and Oxygen Adsorption*, Ph.D. thesis, Scuola Internazionale Superiore di Studi Avanzati - SISSA (1997).

[63] R. O. Jones and O. Gunnarsson, "The density functional formalism, its applications and prospects," Reviews of Modern Physics **61**, 689 (1989).

[64] K. O. Obodo, *Quantum Mechanical Studies of the Early Actinide Compounds*, Ph.D. thesis, University of Pretoria, Pretoria, South Africa (2014).

[65] A. D. Becke, "Density-functional exchange-energy approximation with correct asymptotic behavior," Physical Review A **38**, 3098 (1988).

[66] J. P. Perdew and Y. Wang, "Accurate and simple analytic representation of the electron-gas correlation energy," Physical Review B **45**, 13244 (1992).

[67] J. P. Perdew, K. Burke, and M. Ernzerhof, "Generalized Gradient Approximation Made Simple," Physical Review Letters **77**, 3865 (1996).

[68] J. P. Perdew and A. Zunger, "Self-interaction correction to density-functional approximations for many-electron systems," Physical Review B **23**, 5048 (1981).

[69] C. D. Pemmaraju, T. Archer, D. Sánchez-Portal, and S. Sanvito, "Atomic-orbital-based approximate self-interaction correction scheme for molecules and solids," Physical Review B **75** (2007).

[70] A. Filippetti and N. A. Spaldin, "Self-interaction-corrected pseudopotential scheme for magnetic and strongly-correlated systems," Physical Review B **67**, 1251091 (2003).

[71] D. Vogel, P. Krüger, and J. Pollmann, "Self-interaction and relaxation-corrected pseudopotentials for ii-vi semiconductors," Physical Review B **54**, 5495 (1996).

[72] C. Toher and S. Sanvito, "Efficient atomic self-interaction correction scheme for nonequilibrium quantum transport," Physical Review Letters **99**, 056801 (2007).

[73] S. Power and M. Ferreira, "Indirect Exchange and RudermanKittelKasuyaYosida (RKKY) Interactions in Magnetically-Doped Graphene," Crystals **3**, 49 (2013).

[74] M. Sherafati and S. Satpathy, "RKKY interaction in graphene from the lattice Greens function," Physical Review B **83**, 165425 (2011).

[75] P. D. Gorman, J. M. Duffy, M. S. Ferreira, and S. R. Power, "RKKY interaction between adsorbed magnetic impurities in graphene: Symmetry and strain effects," Physical Review B **88**, 085405 (2013).

[76] A. R. Rocha, V. M. García Suárez, S. W. Bailey, C. J. Lambert, J. Ferrer, and S. Sanvito, "Towards molecular spintronics." Nature materials **4**, 335 (2005).

[77] A. R. Rocha, V. M. García Suárez, S. Bailey, C. Lambert, J. Ferrer, and S. Sanvito, "Spin and molecular electronics in atomically generated orbital landscapes," Physical Review B **73**, 085414 (2006).

[78] R. Alexandra, *Theoretical and computational aspects of electronic transport at the nanoscale*, Ph.D. thesis, Trinity College Dublin, Ireland (2005).

[79] M. Büttiker, Y. Imry, R. Landauer, and S. Pinhas, "Generalized many-channel conductance formula with application to small rings," Physical Review B **31**, 6207 (1985).

[80] M. Brandbyge, J.-L. Mozos, P. Ordejón, J. Taylor, and K. Stokbro, "Density-functional method for nonequilibrium electron transport," Physical Review B **65**, 165401 (2002).

[81] J. Taylor, H. Guo, and J. Wang, "Ab initio modeling of quantum transport properties of molecular electronic devices," Physical Review B **63**, 245407 (2001).

[82] A. Pecchia and A. D. Carlo, "Atomistic theory of transport in organic and inorganic nanostructures," Reports on Progress in Physics **67**, 1497 (2004).

[83] E. N. Economou, *Green's Functions in Quantum Physics* (Spinger-Verlag, Berlin, 1995).

[84] S. Datta, *Electronic Transport in Mesoscopic Systems* (Cambridge University Press, Cambridge, UK, 2003).

[85] M. Paulsson and M. Brandbyge, "Transmission eigenchannels from nonequilibrium Green's functions," Physical Review B **76**, 1 (2007).

[86] H. W. Fink and C. Schonenberger, "Electrical conduction through DNA molecules," in *Advanced Semiconductors and Organic Nano-Techniques*, Vol. 398, edited by H. Morkoc (Academic Press, 2003) pp. 407–410.

[87] S. Sanvito, C. J. Lambert, J. H. Jefferson, and A. M. Bratkovsky, "General Greens-function formalism for transport calculations with spd Hamiltonians and giant magnetoresistance in Co- and Ni-based magnetic multilayers," Physical Review B **59**, 11936 (1999).

[88] Y. Meir and N. S. Wingreen, "Landauer formula for the current through an interacting electron region," Physical Review Letters **68**, 2512 (1992).

[89] W. Quapp and J. M. Bofill, "Letter to the editor: A comment to the nudged elastic band method," Journal of Computational Chemistry **31**, 2526 (2010).

[90] G. Henkelman, B. P. Uberuaga, and H. Jónsson, "Climbing image nudged elastic band method for finding saddle points and minimum energy paths," Journal of Chemical Physics **113**, 9901 (2000).

[91] M. Hauder, J. Gstöttner, W. Hansch, and D. Schmitt-Landsiedel, "Scaling properties and electromigration resistance of sputtered Ag metallization lines," Applied Physics Letters **78**, 838 (2001).

[92] R. Landauer and J. W. F. Woo, "Driving force in electromigration," Physical Review B **10**, 1266 (1974).

[93] A. K. Das and R. Peierls, "The force of electromigration," Journal of Physics C **8**, 3348 (1975).

[94] L. J. Sham, "Microscopic theory of the driving force in electromigration," Physical Review B **12**, 3142 (1975).

[95] R. S. Sorbello, *Theory of Electromigration*, Solid State Physics - Advances in Research and Applications, Vol. 51 (Academic Press, San Diego, 1997) pp. 159–231.

[96] M. Di Ventra and S. T. Pantelides, "Hellmann-Feynman theorem and the definition of forces in quantum time-dependent and transport problems," Physical Review B **61**, 16207 (2000).

[97] R. Zhang, I. Rungger, S. Sanvito, and S. Hou, "Current-induced energy barrier suppression for electromigration from first principles," Physical Review B **84** (2011).

[98] M. Brandbyge, K. Stokbro, J. Taylor, J.-L. Mozos, and P. Ordejon, "Origin Of Current-Induced Forces In An Atomic Gold Wire: A First Principles Study," Physical Review B **67**, 193104 (2002).

[99] M. Di Ventra, *Electrical Transport in Nanoscale Systems* (Cambridge University Press, Cambridge, 2008) p. 496.

[100] M. Di Ventra, Y.-C. Chen, and T. N. Todorov, "Are Current-Induced Forces Conservative?" Physical Review Letters **92**, 176803 (2004).

[101] T. N. Todorov, J. Hoekstra, and A. P. Sutton, "Current-induced forces in atomic-scale conductors," Philosophical Magazine Part B **80**, 421 (2000).

[102] T. Rakshit, G.-C. Liang, A. W. Ghosh, and S. Datta, "Silicon-based Molecular Electronics," Nano Letters **4**, 1803 (2004).

[103] S. Y. Quek, J. B. Neaton, M. S. Hybertsen, E. Kaxiras, and S. G. Louie, "Negative Differential Resistance in Transport through Organic Molecules on Silicon," Physical Review Letters **98**, 066807 (2007).

[104] M. L. Perrin, R. Frisenda, M. Koole, J. S. Seldenthuis, J. A. C. Gil, H. Valkenier, J. C. Hummelen, N. Renaud, F. C. Grozema, J. M. Thijssen, D. Dulić, and H. S. J. van der Zant, "Large negative differential conductance in single-molecule break junctions," Nature Nanotechnology **9**, 830 (2014).

[105] J. Chen, "Large On-Off Ratios and Negative Differential Resistance in a Molecular Electronic Device," Science **286**, 1550 (1999).

[106] B. Xu and Y. Dubi, "Negative differential conductance in molecular junctions: an overview of experiment and theory," Journal of Physics: Condensed Matter **27**, 263202 (2015).

[107] X.-F. Li, K.-Y. Lian, Q. Qiu, and Y. Luo, "Half-filled energy bands induced negative differential resistance in nitrogen-doped graphene," Nanoscale **7**, 4156 (2015).

[108] F. Chen and N. J. Tao, "Electron transport in single molecules: from benzene to graphene," Accounts of Chemical Research **42**, 429 (2009).

[109] N. J. Tao, "Electron transport in molecular junctions." Nature nanotechnology **1**, 173 (2006).

[110] L. Vitali, S. Fabris, A. M. Conte, S. Brink, M. Ruben, S. Baroni, and K. Kern, "Electronic Structure of Surface-supported Bis(phthalocyaninato) terbium(III) Single Molecular Magnets," Nano Letters **8**, 3364 (2008).

[111] J. S. Miller, D. Gatteschi, and S. Sanvito, "Molecule-based magnets themed issue Molecular spintronicsw," Chemical Society Reviews **40**, 3336 (2011).

[112] J. Repp, G. Meyer, F. E. Olsson, and M. Persson, "Controlling the charge state of individual gold adatoms." Science **305**, 493 (2004).

[113] E. G. Emberly and G. Kirczenow, "The smallest molecular switch," Physical Review Letters **91**, 188301 (2003).

[114] A. C. Whalley, M. L. Steigerwald, X. Guo, and C. Nuckolls, "Reversible switching in molecular electronic devices," Journal of the American Chemical Society **129**, 12590 (2007).

[115] S. Ishihara, J. P. Hill, A. Shundo, G. J. Richards, J. Labuta, K. Ohkubo, S. Fukuzumi, A. Sato, M. R. J. Elsegood, S. J. Teat, and K. Ariga, "Reversible photoredox switching of porphyrin-bridged bis-2,6-di- tert -butylphenols," Journal of the American Chemical Society **133**, 16119 (2011).

[116] C. M. Guédon, H. Valkenier, T. Markussen, K. S. Thygesen, J. C. Hummelen, and S. J. van der Molen, "Observation of quantum interference in molecular charge transport," Nature Nanotechnology **7**, 305 (2012).

[117] I. W. Lyo and P. Avouris, "Negative differential resistance on the atomic scale: implications for atomic scale devices." Science **245**, 1369 (1989).

[118] R. B. Pontes, A. R. Rocha, S. Sanvito, A. Fazzio, and A. R. da Silva, "Ab Initio Calculations of Structural Evolution and Conductance of Benzene-1,4-dithiol on Gold Leads," ACS Nano **5**, 795 (2011).

[119] L. Venkataraman, J. E. Klare, I. W. Tam, C. Nuckolls, M. S. Hybertsen, and M. L. Steigerwald, "Single-Molecule Circuits with Well-Defined Molecular Conductance," Nano Letters **6**, 458 (2006).

[120] G. Rozenberg, T. Bäck, and J. Kok, *Handbook of Natural Computing* (Springer-Verlag, Berlin, 2012).

[121] J. Kong, "Nanotube Molecular Wires as Chemical Sensors," Science **287**, 622 (2000).

[122] C. P. Collier, G. Mattersteig, E. W. Wong, Y. Luo, K. Beverly, J. Sampaio, F. M. Raymo, J. F. Stoddart, and J. R. Heath, "A [2]catenane-based solid state electronically reconfigurable switch," Science **289**, 1172 (2000).

[123] Z. J. Donhauser, B. A. Mantooth, K. F. Kelly, L. A. Bumm, J. D. Monnell, J. J. Stapleton, D. W. Price Jr, A. M. Rawlett, D. L. Allara, J. M. Tour, and P. S. Weiss, "Conductance switching in single molecules through conformational changes," Science **292**, 2303 (2001).

[124] D. Dulić, S. J. van der Molen, T. Kudernac, H. T. Jonkman, J. J. D. de Jong, T. N. Bowden, J. van Esch, B. L. Feringa, and B. J. van Wees, "One-way optoelectronic switching of photochromic molecules on gold," Physical Review Letters **91**, 207402 (2003).

[125] A. Odell, A. Delin, B. Johansson, I. Rungger, and S. Sanvito, "Investigation of the conducting properties of a photoswitching dithienylethene molecule," ACS Nano **4**, 2635 (2010).

[126] J. M. Tour, "Conjugated Macromolecules of Precise Length and Constitution. Organic Synthesis for the Construction of Nanoarchitectures," Chemical Reviews **96**, 537 (1996).

[127] F. Jiang, Y. X. Zhou, H. Chen, R. Note, H. Mizuseki, and Y. Kawazoe, "First-principles study of phenyl ethylene oligomers as current-switch," Physics Letters, Section A: General, Atomic and Solid State Physics **359**, 487 (2006).

[128] C. Toher and S. Sanvito, "Effects of self-interaction corrections on the transport properties of phenyl-based molecular junctions," Physical Review B **77**, 155402 (2008).

[129] J. M. Soler, E. Artacho, J. D. Gale, A. Garc, J. Junquera, P. Ordej, S. Daniel, A. García, J. Junquera, P. Ordejón, and D. Sànchez Portal, "The SIESTA method for ab initio order-N materials," Journal of Physics **2745**, 2745 (2002).

[130] J. Junquera, O. Paz, D. Sanchez Portal, E. Artacho, D. Sánchez Portal, and E. Artacho, "Numerical atomic orbitals for linear scaling," Physical Review B **64**, 235111 (2001).

[131] N. Troullier and J. L. Martins, "Efficient pseudopotentials for plane-wave calculations. II. Operators for fast iterative diagonalization," Physical Review B **43**, 8861 (1991).

[132] L. Kleinman and D. M. Bylander, "Efficacious form for model pseudopotentials," Physical Review Letters **48**, 1425 (1982).

[133] D. M. Ceperley and B. J. Alder, "Ground state of the electron gas by a stochastic method," Physical Review Letters **45**, 566 (1980).

[134] A. Filippetti, C. D. Pemmaraju, S. Sanvito, P. Delugas, D. Puggioni, and V. Fiorentini, "Variational pseudo-self-interaction-corrected density functional approach to the ab initio description of correlated solids and molecules," Physical Review B **84**, 195127 (2011).

[135] C. S. Cucinotta, I. Rungger, and S. Sanvito, "First Principles Study of Electron Tunneling through Ice," The Journal of Physical Chemistry C **116**, 22129 (2012).

[136] H. Sellers, A. Ulman, Y. Shnidman, and J. E. Eilers, "Structure and binding of alkanethiolates on gold and silver surfaces: Implications for self-assembled monolayers," Journal of the American Chemical Society **115**, 9389 (1993).

[137] H. Grönbeck, A. Curioni, and W. Andreoni, "Thiols and Disulfides on the Au(111) Surface: The HeadgroupGold Interaction," Journal of the American Chemical Society **122**, 3839 (2000).

[138] S. N. Yaliraki, A. E. Roitberg, C. Gonzalez, V. Mujica, and M. A. Ratner, "The injecting energy at molecule/metal interfaces: Implications for conductance of molecular junctions from an ab initio molecular description," Journal of Chemical Physics **111**, 6997 (1999).

[139] I. Rungger, X. Chen, U. Schwingenschlögl, and S. Sanvito, "Finite-bias electronic transport of molecules in a water solution," Physical Review B **81**, 235407 (2010).

[140] A. K. Mahler, H. Schlick, R. Saf, F. Stelzer, F. Meghdadi, A. Pogantsch, G. Leising, K.-C. Möller, and J. O. Besenhard, "Blue-Green Light Emitting Poly(phenylenevinylene) Derivatives as Candidates for Polymer LEDs: Synthesis and Characterization," Macromolecular Chemistry and Physics **205**, 1840 (2004).

[141] J. B. Neaton, M. S. Hybertsen, and S. G. Louie, "Renormalization of Molecular Electronic Levels at Metal-Molecule Interfaces," Physical Review Letters **97**, 216405 (2006).

[142] C. Toher, I. Rungger, and S. Sanvito, "Simulating STM transport in alkanes from first principles," Physical Review B **79**, 205427 (2009).

[143] A. Danilov, S. Kubatkin, S. Kafanov, P. Hedegård, N. Stuhr Hansen, K. Moth Poulsen, and T. Bjørnholm, "Electronic transport in single molecule junctions: control of the molecule-electrode coupling through intramolecular tunneling barriers," Nano Letters **8**, 1 (2008).

[144] C. D. Pemmaraju, I. Rungger, and S. Sanvito, "Ab initio calculation of the bias-dependent transport properties of Mn 12 molecules," Physical Review B **80**, 104422 (2009).

[145] R. Landauer, "Spatial carrier density modulation effects in metallic conductivity," Physical Review B **14**, 1474 (1976).

[146] R. S. Sorbello and B. B. Dasgupta, "Force on an atom in an electrostatic field: Feynman-Hellmann theorem and oscillator strengths," Physical Review B **21**, 2196 (1980).

[147] I. Valov, E. Linn, S. Tappertzhofen, S. Schmelzer, J. van den Hurk, F. Lentz, and R. Waser, "Nanobatteries in redox-based resistive switches require extension of memristor theory," Nature Communications **4**, 1771 (2013).

[148] R. Zhang, I. Rungger, S. Sanvito, and S. Hou, "Current-induced energy barrier suppression for electromigration from first principles," Physical Review B **84**, 085445 (2011).

[149] N. Agraït, C. Untiedt, G. Rubio Bollinger, S. Vieira, N. Agraït, C. Untiedt, G. Rubio Bollinger, and S. Vieira, "Onset of energy dissipation in ballistic atomic wires," Physical Review Letters **88**, 216801 (2002).

[150] Y.-C. Chen, M. Zwolak, and M. Di Ventra, "Theory of local heating in nanoscale conductors," Nano Letters **3**, 4 (2003).

[151] Z. Ioffe, T. Shamai, A. Ophir, G. Noy, I. Yutsis, K. Kfir, O. Cheshnovsky, and Y. Selzer, "Detection of heating in current-carrying molecular junctions by Raman scattering," Nature Nanotechnology **3**, 727 (2008).

[152] Z. Huang, F. Chen, R. D'Agosta, P. A. Bennett, M. Di Ventra, and N. Tao, "Local ionic and electron heating in single-molecule junctions," Nature Nanotechnology **2**, 698 (2007).

[153] A. K. Geim and K. S. Novoselov, "The rise of graphene," Nature Materials **6**, 183 (2007).

[154] A. H. Castro Neto, F. Guinea, N. M. R. Peres, K. S. Novoselov, and a. K. Geim, "The electronic properties of graphene," Reviews of Modern Physics **81**, 109 (2009).

[155] A. Murat, I. Rungger, C. Jin, S. Sanvito, and U. Schwingenschlögl, "Origin of the p-Type Character of AuCl 3 Functionalized Carbon Nanotubes," The Journal of Physical Chemistry C **118**, 3319 (2014).

[156] S. J. Tans, A. R. M. Verschueren, and C. Dekker, "Room-temperature transistor based on a single carbon nanotube," Nature **393**, 49 (1998).

[157] C. Zhou, J. Kong, E. Yenilmez, and H. Dai, "Modulated chemical doping of individual carbon nanotubes," Science **290**, 1552 (2000).

[158] Q. M. Ramasse, R. Zan, U. Bangert, D. W. Boukhvalov, Y.-W. Son, and K. S. Novoselov, "Direct Experimental Evidence of Metal-Mediated Etching of Suspended Graphene," ACS Nano **6**, 4063 (2012).

[159] A. W. Robertson, B. Montanari, K. He, J. Kim, C. S. Allen, Y. A. Wu, J. Olivier, J. Neethling, N. Harrison, A. I. Kirkland, and J. H. Warner, "Dynamics of single Fe atoms in graphene vacancies," Nano Letters **13**, 1468 (2013).

[160] D. Solenov and K. A. Velizhanin, "Adsorbate transport on graphene by electromigration," Physical Review Letters **109**, 95504 (2012).

[161] M. Löffler, U. Weissker, T. Mühl, T. Gemming, J. Eckert, and B. Büchner, "Current-Induced Mass Transport in Filled Multiwalled Carbon Nanotubes," Advanced Materials **23**, 541 (2011).

[162] J. Chen, T. Shi, T. Cai, T. Xu, L. Sun, X. Wu, and D. Yu, "Self healing of defected graphene," Applied Physics Letters **102** (2013).

[163] L. Liu, Z. Chen, L. Wang, E. Polyakova, T. Taniguchi, K. Watanabe, J. Hone, G. W. Flynn, and L. E. Brus, "Slow gold adatom diffusion on graphene: Effect of silicon dioxide and hexagonal boron nitride substrates," Journal of Physical Chemistry B **117**, 4305 (2013).

[164] T. P. Hardcastle, C. R. Seabourne, R. Zan, R. M. D. Brydson, U. Bangert, Q. M. Ramasse, K. S. Novoselov, and A. J. Scott, "Mobile metal adatoms on single layer, bilayer, and trilayer graphene: An ab initio DFT study with van der Waals corrections correlated with electron microscopy data," Physical Review B **87**, 195430 (2013).

[165] A. Barreiro, R. Rurali, E. R. Hernndez, and A. Bachtold, "Structured graphene devices for mass transport," Small **7**, 775 (2011).

[166] C. Jin, K. Suenaga, and S. Iijima, "Vacancy migrations in carbon nanotubes," Nano Letters **8**, 1127 (2008).

[167] H. Jónsson, G. Mills, and K. W. Jacobsen, "Nudged elastic band method for finding minimum energy paths of transitions," in *Classical and Quantum Dynamics in Condensed Phase Simulations*, edited by G. C. B. J. Berne and D. F. Coker (World Scientific, 1998) pp. 385–404.

[168] G. Mills and H. Jónsson, "Quantum and thermal effects in H2 dissociative adsorption: Evaluation of free energy barriers in multidimensional quantum systems," Physical Review Letters **72**, 1124 (1994).

[169] G. Mills and H. Jonsson, "Reversible Work Transiton State Theory: Application to Dissociative Adsorption of Hydrogen," Surface Science **324**, 42 (1994).

[170] I. Rungger and S. Sanvito, "Algorithm for the construction of self-energies for electronic transport calculations based on singularity elimination and singular value decomposition," Physical Review B **78**, 035407 (2008).

[171] D. Sánchez Portal, P. Ordejón, E. Artacho, J. M. Soler, D. Sanchez Poral, P. Ordejon, E. Artacho, and J. M. Soler, "Density-Functional Method for Very Large Systems with LCAO Basis Sets," International Journal **65**, 453 (1997).

[172] T. N. Todorov, "Time-dependent tight binding," Journal of Physics: Condensed Matter **13**, 10125 (2001).

[173] T. N. Todorov, D. Dundas, J.-T. Lü, M. Brandbyge, and P. Hedegård, "Current-induced forces: A simple derivation," European Journal of Physics **35**, 065004 (2014).

[174] N. Bode, S. V. Kusminskiy, R. Egger, and F. von Oppen, "Current-induced forces in mesoscopic systems: A scattering-matrix approach," Beilstein Journal of Nanotechnology **3**, 144 (2012).

[175] T. Ohto, I. Rungger, K. Yamashita, H. Nakamura, and S. Sanvito, "Ab initio theory for current-induced molecular switching: Melamine on Cu(001)," Physical Review B **87**, 205439 (2013).

[176] G. Henkelman, B. P. Uberuaga, and H. Jónsson, "Climbing image nudged elastic band method for finding saddle points and minimum energy paths," Journal of Chemical Physics **113**, 9901 (2000).

[177] Y. Lin and J. W. Connell, "Advances in 2D boron nitride nanostructures: nanosheets, nanoribbons, nanomeshes, and hybrids with graphene," Nanoscale **4**, 6908 (2012).

[178] N. Peltekis, S. Kumar, N. McEvoy, K. Lee, A. Weidlich, and G. S. Duesberg, "The effect of downstream plasma treatments on graphene surfaces," Carbon **50**, 395 (2012).

[179] F. Banhart, J. Kotakoski, and A. V. Krasheninnikov, "Structural defects in graphene," ACS Nano **5**, 26 (2011).

[180] K. Obodo, R. Andrew, and N. Chetty, "Modification of the band offset in boronitrene," Physical Review B **84**, 155308 (2011).

[181] P. O. Lehtinen, A. S. Foster, A. Ayuela, T. T. Vehviläinen, and R. M. Nieminen, "Structure and magnetic properties of adatoms on carbon nanotubes," Physical Review B **69**, 155422 (2004).

[182] E. J. Dell, B. Capozzi, J. Xia, L. Venkataraman, and L. M. Campos, "Molecular length dictates the nature of charge carriers in single-molecule junctions of oxidized oligothiophenes," Nature Chemistry **7**, 209 (2015).

[183] R. M. Metzger, "Unimolecular electrical rectifiers," Chemical Reviews **103**, 3803 (2003).

[184] I. Díez Pérez, J. Hihath, Y. Lee, L. Yu, L. Adamska, M. a. Kozhushner, I. I. Oleynik, and N. Tao, "Rectification and stability of a single molecular diode with controlled orientation." Nature chemistry **1**, 635 (2009).

[185] M. K. Ng, D. C. Lee, and L. Yu, "Molecular diodes based on conjugated diblock co-oligomers," Journal of the American Chemical Society **124**, 11862 (2002).

[186] G. M. Morales, P. Jiang, S. Yuan, Y. Lee, A. Sanchez, W. You, and L. Yu, "Inversion of the rectifying effect in diblock molecular diodes by protonation," Journal of the American Chemical Society **127**, 10456 (2005).

[187] E. Lörtscher, B. Gotsmann, Y. Lee, L. Yu, C. Rettner, and H. Riel, "Transport properties of a single-molecule diode," ACS Nano **6**, 4931 (2012).

[188] M. L. Chabinyc, X. Chen, R. E. Holmlin, H. Jacobs, H. Skulason, C. D. Frisbie, V. Mujica, M. a. Ratner, M. A. Rampi, and G. M. Whitesides, "Molecular rectification in a metal-insulator-metal junction based on self-assembled monolayers," Journal of the American Chemical Society **124**, 11730 (2002).

[189] C. Toher, A. Filippetti, S. Sanvito, and K. Burke, "Self-interaction errors in density-functional calculations of electronic transport," Physical Review Letters **95**, 146402 (2005).

[190] G.-H. Lee, Y.-J. Yu, X. Cui, N. Petrone, C.-H. Lee, S. Choi, D.-Y. Lee, C. Lee, W. J. Yoo, K. Watanabe, T. Taniguchi, C. Nuckolls, P. Kim, and J. Hone, "Flexible and Transparent MoS 2 Field- Effect Transistors on Hexagonal Boron Nitride-graphene Heterostructures," ACS Nano **9**, 7931 (2013).

[191] Y. Gao, Y. Zhang, P. Chen, Y. Li, M. Liu, T. Gao, D. Ma, Y. Chen, Z. Cheng, X. Qiu, W. Duan, and Z. Liu, "Toward single-layer uniform hexagonal boron nitride-graphene patchworks with zigzag linking edges," Nano Letters **13**, 3439 (2013).

[192] Z. Liu, L. Ma, G. Shi, W. Zhou, Y. Gong, S. Lei, X. Yang, J. Zhang, J. Yu, K. P. Hackenberg, A. Babakhani, J.-C. Idrobo, R. Vajtai, J. Lou, and P. M. Ajayan, "In-plane heterostructures of graphene and hexagonal boron nitride with controlled domain sizes." Nature Nanotechnology **8**, 119 (2013).

[193] R. Chrenko, "Ultraviolet and infrared spectra of cubic boron nitride," Solid State Communications **14**, 511 (1974).

[194] K. Watanabe, T. Taniguchi, and H. Kanda, "Direct-bandgap properties and evidence for ultraviolet lasing of hexagonal boron nitride single crystal." Nature Materials **3**, 404 (2004).

[195] X. Wei, M. S. Wang, Y. Bando, and D. Golberg, "Electron-beam-induced substitutional carbon doping of boron nitride nanosheets, nanoribbons, and nanotubes," ACS Nano **5**, 2916 (2011).

[196] Z. Liu, Q. Xue, T. Zhang, Y. Tao, C. Ling, and M. Shan, "Carbon doping of hexagonal boron nitride by using CO molecules," Journal of Physical Chemistry C **117**, 9332 (2013).

[197] D. Golberg, Y. Bando, Y. Huang, T. Terao, M. Mitome, C. Tang, and C. Zhi, "Boron Nitride Nanotubes and Nanosheets," ACS Nano **4**, 2979 (2010).

[198] N. Berseneva, A. Gulans, A. V. Krasheninnikov, and R. M. Nieminen, "Electronic structure of boron nitride sheets doped with carbon from first-principles calculations," Physical Review B **87**, 035404 (2013).

[199] Y. Lin and J. W. Connell, "Advances in 2D boron nitride nanostructures: nanosheets, nanoribbons, nanomeshes, and hybrids with graphene," Nanoscale **4**, 6908 (2012).

[200] C.-H. Park and S. G. Louie, "Energy Gaps and Stark Effect in Boron Nitride Nanoribbons," Nano Letters **8**, 2200 (2008).

[201] N. Jain, T. Bansal, C. A. Durcan, Y. Xu, and B. Yu, "Monolayer graphene/hexagonal boron nitride heterostructure," Carbon **54**, 396 (2013).

[202] W. Yang, G. Chen, Z. Shi, C.-C. Liu, L. Zhang, G. Xie, M. Cheng, D. Wang, R. Yang, D. Shi, K. Watanabe, T. Taniguchi, Y. Yao, Y. Zhang, and G. Zhang, "Epitaxial growth of single-domain graphene on hexagonal boron nitride." Nature Materials **12**, 792 (2013).

[203] D. M. Cardamone and G. Kirczenow, "Single-molecule device prototypes for protein-based nanoelectronics: Negative differential resistance and current rectification in oligopeptides," Physical Review B **77**, 165403 (2008).

[204] J. Huang, W. Wang, Qunxiang, and J. Yang, "Negative differential resistance devices by using N-doped graphene nanoribbons," Journal of Chemical Physics **140**, 164703 (2014).

[205] H. W. andYing Xu and G. Zhou, "Dual conductance, negative differential resistance, and rectifying behavior in a molecular device modulated by side groups," Journal of Chemical Physics **136**, 184704 (2012).

[206] Y. Xue, S. Datta, S. Hong, R. Reifenberger, J. I. Henderson, and C. P. Kubiak, "Negative Differential Resistance in the Scanning Tunneling Spectroscopy of Organic molecules," Physical Review B **59**, R7852 (1998).

[207] H. Dalgleish and G. Kirczenow, "Interface states, negative differential resistance, and rectification in molecular junctions with transition-metal contacts," Physical Review B **73**, 245431 (2006).

[208] E. Emberly and G. Kirczenow, "Current-Driven Conformational Changes, Charging and Negative Differential Resistance in Molecular Wires," Physical Review B **64**, 125318 (2001).

[209] I. W. Lyo and P. Avouris, "Negative differential resistance on the atomic scale: implications for atomic scale devices," Science **245**, 1369 (1989).

[210] N. D. Lang, "Negative differential resistance at atomic contacts," Physical Review B **55**, 9364 (1997).

[211] W. Y. Kim, S. K. Kwon, and K. S. Kim, "Negative differential resistance of carbon nanotube electrodes with asymmetric coupling phenomena," Physical Review B **76**, 033415 (2007).

[212] R. Pati, M. McClain, and A. Bandyopadhyay, "Origin of negative differential resistance in a strongly coupled single molecule-metal junction device," Physical Review Letters **100**, 246801 (2008).

[213] M. Topsakal, E. Aktürk, and S. Ciraci, "First-principles study of two- and one-dimensional honeycomb structures of boron nitride," Physical Review B **79**, 115442 (2009).

[214] M. Oehme, "Silicon interband tunneling diodes with high peak-to-valley ratios," Thin Solid Films **520**, 3341 (2012).

[215] J. Koga, C. Vanderstraeten, S.-I. Takagi, and A. Toriumi, "New Approach to Negative Differential Conductance with High Peak-to-Valley Ratio in Silicon," Jpn. J. Appl. Phys. **39**, 2246 (2000).

[216] V. Nam Do and P. Dollfus, "Negative differential resistance in zigzag-edge graphene nanoribbon junctions," Journal of Applied Physics **107**, 063705 (2010).

[217] H. Raza, "Electronic structure modulation for low-power switching." Nanoscale Research Letters **8**, 74 (2013).

[218] E. Ozbay, D. M. Bloom, D. H. Chow, and J. N. Schulman, "1.7-ps, Microwave, integrated-circuit-compatible InAs/AlSb resonant tunneling diodes," IEEE Electron Device Letters **14**, 400 (1993).

[219] M. S. Dresselhaus, *Science of Fullerenes and Carbon Nanotubes* (Academic Press, San Diego, 1996).

[220] J. W. Mintmire, B. I. Dunlap, and C. T. White, "Are fullerene tubules metallic?" Physical Review Letters **68**, 631 (1992).

[221] S. Iijima, "Helical microtubules of graphitic carbon," Nature **354**, 56 (1991).

[222] M. U. Kahaly, S. P. Singh, and U. V. Waghmare, "Carbon Nanotubes with an Extended Line Defect," Small **4**, 2209 (2008).

[223] J. Lahiri, Y. Lin, P. Bozkurt, I. I. Oleynik, and M. Batzill, "An extended defect in graphene as a metallic wire," Nature nanotechnology **5**, 326 (2010).

[224] J. Kotakoski, A. V. Krasheninnikov, U. Kaiser, and J. C. Meyer, "From point defects in graphene to two-dimensional amorphous carbon," Physical Review Letters **106**, 105505 (2011).

[225] J.-H. Chen, G. Autès, N. Alem, F. Gargiulo, A. Gautam, M. Linck, C. Kisielowski, O. V. Yazyev, S. G. Louie, and A. Zettl, "Controlled growth of a line defect in graphene and implications for gate-tunable valley filtering," Physical Review B **89**, 121407 (2014).

[226] E. Cockayne, G. M. Rutter, N. P. Guisinger, J. N. Crain, P. N. First, and J. a. Stroscio, "Grain boundary loops in graphene," Physical Review B **83**, 195425 (2011).

[227] H. Terrones, R. Lv, M. Terrones, and M. S. Dresselhaus, "The role of defects and doping in 2D graphene sheets and 1D nanoribbons," Reports on Progress in Physics **75**, 062501 (2012).

[228] R. Nair, I.-L. Tsai, M. Sepioni, O. Lehtinen, J. Keinonen, A. Krasheninnikov, A. Castro Neto, M. Katsnelson, A. Geim, and I. Grigorieva, "Dual origin of defect magnetism in graphene and its reversible switching by molecular doping," Nature Communications **4**, 2010 (2013).

[229] M. Gmitra, D. Kochan, and J. Fabian, "Spin-Orbit Coupling in Hydrogenated Graphene," Physical Review Letters **110**, 246602 (2013).

[230] M. B. Lundeberg, R. Yang, J. Renard, and J. A. Folk, "Defect-Mediated Spin Relaxation and Dephasing in Graphene," Physical Review Letters **110**, 156601 (2013).

[231] Z. Tehrani, G. Burwell, M. A. M. Azmi, A. Castaing, R. Rickman, J. Almarashi, P. Dunstan, A. M. Beigi, S. H. Doak, and O. J. Guy, "Generic epitaxial graphene biosensors for ultrasensitive detection of cancer risk biomarker," 2D Materials **1**, 025004 (2014).

[232] R. Yang, S. Wu, D. Wang, G. Xie, M. Cheng, G. Wang, W. Yang, P. Chen, D. Shi, and G. Zhang, "Fabrication of high-quality all-graphene devices with low contact resistances," Nano Research **7**, 1449 (2014).

[233] G. Kim, S.-H. Jhi, S. Lim, and N. Park, "Effect of vacancy defects in graphene on metal anchoring and hydrogen adsorption," Applied Physics Letters **94**, 173102 (2009).

[234] J. A. Rodriguez Manzo, O. Cretu, and F. Banhart, "Trapping of Metal Atoms in Vacancies of Carbon Nanotubes and Graphene," ACS Nano **4**, 3422 (2010).

[235] A. V. Krasheninnikov, P. O. Lehtinen, A. S. Foster, P. Pyykkö, and R. M. Nieminen, "Embedding Transition-Metal Atoms in Graphene: Structure, Bonding, and Magnetism," Physical Review Letters **102**, 126807 (2009).

[236] O. Cretu, A. V. Krasheninnikov, J. A. Rodríguez Manzo, L. Sun, R. M. Nieminen, and F. Banhart, "Migration and Localization of Metal Atoms on Strained Graphene," Physical Review Letters **105**, 196102 (2010).

[237] Y. Tang, Z. Yang, and X. Dai, "Trapping of metal atoms in the defects on graphene," The Journal of Chemical Physics **135**, 224704 (2011).

[238] K. Kim, H.-B.-R. Lee, R. W. Johnson, J. T. Tanskanen, N. Liu, M.-G. Kim, C. Pang, C. Ahn, S. F. Bent, and Z. Bao, "Selective metal deposition at graphene line defects by atomic layer deposition," Nature Communications **5**, 4781 (2014).

[239] M. Pannetier Lecoeur, C. Fermon, A. de Vismes, E. Kerr, and L. Vieux Rochaz, "Low noise magnetoresistive sensors for current measurement and compasses," Journal of Magnetism and Magnetic Materials **316**, e246 (2007).

[240] K. M. H. Lenssen, D. J. Adelerhof, H. J. Gassen, A. E. T. Kuiper, G. H. J. Somers, and J. B. A. D. Van Zon, "Robust giant magnetoresistance sensors," Sensors and Actuators, A: Physical **85**, 1 (2000).

[241] B. Hu and Y. Wu, "Tuning magnetoresistance between positive and negative values in organic semiconductors," Nature Materials **6**, 985 (2007).

[242] J. Bai, R. Cheng, F. Xiu, L. Liao, M. Wang, A. Shailos, K. L. Wang, Y. Huang, and X. Duan, "Very large magnetoresistance in graphene nanoribbons," Nature Nanotechnology **5**, 655 (2010).

[243] M. Y. Han, J. C. Brant, and P. Kim, "Electron Transport in Disordered Graphene Nanoribbons," Physical Review Letters **104**, 056801 (2010).

[244] W. Li, M. Zhao, Y. Xia, R. Zhang, and Y. Mu, "Covalent-adsorption induced magnetism in graphene," Journal of Materials Chemistry **19**, 9274 (2009).

[245] N. A. Pike and D. Stroud, "Graphene with adatoms: Tuning the magnetic moment with an applied voltage," Applied Physics Letters **105**, 052404 (2014).

[246] E. E. Mallon, M. Y. Jeon, M. Navarro, A. Bhan, and M. Tsapatsis, "Probing the relationship between silicalite-1 defects and polyol adsorption properties," Langmuir **29**, 6546 (2013).

[247] P. Ordejón, E. Artacho, and J. M. Soler, "Self-consistent order-N density-functional calculations for very large systems," Physical Review B **53**, R10441 (1996).

[248] Z. Zhu, W. Chen, Q. Sun, and Y. Jia, "Half-metal behaviour mediated by self-doping of topological line defect combining with adsorption of 3d transition-metal atomic chains in graphene," Journal of Physics D: Applied Physics **47**, 055303 (2014).

[249] J. M. de Almeida, A. R. R. Rocha, A. J. R. da Silva, and A. Fazzio, "Spin filtering and disorder-induced magnetoresistance in carbon nanotubes: Ab initio calculations," Physical Review B **84**, 085412 (2011).

[250] V. M. Karpan, P. A. Khomyakov, A. A. Starikov, G. Giovannetti, M. Zwierzycki, M. Talanana, G. Brocks, J. van den Brink, and P. J. Kelly, "Theoretical prediction of perfect spin filtering at interfaces between close-packed surfaces of Ni or Co and graphite or graphene," Physical Review B **78**, 195419 (2008).

9 Papers Published, Submitted, and Under Preparation

• **J. T. Obodo** and U. Schwingenschlögl, "Recent developments in molecular switches and rectifiers", *To be submitted.*

• **J. T. Obodo**, A. Murat, and U. Schwingenschlögl, "Quantum transport through tunable molecular diodes", *To be submitted.*

• **J. T. Obodo**, I. Rungger, S. Sanvito, and U. Schwingenschlögl, "Current-induced changes of migration energy barriers in carbon-based systems", *Submitted.*

• **J. T. Obodo**, K. O. Obodo, and U. Schwingenschlögl, "Negative differential conductance in two-dimensional C-functionalized boronitrene", New Journal of Physics **17**, 093012 (2015).

• **J. T. Obodo**, M. Upadhyay Kahaly, and U. Schwingenschlögl, "Magnetoresistance of Mn-decorated topological line defects in graphene", Physical Review B **91**, 014413 (2015).

• K. Gkionis, **J. T. Obodo**, C. Cucinotta, S. Sanvito, and U. Schwingenschlögl, "Molecular dynamics investigation of gold-carbon nanotube junctions in non-aqueous solutions", Journal of Materials Chemistry A **2**, 16498 (2014).

• **J. T. Obodo**, K. Gkionis, I. Rungger, S. Sanvito, and U. Schwingenschlögl,, 'Hydrogen bonding as the origin of the switching behavior in dithiolated phenylene-vinylene oligomers", Physical Review B **88**, 085438 (2013).